e. Copy two specific publications/research papers of the applicant, relevant to the research work on which the award is claimed.

Das M, Sreedharan S, Shee S, Malhotra N, Nandy M, Banerjeee U, Kholi S, Rajmani R, Chandra N, Seshasayee AN, Laxman S and **Singh A**. Cysteine desulfurase (IscS)–mediated fine- tuning of bioenergetics and SUF expression prevents *Mycobacterium tuberculosis* hypervirulence. ***Sci Adv***. 2023. 15(50): eadh2858

Mishra R, Kohli S, Malhotra N, Bandhyopadhyay P, Mehta M, Munshi M, Adiga V, Ahuja VK, Shandil RK, Rajmani RS, Seshasayee ASN and **Singh A**. Targeting redox heterogeneity to counteract drug tolerance in replicating *Mycobacterium tuberculosis*. ***Sci Transl Med.*** 2019. 11 (518)

MICROBIOLOGY

Cysteine desulfurase (IscS)–mediated fine-tuning of bioenergetics and SUF expression prevents *Mycobacterium tuberculosis* hypervirulence

Mayashree Das[1,2], Sreesa Sreedharan[3,4], Somnath Shee[1,2], Nitish Malhotra[5], Meghna Nandy[5], Ushashi Banerjee[6], Sakshi Kohli[1,2], Raju S. Rajmani[7], Nagasuma Chandra[6], Aswin Sai Narain Seshasayee[5], Sunil Laxman[3], Amit Singh[1,2]*

Iron-sulfur (Fe-S) biogenesis requires multiprotein assembly systems, SUF and ISC, in most prokaryotes. *M. tuberculosis* (*Mtb*) encodes a complete SUF system, the depletion of which was bactericidal. The ISC operon is truncated to a single gene *iscS* (cysteine desulfurase), whose function remains uncertain. Here, we show that *MtbΔiscS* is bioenergetically deficient and hypersensitive to oxidative stress, antibiotics, and hypoxia. *MtbΔiscS* resisted killing by nitric oxide (NO). RNA sequencing indicates that IscS is important for expressing regulons of DosR and Fe-S–containing transcription factors, WhiB3 and SufR. Unlike wild-type *Mtb*, *MtbΔiscS* could not enter a stable persistent state, continued replicating in mice, and showed hypervirulence. The *suf* operon was overexpressed in *MtbΔiscS* during infection in a NO-dependent manner. Suppressing *suf* expression in *MtbΔiscS* either by CRISPR interference or upon infection in inducible NO-deficient mice arrests hypervirulence. Together, *Mtb* redesigned the ISC system to "fine-tune" the expression of SUF machinery for establishing persistence without causing detrimental disease in the host.

INTRODUCTION

The *Mycobacterium tuberculosis* (*Mtb*) life cycle inside the human host relies upon successful adaptation to commonly encountered stresses such as reactive oxygen species (ROS), reactive nitrogen species (RNS), iron starvation, low pH, and hypoxia (*1*). Iron-sulfur (Fe-S) clusters, which are the most ancient protein prosthetic groups, are sensitive targets for ROS and RNS, and their biogenesis is adversely affected by iron starvation (*2*, *3*). *Mtb* contains more than 50 Fe-S cluster proteins that carry out diverse functions within central metabolism, gene regulation, drug resistance, and persistence (table S1) (*4*, *5*). Therefore, knowledge of the biogenesis and repair of Fe-S clusters is critical to understanding the basis of persistence for this human pathogen.

Many organisms express multiple Fe-S assembly systems (e.g., NIF, ISC, and SUF), wherein the SUF system is largely restricted to organisms that are frequently exposed to Fe-S cluster–damaging conditions (*6*). In line with this, *Mtb* expresses a complete SUF system (*Rv1461-Rv1466*) that not only is essential under standard growth conditions but also protects *Mtb* from stresses [e.g., nitric oxide (NO) and iron starvation] by repairing damaged Fe-S clusters (*7*–*9*). Furthermore, depletion of the SUF system impairs *Mtb*'s ability to maintain redox balance, central carbon metabolism (CCM), respiration, and persistence when in animals (*10*, *11*). Consistent with these findings, the SUF system was induced under stressful conditions such as ROS, reactive nitrogen intermediate (RNI), low iron, antibiotics, macrophage milieu, and sputum of tuberculosis (TB) patients (*9*, *12*–*16*). *Mtb* also encodes an *iscS* gene (*Rv3025c*; cysteine desulfurase) that is not a part of the *suf* locus and is not surrounded by other *isc* genes, such as *iscA* and *iscU*, and by chaperones *hscA* and *hscB* (*17*). Although these findings indicate that the SUF machinery is the primary Fe-S biogenesis system in *Mtb*, a previous report suggested the involvement of *Mtb* IscS in building a 4Fe-4S cluster of the transcription factor WhiB3 in vitro (*18*). Moreover, a mutant of IscS (*MtbΔiscS*) was hypersensitive to oxidative stress and displayed impaired activity of the Fe-S cluster–dependent enzymes, aconitase and succinate dehydrogenase (*17*). These findings indicate that IscS is involved in maintaining Fe-S cluster homeostasis and protects *Mtb* from oxidative stress. However, important questions remain unanswered: What are the mechanisms by which IscS contributes to oxidative stress resistance and what is the consequence of an IscS loss in the backdrop of a fully functional SUF system on the persistence and virulence of *Mtb*.

In this study, we used a redox biosensor and extracellular flux (XF) analyzer to compare the redox balance and bioenergetics of wild-type (WT) *Mtb* and *MtbΔiscS*. We also examined metabolomics and transcriptomics of *MtbΔiscS* and analyzed the survival phenotype of the mutant under diverse stresses in vitro and in mice. Last, we found that the interplay between IscS and SUF system is crucial for adjusting the virulence of *Mtb* in mice. We anticipate that understanding the IscS-linked metabolic and regulatory events will contribute toward knowledge of how *Mtb* maintain cellular homeostasis for persistence.

[1]Department of Microbiology and Cell Biology, Indian Institute of Science, Bangalore 560012, India. [2]Centre for Infectious Disease Research, Indian Institute of Science, Bangalore 560012, India. [3]Institute for Stem Cell Science and Regenerative Medicine, Bangalore 560065, India. [4]School of Chemical and Biotechnology, (SASTRA)-Deemed to be University, Thanjavur 613401, India. [5]National Centre for Biological Sciences (NCBS), Tata Institute of Fundamental Research (TIFR), Bangalore 560065, India. [6]Department of Biochemistry, Indian Institute of Science, Bangalore 560012, India. [7]Molecular Biophysics Unit, Indian Institute of Science, Bangalore 560012, India.
*Corresponding author. Email: asingh@iisc.ac.in

RESULTS

IscS is required to maintain redox homeostasis in *Mtb*

A previous study reported that depletion of IscS results in a slightly slower growth rate of *Mtb* and diminished activity of Fe-S cluster–containing enzyme, aconitase, under aerobic culture conditions (*17*). We confirmed this observation using *Mtb*Δ*iscS* (fig. S1, A and B). Aerobic metabolism inevitably generates highly deleterious superoxide ($O_2^{-\bullet}$) and hydrogen peroxide (H_2O_2) due to the univalent reduction of molecular oxygen (O_2) by redox enzymes (Fig. 1A). ROS-scavenging enzymes, along with Fe-S cluster biogenesis systems, protect cells from the adverse consequences of oxidative radicals and maintains redox homeostasis in diverse organisms (*2*, *5*, *19*–*21*). Therefore, we asked whether IscS is required to maintain redox balance under aerobic growth conditions in *Mtb*. To do this, we used a genetically encoded redox biosensor, Mrx1-roGFP2, to measure the redox potential of the antioxidant buffer mycothiol [reduced mycothiol (MSH)/oxidized mycothione (MSSM); E_{MSH}] as a proxy for cytoplasmic redox state of *Mtb* (*22*). The readout of Mrx1-roGFP2 can be analyzed by measuring the fluorescence intensity at 510 nm emission and excitation at 405 and 488 nm (fig. S2). An increase in the 405/488 ratio indicates a shift in the MSH/MSSM ratio toward MSSM due to either enzymatic oxidation of MSH in response to ROS or depletion of the total mycothiol pool (*22*). Treatment of *Mtb*-expressing Mrx1-roGFP2 to increasing concentrations of H_2O_2 gradually increased the biosensor ratio (fig. S3).

Exponentially growing *Mtb*Δ*iscS* expressing the biosensor exhibited a ~1.5- to 2.0-fold higher 405/488 ratio than WT *Mtb* and *iscS-com*p (Fig. 1B), indicating that the mutant suffers from oxidative stress under aerobic conditions. We have previously reported that a twofold increase in the biosensor ratio is similar to the oxidative stress induced by 500 μM H_2O_2 (fig. S3). These changes in the biosensor ratio corresponds to slightly oxidized E_{MSH} of −260 mV for *Mtb*Δ*iscS* as compared to WT *Mtb* (E_{MSH} = −280 mV) and *iscS-comp* (−275 mV). Using CellROX Deep Red dye, which becomes fluorescent upon intracellular oxidation by ROS, we confirmed that *Mtb*Δ*iscS* stained with CellROX displayed 1.5- and 3.0-fold greater fluorescence than WT *Mtb* and *iscS-comp*, respectively (Fig. 1C). An equivalent increase in CellROX fluorescence was observed upon treatment of *Mtb* with 50 to 100 μM cumene hydroperoxide (CHP) (fig. S4). ROS are known to damage Fe-S clusters and increase the pool of labile iron (*19*). We confirmed this by showing higher ROS in *Mtb* growing under iron-excess conditions, whereas iron limitation decreases ROS levels (fig. S5). Consistent with this finding, we observed an ~1.5-fold increase in free iron in *Mtb*Δ*iscS* compared to WT *Mtb* (Fig. 1D). Collectively, these data suggest that aerobically grown *Mtb*Δ*iscS* displays disruption of redox and iron homeostatic mechanisms.

Because most of the cytoplasmic pool of labile iron exists in the ferrous form (*23*) and catalyzes the Fenton reaction to generate deleterious hydroxyl radicals, we investigated whether ROS accumulation and slow growth of *Mtb*Δ*iscS* are due to elevated iron in the mutant. We treated exponentially grown WT *Mtb*, *Mtb*Δ*iscS*, and *iscS-comp* with 250 μM of the cell-permeable iron chelator 2,2-bipyridyl (Bip) followed by measurement of ROS and viability at 24 hours after treatment. Iron deprivation by Bip induces the IdeR-dependent expression of *esx-3* and *suf* operons (*13*). We detected increased expression of *esx-3* (*esxH*) and *suf* genes (*sufR*, *sufS*, and *sufB*) in Bip-treated *Mtb*, confirming iron deprivation (fig. S1C). Surprisingly, CellROX staining revealed higher ROS in all three strains upon treatment with Bip (Fig. 1E). While Bip treatment increased ROS in WT *Mtb* (~4-fold) and *iscS-comp* (~6-fold), a >10-fold increase was observed in *Mtb*Δ*iscS* as compared to WT *Mtb* untreated (Fig. 1E). Consistent with this, Bip treatment reduced the viability of *Mtb*Δ*iscS* by 70%. In contrast, Bip treatment reduced viability by only 10 to 20% in WT *Mtb* and *iscS-comp* (Fig. 1F). We determined the minimal inhibitory concentration at 90% (MIC_{90}) of Bip for WT *Mtb*, *Mtb*ΔiscS, and *iscS-comp* using Microplate Alamar Blue Assay (MABA). A twofold lower MIC_{90} of Bip was observed in the case of *Mtb*Δ*iscS* compared to WT *Mtb* and *iscS-comp* (fig. S1D). While surprising, our findings correlate with work on obligate aerobes and photosynthetic organisms such as *Anabaena* sp. and *Caulobacter cresentus* that display heightened ROS under iron starvation—a phenomenon not detected in facultative anaerobes/aerobes, such as *Escherichia coli* and *Bacillus subtilis* (*24*, *25*).

Given that a deficiency of IscS leads to accumulation of ROS in *Mtb*, treatment with antioxidants could potentially rescue the slow growth phenotype of *Mtb*Δ*iscS*. To test this, we evaluated the effect of thiourea (Thio), an ROS scavenger (*20*), on ROS accumulation using CellROX and survival of *Mtb*Δ*iscS*. As expected, treatment with 10 mM Thio for 24 hours reduced ROS levels in *Mtb*Δ*iscS* (Fig. 1G). All three strains showed comparable levels of ROS upon Thio treatment (Fig. 1G). Surprisingly, despite lowering ROS levels, Thio treatment further inhibited the growth of *Mtb*Δ*iscS* as revealed by two- to fourfold lower MIC_{90} of Thio against *Mtb*Δ*iscS* (3.125 mM) than WT *Mtb* (6.25 mM) and *iscS-comp* (12.5 mM) (fig. S1D).

Intracellular ROS generation takes place when flavoenzymes inadvertently relocate a fraction of their electron flux directly to molecular oxygen (*26*). Thus, under oxygen-deficient conditions, we expect a reduction in ROS generation. We hypothesize that if ROS accumulation is the cause of slow growth of *Mtb*Δ*iscS*, we could rescue the growth phenotype of mutant under conditions that limit ROS formation such as oxygen depletion. We used an in vitro Wayne model of hypoxia and reaeration (*27*). In this model, *Mtb* respiration gradually uses oxygen such that hypoxia and bacteriostasis is achieved by day 12 (Fig. 1H). We examined the growth phenotype of WT *Mtb*, *Mtb*Δ*iscS*, and *iscS-comp* after establishment of hypoxia in the Wayne model (*27*). We monitored oxygen depletion by examining decoloration of the dye methylene blue (MB). As expected, the blue color of MB dye decolorized by day 12 for WT *Mtb* and *iscS-comp*. However, and consistent with the slow growth phenotype of the mutant, the color of MB dye faded by day 16 for *Mtb*Δ*iscS*. We followed the viability of three strains for 10 days after establishment of hypoxia (i.e., after dye decolorization). As previously reported (*28*), WT *Mtb* retained 100% viability under hypoxic conditions for the entire duration of the experiment (Fig. 1I). In contrast, *Mtb*Δ*iscS* showed gradual loss of viability over time under hypoxic conditions (Fig. 1I). We conclude that increased ROS accumulation during aerobic metabolism might not be the primary cause of slow growth of *Mtb*Δ*iscS*. Because IscS coordinates Fe-S clusters of metabolic (e.g., aconitase) and respiratory (e.g., succinate dehydrogenase) enzymes (*17*), impaired bioenergetics could lead to ROS accumulation and slow growth of *Mtb*Δ*iscS*. Aberrant respiration could trap components of the electron transport chain in the reduced state that can directly transfer electron to molecular oxygen leading to ROS formation (*29*, *30*).

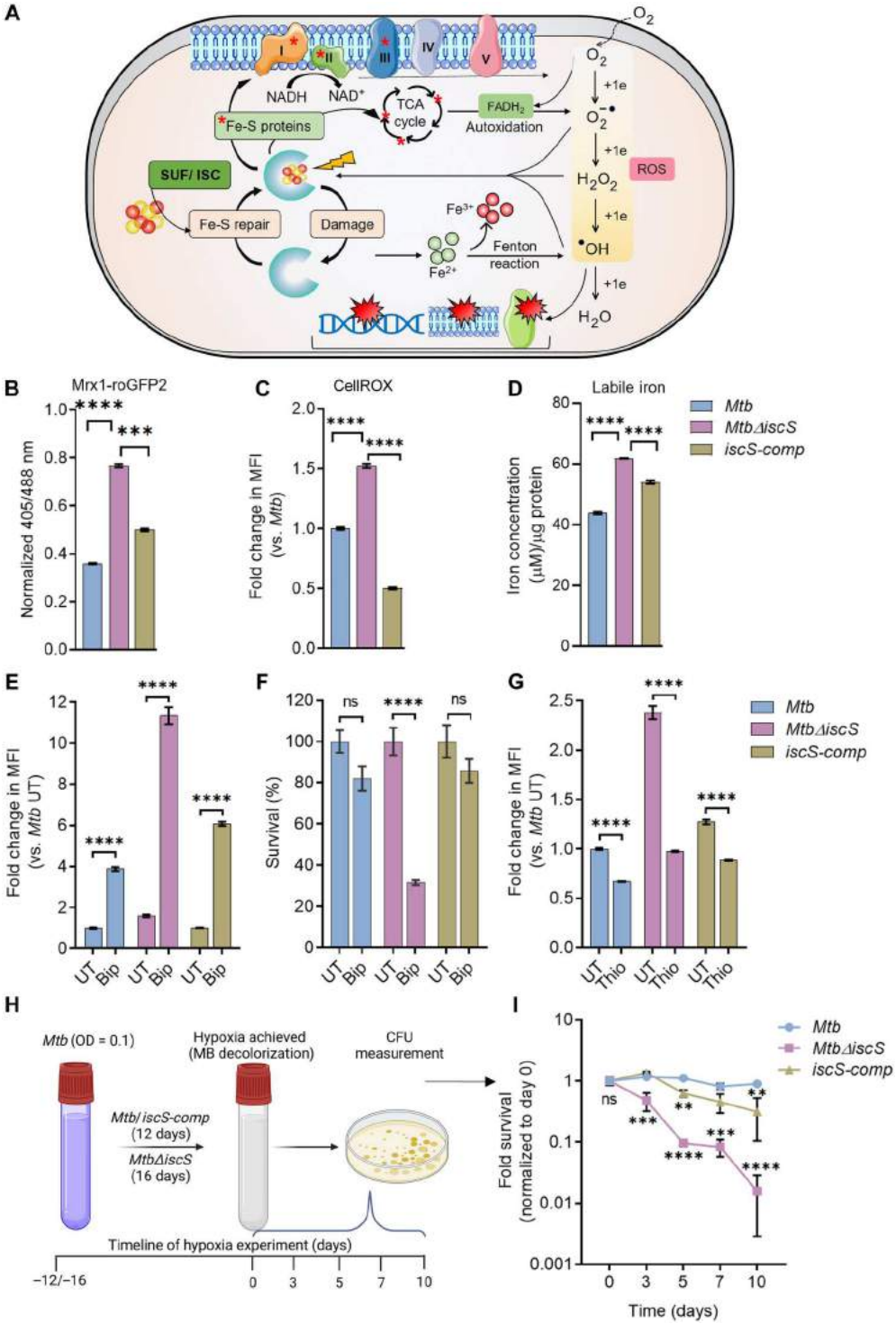

Fig. 1. IscS is required to maintain redox balance of *Mycobacterium tuberculosis* (*Mtb*). (**A**) Diagrammatic representation of endogenous reactive oxygen species (ROS) generation ($O_2^{-\bullet}$, H_2O_2, and $^{\bullet}OH$) due to the univalent reduction of O_2 via electron leak from redox-active enzymes. $O_2^{-\bullet}$ and H_2O_2 disrupt iron-sulfur (Fe-S) clusters, resulting in leaching of iron and formation of highly deleterious $^{\bullet}OH$ radical by Fenton reaction. SUF and ISC pathways are essential for Fe-S cluster biogenesis/repair. (**B**) The mycothiol redox potential (E_{MSH}) of *Mtb*, *MtbΔiscS*, *and iscS-comp* was determined by measuring Mrx1-roGFP2 biosensor ratio (405/488 nm) using flow cytometry. (**C**) *Mtb*, *MtbΔiscS*, *and iscS-comp* were stained with CellROX Deep Red dye to measure endogenous ROS. (**D**) Intracellular labile iron was determined for *Mtb*, *MtbΔiscS*, and *iscS-comp* by ferrozine-based colorimetric assay. Iron concentration was normalized to the protein content. *Mtb*, *MtbΔiscS*, *and iscS-comp* were exposed to 250 μM of cell-permeable iron chelator 2,2-bipyridyl (Bip) for 24 hours, followed by measurement of (**E**) endogenous ROS and (**F**) survival. (**G**) Endogenous ROS of *Mtb*, *MtbΔiscS*, and *iscS-comp* upon treatment with ROS scavenger Thio (10 mM). (**H**) Schematic representation showing experimental strategy to measure persistence of *Mtb* under hypoxia (credit: BioRender.com). (**I**) Viability of *Mtb*, *MtbΔiscS*, *and iscS-comp* cultured under hypoxia by colony-forming unit (CFU) enumeration. Data are presented as means ± SEM. (B to D) $^*P \le 0.05$ and $^{****}P \le 0.0001$ by one-way analysis of variance (ANOVA) with Bonferroni's multiple comparisons test. (E to G and I) $^{**}P \le 0.01$, $^{***}P \le 0.001$, and $^{****}P \le 0.0001$; ns, not significant by two-way ANOVA with Bonferroni's multiple comparisons test.

These events are possible as enough molecular oxygen might be present even under hypoxia for the reduction and ROS formation (*31*, *32*).

IscS deficiency affects CCM in *Mtb*

Fe-S cluster–dependent enzymes play key roles in CCM, branched-chain amino acid synthesis, and nucleotide biosynthesis (*33*). To examine whether the growth defect exhibited by *MtbΔiscS* correlates with a consequence of impaired metabolism, we used targeted, quantitative liquid chromatography–mass spectrometry (LC-MS/MS). We quantified the steady-state amounts of glycolytic, pentose phosphate pathway (PPP), and tricarboxylic acid (TCA) intermediates. We uniformly observed decreased amounts of several glycolytic and PPP intermediates in *MtbΔiscS* as compared to WT

Mtb (Fig. 2A). The influence of IscS deficiency on glycolysis and PPP was surprising, as none of the glycolytic and PPP enzymes contains Fe-S clusters. However, several glycolytic and gluconeogenesis enzymes contain cysteine thiols, which are sensitive to inhibition by oxidation and S-mycothiolation in mycobacteria (*34*, *35*). Further, glucose-6-phosphate (G6P) levels are regulated by endogenous ROS (*36*); therefore, diminished G6P levels in the mutant could be a consequence of ROS accumulation in *Mtb*Δ*iscS*. Efficient metabolism of G6P is also essential for generating nicotinamide adenine dinucleotide phosphate hydrogen (NADPH) through PPP (*36*), which serves as reductive power for antioxidant buffers (e.g., mycothiol and thioredoxin systems) and cell wall lipid biogenesis. Consistent with diminished PPP intermediates, levels of NADPH were slightly reduced, and nicotinamide adenine dinucleotide phosphate ($NADP^+$) levels were increased in *Mtb*Δ*iscS*, resulting in an overall increase in $NADP^+$/NADPH ratio as compared to WT *Mtb* (fig. S6, A to C).

Impaired glycolysis and PPP are also reflected in a lower abundance of sugar metabolites uridine 5′-diphosphate glucose (UDP-Glc) along with a modest reduction in guanosine diphosphate mannose (GDP-MAN) and uridine diphosphate *N*-acetyl glucosamine (UDP-Glc-NAC) required for the biosynthesis of peptidoglycan (Fig. 2A) (*37*). UDP-Glc-NAC is an essential substrate for mycothiol glycosyltransferase, which catalyzes the first step in the biosynthesis of mycothiol in *Mtb* (*38*). As expected, the total mycothiol (MSH + MSSM) content was substantially diminished in *Mtb*Δ*iscS* as compared to WT *Mtb* (Fig. 2B; $P \leq 0.001$), correlating well with the ratiometric increase in the mycothiol-specific biosensor (Mrx1-roGFP2) observed in the mutant. Mycothiol is also essential for detoxifying a highly reactive dicarbonyl by-product, methylglyoxal (MG) (*38*). We found that MG levels accumulated in *Mtb*Δ*iscS* as compared to WT *Mtb*, and this could in part be linked to the lack of mycothiol-linked remediation (Fig. 2B).

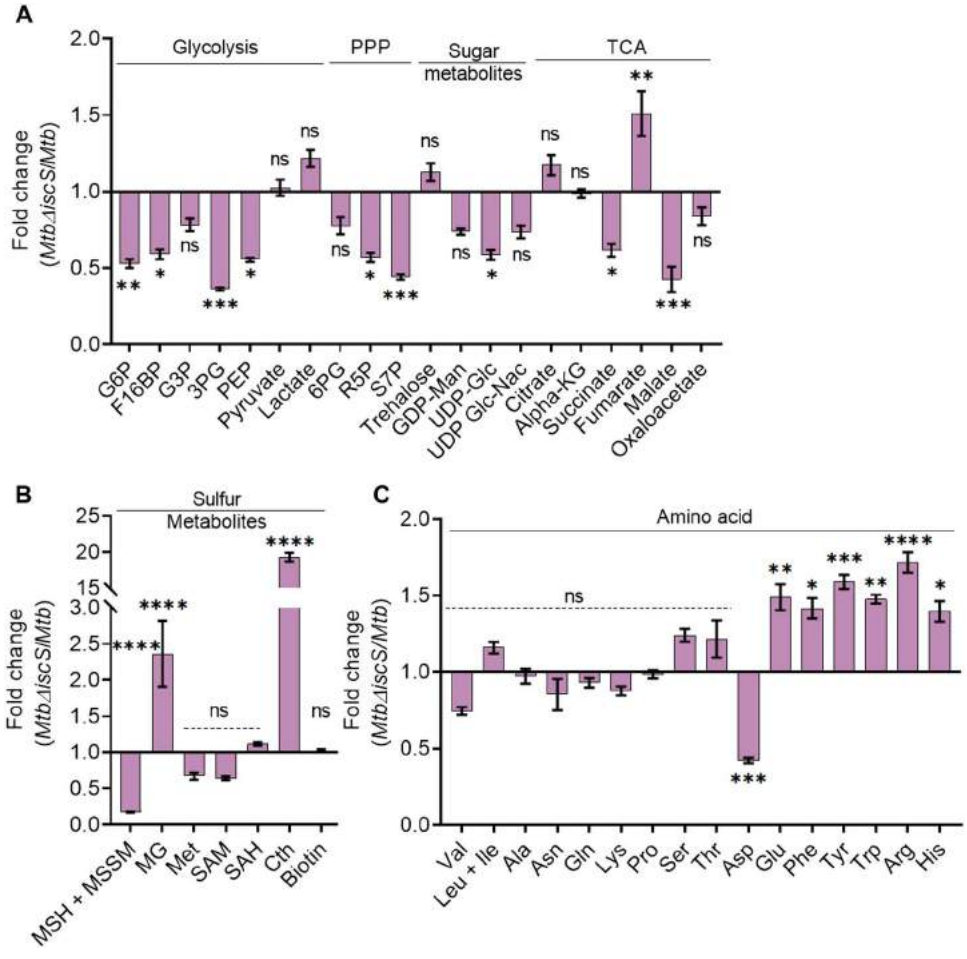

Fig. 2. IscS deletion results in deregulation of central carbon metabolism in *Mycobacterium tuberculosis* (*Mtb*). Quantitative liquid chromatography–mass spectrometry (LC-MS/MS) analysis of (**A**) glycolytic intermediates, pentose phosphate metabolites, tricarboxylic acid (TCA) metabolites, sugar nucleotides, (**B**) sulfur metabolites, and (**C**) amino acids of *Mtb* and *Mtb*Δ*iscS*. Data are presented as fold change respective to *Mtb* and means ± SEM. *$P \leq 0.05$, **$P \leq 0.01$, ***$P \leq 0.001$, and ****$P \leq 0.0001$ by two-way analysis of variance (ANOVA) with Bonferroni's multiple comparisons test compared to *Mtb* levels. PPP, pentose phosphate pathway; G6P, glucose-6-phosphate/fructose-6-phosphate; F16BP, fructose-1,6-bisphosphate; G3P, glyceraldehyde-3-phosphate; 3PG, 3-phosphoglycerate; PEP, phosphoenolpyruvate; MG, methylglyoxal; Met, methionine; SAM, *S*-adenosyl methionine; SAH, *S*-adenosyl homocysteine; Cth, cystathionine; 6PG, 6-phosphogluconate; R5P, ribulose-5-phosphate; S7P, sedoheptulose-7-phosphate; GDP-Man, guanosine diphosphate mannose; UDP-Glc, uracil diphosphate glucose; UDP-Glc-Nac, uridine diphosphate *N*-acetylglucosamine; ns, not significant.

*Mtb*Δ*iscS* has been previously reported to display diminished activities of the Fe-S cluster–containing TCA cycle enzymes aconitase and succinate dehydrogenase (*17*). Inactivation of aconitase is expected to raise citrate levels and reduce downstream TCA cycle metabolites such as α-ketoglutarate (α-KG) (*11*). Citrate showed only a marginal increase. Likewise, α-KG was unaffected in *Mtb*Δ*iscS* (Fig. 2A). Lowered succinate dehydrogenase activity indicates that the conversion of succinate to fumarate would be deficient in *Mtb*Δ*iscS*. Surprisingly, rather than accumulating succinate, *Mtb*Δ*iscS* displayed succinate depletion along with a concomitant increase in fumarate as compared to WT *Mtb* (Fig. 2A). These results suggest impairment of activity or expression of fumarate reductase in *Mtb*Δ*iscS*. Fumarate reductase is a 4Fe-4S cluster enzyme encoded by *frdABCD* and catalyzes the conversion of succinate to fumarate (*39*). Along with fumarate accumulation, a notable depletion of malate was observed in *Mtb*Δ*iscS* (Fig. 2A), indicating weakened fumarate hydratase activity. In line with the defective TCA cycle, the generation of nicotinamide adenine dinucleotide hydrogen (NADH) was marginally reduced, leading to higher nicotinamide adenine dinucleotide (NAD^+) and NAD^+/NADH ratio in *Mtb*Δ*iscS* as compared to WT *Mtb* and *IscS-comp* (fig. S6, D to F). A massive accumulation of the transsulfuration pathway metabolite cystathionine (Cth; 20-fold) and minor albeit nonsignificant decrease in methionine (Met) and *S*-adenosyl methionine (SAM) suggests an impairment of sulfur metabolism in *Mtb*Δ*iscS* (Fig. 2B). The enzyme adenosine 5′-phosphosulfate reductase (CysH) that catalyzes reductive assimilation of inorganic sulfate into Met, SAM, and cysteine (Cys) in *Mtb* contains a 4Fe-4S cluster (*5*); the activity of this enzyme may also be insufficient in *Mtb*Δ*iscS*. Under such conditions (abnormal reduction of inorganic sulfate), *Mtb* relies upon reverse transsulfuration (RTS) enzymes Cth-β-synthase (CBS) that converts homocysteine to Cth and Cth-γ-lyase (MetB) that generates Cys for mycothiol biosynthesis from Cth (*40*, *41*). MetB is also a bifunctional enzyme that can catalyze a γ-replacement reaction using Cys and *O*-succinyl/acetyl-homoserine to generate Cth via forward transsulfuration (FTS) reaction for regenerating methyl cycle intermediates [Met, SAM, and *S*-adenosyl homocysteine (SAH)]. While *Mtb*Δ*iscS* accumulates Cth and maintains methyl cycle intermediates, it shows depletion of mycothiol. These findings suggest that in the absence of IscS, *Mtb* switches from synthesizing Cys via the RTS pathway to using Cys for generating methyl cycle intermediates via the formation of Cth intermediate through the FTS pathway. We recently showed that metabolic switching from RTS to FTS pathways ensured *Mtb* survival by avoiding excess oxidative stress (*40*). Future experiments are required to clarify the link between IscS, RTS, and FTS pathways.

We observed a notable accumulation of various amino acids (Phe, Tyr, Trp, Glu, Arg, and His) in the mutant (Fig. 2C), suggesting attempts of *Mtb* to balance the loss of TCA cycle intermediates by anaplerosis in the absence of IscS. For example, elevated Glu could support the replenishment of α-KG by glutamate dehydrogenase in the background of defective glycolysis and aconitase activity in *Mtb*Δ*iscS*. Despite the reduction in levels of 2-phosphoenol pyruvate (PEP) and PPP intermediates, which are the initial substrates for the biosynthesis of aromatic amino acids (shikimate pathway), *Mtb*Δ*iscS* showed an accumulation of Phe, Trp, and Tyr. This could come from an impairment in the catabolic pathways for these amino acids, for instance, utilization into TCA or cofactor generation (e.g., molybdopterin biosynthesis) (*42*), along with increased utilization of PPP intermediates for amino acid synthesis. Complementation of IscS expression readjusted abundance of ~70% of the metabolites to levels comparable to those detected in WT *Mtb* (fig. S7, A and B). Last, the highlighted changes in the abundance of glycolysis, PPP, TCA, and amino acid pathways metabolites are also observed in the WhiB3 mutant of *Mtb* (*43*). IscS directly interacts with WhiB3 to coordinate 4Fe-4S cluster in vitro, indicating that IscS can regulate the Fe-S cluster–dependent regulatory activity of WhiB3 (*18*). Overall, the data indicate an important interplay between IscS, CCM, sulfur metabolism, and redox homeostasis in *Mtb*.

IscS is required to maintain bioenergetic homeostasis of *Mtb*

The altered pool of CCM in *Mtb*Δ*iscS* and the dependency of mycobacterial respiration on Fe-S cluster homeostasis (*10*, *11*) motivated us to measure the bioenergetics of the mutant. We used the XF analyzer and noninvasively tracked the extracellular acidification rate (ECAR) and oxygen consumption rate (OCR) of *Mtb*Δ*iscS*. ECAR is an accurate indication of proton (H^+) translocation due to glycolytic and TCA cycle activity, whereas OCR is a measure of respiration linked to oxidative phosphorylation.

We starved *Mtb* cultures overnight, followed by seeding in the XF microchamber, exposed them to glucose at a specific time, and then treated cells twice with the uncoupler carbonyl cyanide *m*-chlorophenyl hydrazine (CCCP). The injection of CCCP stimulates maximal respiration by *Mtb*, which provides an estimate of the bioenergetic reserves of the cells (*44*). The data are normalized to an equal number of viable cells (2×10^6 per well) in each case. We noticed that the basal OCR (before the addition of glucose) of *Mtb*Δ*iscS* is twofold ($P = 0.0001$) reduced as compared to WT *Mtb* (Fig. 3, A and C) with a change of 1.6-fold ($P = 0.005$) in ECAR (Fig. 3B). In the presence of glucose, *Mtb*Δ*iscS* displayed a substantial reduction in OCR (~2.5-fold, $P = 0.008$) and ECAR (~2.6-fold, $P = 0.00007$) relative to WT *Mtb* (Fig. 3, A to C). As expected, two sequential additions of CCCP stimulated OCR and ECAR in WT *Mtb* (Fig. 3, A and B). In contrast, a negligible increase in OCR and ECAR was observed in the case of CCCP-treated *Mtb*Δ*iscS* (Fig. 3, A and B). As a result, *Mtb*Δ*iscS* showed a 2.4-fold reduction in the spare respiratory capacity as compared to WT *Mtb* (Fig. 3C). The IscS complemented strain largely restored the bioenergetic profile to that of WT *Mtb* (Fig. 3, A to C). We conclude that IscS is required for maintaining the optimal bioenergetics of *Mtb*.

IscS modulates the expression of DosR, WhiB3, and SufR regulons in *Mtb*

We next asked whether any transcriptional response was associated with the redox, metabolic, and bioenergetic changes we described in *Mtb*Δ*iscS*. We analyzed the global transcriptome of *Mtb*Δ*iscS* compared to WT *Mtb*. Total bacterial RNA was isolated from logarithmically growing cultures at an absorbance of ~0.4, sequenced, and analyzed using the EdgeR platform. Multidimensional scaling analysis showed that the samples clustered by their biological replicates (fig. S8A). Compared to the transcriptome of WT *Mtb*, the expression of 547 genes was altered in *Mtb*Δ*iscS* [false discovery rate (FDR) ≤ 0.05, absolute fold change ≥ 1.5], of which 181 genes were up-regulated, whereas 366 genes showed down-regulation (table S2).

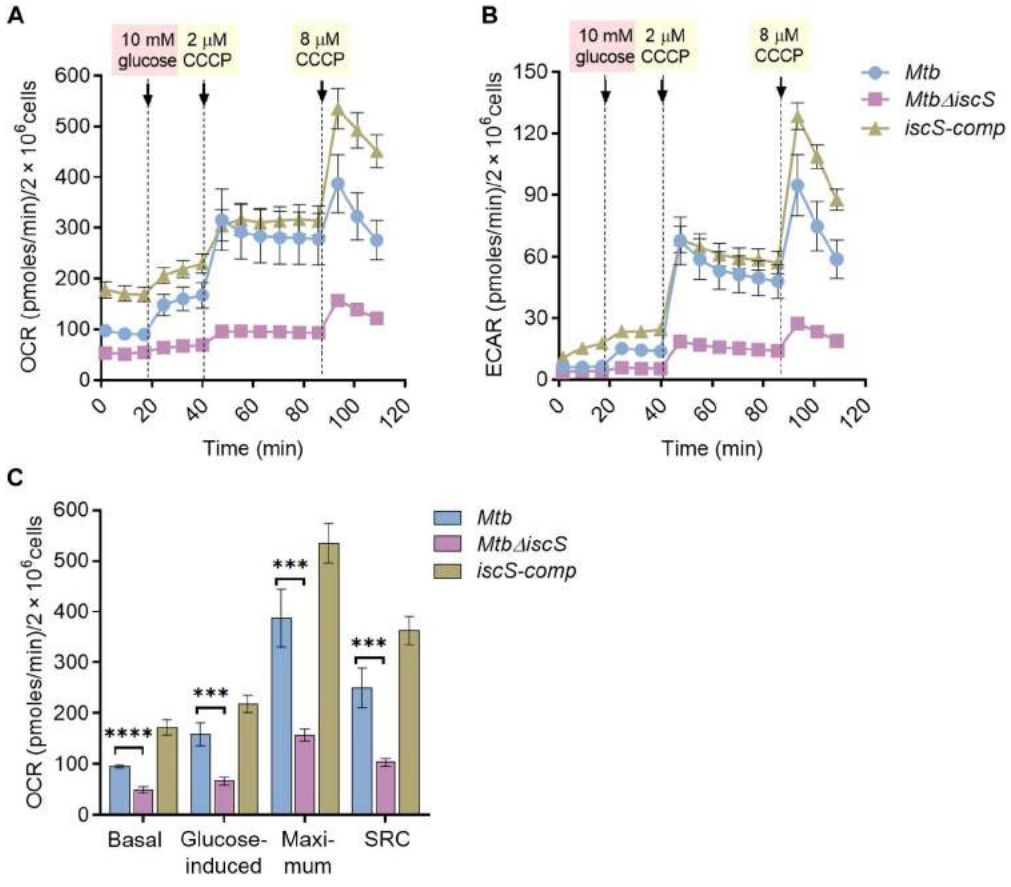

Fig. 3. Deletion of IscS results in diminished oxygen consumption rate (OCR) and extracellular acidification rate (ECAR). (**A**) OCR and (**B**) ECAR measurement of *Mycobacterium tuberculosis* (*Mtb*) , *MtbΔiscS*, and *iscS-comp* after injection of glucose and the uncoupler carbonyl cyanide *m*-chlorophenyl hydrazine (CCCP) indicated by the dotted lines. (**C**) Graph plotting basal respiration, glucose-induced respiration, maximum respiratory, and spare respiratory capacity (SRC) as derived from OCR values. All points of OCR and ECAR are normalized to colony-forming unit (CFU) (2×10^6 cells per well). Data are presented as means ± SEM. *$P \leq 0.05$, **$P \leq 0.01$, ***$P \leq 0.001$, and ****$P \leq 0.0001$ calculated by unpaired two-tailed *t* test.

Classification of differentially expressed genes (DEGs) according to annotated functional categories revealed up-regulation of stress-responsive genes (*trxB1*, *ahpCD*, *hsp*, *rubA*, and *groEL2*) that corroborates our finding of increased ROS in *MtbΔiscS* (Fig. 4, A and B). Genes involved in lipid metabolism showed a distinct expression pattern, with many catabolic genes (*kshA*, *lipFQR*, *fadA5*, *tgs1*,*2*,*4*, *accA2*, *accD2*, and *desA3*) being repressed; anabolic genes (*alkB*, *fadD*, *mas*, *pks1*, and *ppsA-E*) and lipid transporters (*mce1* and *mce3* operons) were up-regulated. Several genes involved in virulence and detoxification, such as toxin counterparts of toxin-antitoxin systems (*mazF8* and *relE*) (Fig. 4B) and stress-responsive sigma factors (*sigA*, *sigB*, and *sigH*) (Fig. 4C), were induced in *MtbΔiscS*. In agreement with our metabolomics data, genes associated with CCM such as fumarate reductase (*frdA-D*), phosphofructokinase (*pfkB*), methyl citrate cycle (*prpCD*), inositol-1-phosphate synthase (*ino1*), and molybdenum and biotin biosynthesis (*moaA1-D1* and *bioF2*) were repressed, whereas amino acid metabolism was induced (Fig. 4B). A general shutdown of housekeeping pathways was also evident by the down-regulation of genes involved in DNA and ribosomal RNA (rRNA) synthesis (Fig. 4C).

As expected from a defective adaptation of *MtbΔiscS* to O_2 limitation, the hypoxia-responsive Dos-dormancy regulon was uniformly suppressed in the mutant (Fig. 4D). Furthermore, we compared the expression of the Dos-dormancy regulon under hypoxic conditions by performing quantitative reverse transcription polymerase chain reaction (qRT-PCR) of a set of genes (*hspX*, *fdxA*, *devR*, *devS*, and *narK2*) representing the Dos regulon. As expected, hypoxia induces the expression of Dos regulon genes in WT *Mtb*. However, the expression of Dos genes is either less induced (*hspX* and *fdxA*) or down-regulated (*devR*, *devS*, and *nark2*) in *MtbΔiscS* compared to WT *Mtb* or *iscS-comp* (fig. S9A). We also found that the expression of eight genes encoding Fe-S cluster proteins was repressed, while two genes (*rubA* and *whiB6*) were induced in *MtbΔiscS* as compared to WT *Mtb* (Fig. 4B). We reasoned that the observed transcriptional changes are not a direct consequence of *iscS* loss but rather due to defective occupancy of Fe-S clusters on transcription factors. Consistent with this idea, the expression of several Fe-S cluster–containing transcription factors, such as *whiB1*, *whiB6*, *sirA*, and *sufR*, was deregulated in *MtbΔiscS* (Fig. 4B). Moreover, the transcriptome of *MtbΔiscS* overlapped with that of previously reported regulons of Fe-S cluster–containing transcription factors: *sufR* and *whiB3* (Fig. 4E) (*10*, *45*). Because *whiB1* is essential and its transcriptome is not reported, we depleted *whiB1* in *Mtb* (*whiB1-KD*), using

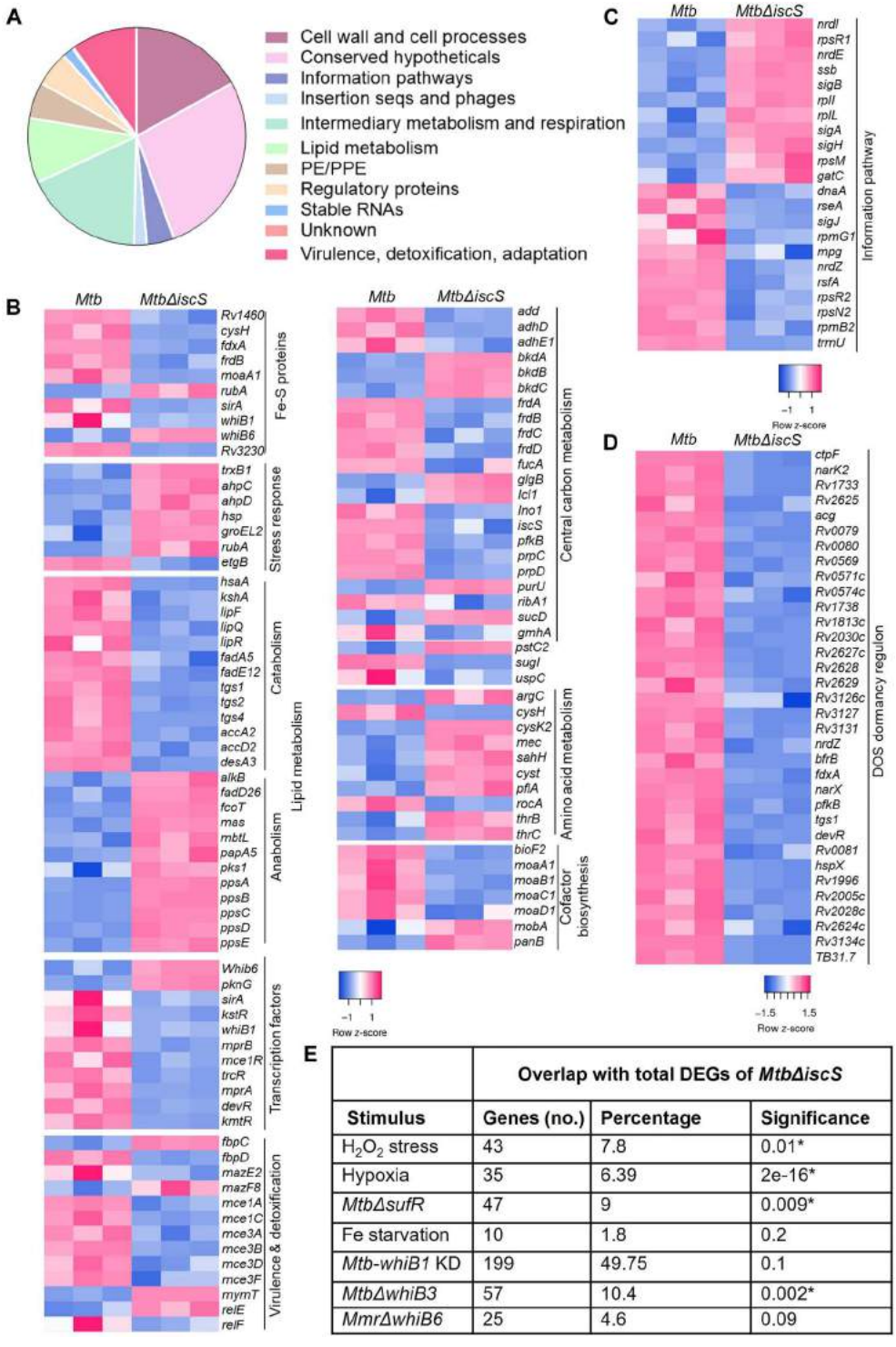

E

	Overlap with total DEGs of *MtbΔiscS*		
Stimulus	**Genes (no.)**	**Percentage**	**Significance**
H_2O_2 stress	43	7.8	0.01*
Hypoxia	35	6.39	2e-16*
MtbΔsufR	47	9	0.009*
Fe starvation	10	1.8	0.2
Mtb-whiB1 KD	199	49.75	0.1
MtbΔwhiB3	57	10.4	0.002*
MmrΔwhiB6	25	4.6	0.09

Fig. 4. *MtbΔiscS* displayed altered expression of genes regulated by iron-sulfur (Fe-S)–containing WhiBs, SufR, and DosR/S/T system. Total RNA was isolated from *Mycobacterium tuberculosis* (*Mtb*) cultures, grown to 0.4 OD_{600}, and subjected to RNA sequencing (RNA-seq) analysis. (**A**) Mycobrowser-based classification of the genes/pathways [1.5-fold change; false discovery rate (FDR) ≤ 0.05] deregulated in *MtbΔiscS*. (**B** to **D**) Heatmaps showing gene expression changes belonging to various functional categories. Heatmaps were constructed with row z-score on normalized logCPM values. (**E**) The table summarizes the overlap between the IscS transcriptome with the whole-genome expression under different stress conditions and transcriptomes *of Mtb-whiB1 KD*, *MtbΔwhiB3*, and *MtbΔsufR*. Fisher's exact test with *$P < 0.05$ as a cutoff for significance (table S2).

tetracycline-based CRISPR interference (CRISPRi) (fig. S10, A and B), and performed RNA sequencing (RNA-seq). An ~50% overlap between the transcriptomes of *whiB1* and *iscS* was observed (Fig. 4E). We also compared the overlap between DEGs in *Mtb*Δ*iscS* with DEGs of *Mtb* grown under oxygen limitation, H_2O_2, and Fe^- starvation. We considered that DEGs overlapped irrespective of whether the genes are similarly regulated (induced or repressed) between *Mtb*Δ*iscS* and WT *Mtb* exposed to different stress conditions. On this basis, the RNA-seq data of *Mtb*Δ*iscS* overlapped with *Mtb* grown under oxygen limitation and H_2O_2. Similarly, the transcriptome of *Mtb*Δ*iscS* did not coincide with iron starvation (*13*), a finding consistent with an increased fraction of free iron in the *iscS* mutant (Fig. 4E). The *iscS-comp* strain notably complements the IscS deregulated transcripts (table S2).

IscS protects *Mtb* from lethality caused by anti-TB drugs

Redox homeostasis, CCM, and respiration modulate *Mtb*'*s* response to anti-TB drugs (*44*). Furthermore, the ISC system in *E. coli* promotes killing by bactericidal antibiotics by providing iron for Fenton chemistry (*46*). In addition, ISC-mediated maturation of Fe-S clusters on respiratory complexes I and II promotes aminoglycoside killing by enabling respiration-dependent drug uptake (*47*). In the absence of ISC, cells switch to a less efficient SUF system for the maturation of Fe-S clusters on respiratory complexes, leading to defective uptake of aminoglycoside (*47*). However, a knowledge gap exists in our understanding of the role of Fe-S cluster biogenesis pathways in influencing lethality caused by anti-TB drugs. To begin understanding this, we measured the inhibition of *Mtb*Δ*iscS* growth by the clinically relevant anti-TB drugs rifampicin (Rif), isoniazid (Inh), moxifloxacin (Mox), and bedaquiline (Bdq). Using MABA, we determined MIC for Rif, Inh, Mox, and Bdq with WT *Mtb*, *Mtb*Δ*iscS*, and *iscS-comp* (Fig. 5A). *Mtb*Δ*iscS* exhibited two to fourfold lower MIC (therefore higher sensitivity) for Mox and Bdq (Fig. 5A). While *Mtb*Δ*iscS* showed no change in MIC for Rif, mutant growth was lowered by 84% at a subinhibitory concentration (8.8 nM) of Rif as compared to 37 to 67% inhibition of WT *Mtb* and *iscS-comp* (Fig. 5B).

We also measured the kill kinetics for Mox and Rif by colony-forming unit (CFU) analysis at various times after treatment with 1× MIC for WT *Mtb*. Compared to WT *Mtb*, *Mtb*Δ*iscS* displayed ~20- and 600-fold greater killing for Mox and Rif, respectively, at 10 days after exposure (Fig. 5, C and D). In contrast, *Mtb*Δ*iscS* exhibited higher MIC and resistance toward Inh (Fig. 5, A and E). One likely possibility is diminished levels of mycothiol in *Mtb*Δ*iscS*, which is known to cause Inh resistance in diverse mycobacterial species (*48*). Together, our data are in contrast with the current paradigm in bacteria, which indicates that Fe-S cluster biogenesis pathways promote killing by antibiotics (*46*). In *Mtb*, IscS reduces susceptibility toward anti-TB drugs.

IscS protects *Mtb* from oxidative stress but not nitrosative stress

Fe-S cluster biogenesis systems also contribute to protection from oxidative and nitrosative stress in bacteria (*49*). In general, the Suf system maintains Fe-S cluster homeostasis during high demand (e.g., NO and iron starvation), whereas IscS coordinates housekeeping requirements for Fe-S clusters in diverse bacteria (*3*, *33*, *50*, *51*). The *Mtb* Suf system is required for Fe-S cluster biogenesis/repair both under low (standard growth conditions) and high demand (nitrosative stress) for Fe-S clusters (*10*, *11*). Although IscS seems important for optimal growth, its contribution in assisting *Mtb* to counteract stresses remains uncertain. Thus, we next examined the requirement for IscS in providing tolerance to stresses such as organic hydroperoxide (CHP; 80 μM), superoxide [menadione (Mnd); 60 μM], and NO donor [diethylenetriamine (DETA)/NO adduct (1 mM)]. WT *Mtb* and *Mtb*Δ*iscS* were treated with CHP and Mnd for 4 hours (Fig. 6A) and 24 hours (Fig. 6B), and survival was measured by CFU analysis. WT *Mtb* was unaffected at 4 hours, while 24-hour exposure led to a 20% decrease in survival (Fig. 6B). In contrast, 4-hour CHP and Mnd treatment was sufficient to reduce survival by 80 and 25% in *Mtb*Δ*iscS* relative to WT *Mtb*, respectively (Fig. 6A). At 24 hours after exposure, CHP and Mnd treatment resulted in ~99% lower survival as compared to WT *Mtb* (Fig. 6B). Using the Mrx1-roGFP2 biosensor, we confirmed that sensitivity to CHP or Mnd is associated with excessive oxidative stress in *Mtb*Δ*iscS*. We observed nearly complete oxidation of the biosensor in CHP- or Mnd-treated *Mtb*Δ*iscS* relative to WT *Mtb* within 4 hours of exposure (Fig. 6C). The *iscS-comp* strain showed a survival phenotype comparable to that of WT *Mtb* (Fig. 6, A to C). In contrast to oxidative stress, treatment of 1 mM DETA NO uniformly induces bacteriostasis in all three strains without any adverse effect on *Mtb*Δ*iscS* (Fig. 6D). Because NO′s ability to kill *Mtb* depends upon concentration and exposure time (*9*), we repeatedly challenged *Mtb* strains to 1 mM DETA NO every 24 hours for 4 days, and viability was assessed. We observed that WT *Mtb* and *iscS-comp* maintained survival until day 2 but displayed a gradual loss in viability at day 3 (10-fold) and day 4 (100-fold) after treatment (Fig. 6E). In contrast, *Mtb*Δ*iscS* retained viability throughout the experiment, indicating that the mutant resists nitrosative stress (Fig. 6E). A similar trend was observed upon repeated exposure to 2 mM DETA NO. In the case of WT *Mtb* and *iscS-comp*, 2 mM DETA NO resulted in a complete loss of viability at day 4 after treatment (Fig. 6F), corresponding to more than 5-log reduction in bacterial numbers (no colonies detected). In contrast, we observed only 100-fold killing of *Mtb*Δ*iscS* at day 4 after treatment (Fig. 6F).

To understand the relevance of in vitro findings to infection settings, we assessed survival of the mutant in macrophages. We infected resting and immune-activated RAW264.7 murine macrophages with *Mtb* strains at a multiplicity of infection (MOI) of 2 and monitored survival over time. The WT *Mtb* showed unrestricted growth in resting RAW264.7 over time. *Mtb*Δ*iscS* displayed a marginal (twofold) reduction in growth as compared to WT *Mtb* and *iscS-comp* at day 3 after infection (Fig. 6G). As expected, activation of macrophages prevents the multiplication of *Mtb* strains. *Mtb*Δ*iscS* showed survival comparable to WT *Mtb* and *iscS-comp* in activated macrophages (Fig. 6H). Because NO generated via inducible nitric oxide synthase (iNOS) is one of the main contributors of redox stress in *Mtb* inside immune-activated murine macrophages (*1*), these data agree with comparable survival of the mutant and WT *Mtb* in response to a bacteriostatic concentration of NO (single-dose 1 mM DETA NO) in vitro. We further verified the association between IscS and NO by treating RAW264.7 with the iNOS inhibitor 1400W (*52*) and examined the growth phenotype of *Mtb*Δ*iscS*. All three strains resumed proliferation in the presence of 1400W; however, the growth was marginally slow for *Mtb*Δ*iscS* compared to WT *Mtb* and *iscS-comp* (Fig. 6I).

A

MIC$_{90}$ (μM)			
Antibiotics	*Mtb*	*MtbΔiscS*	*iscS-comp*
Moxifloxacin	0.25	0.0625	0.25
Rifampicin	0.035	0.035	0.035
Bedaquiline	0.225	0.112	0.225
Isoniazid	0.227	0.911	0.227

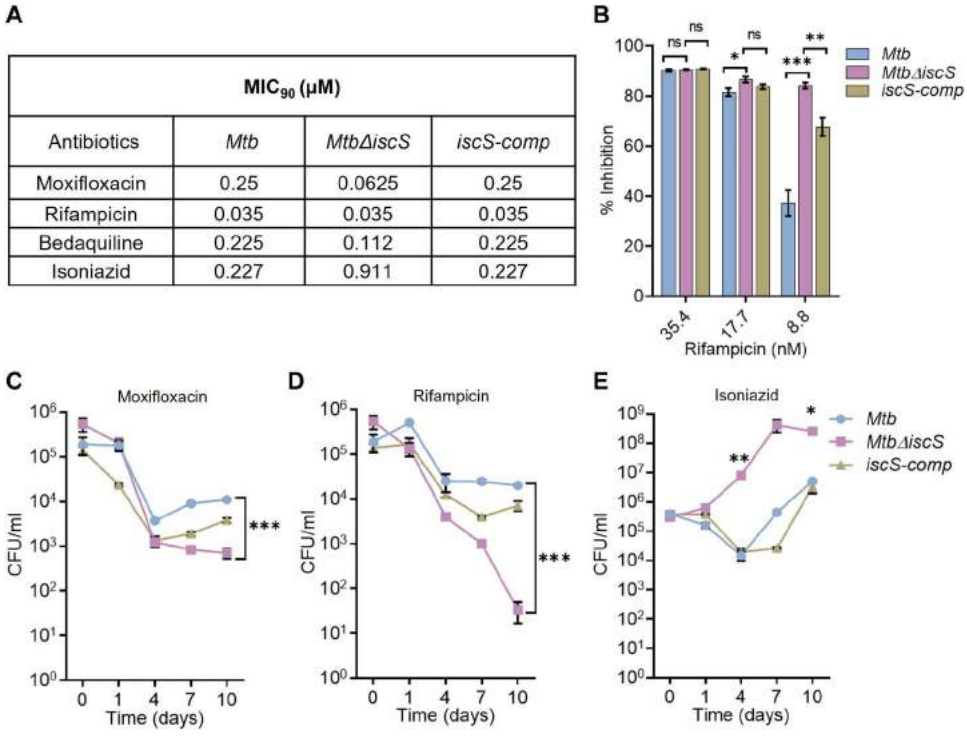

Fig. 5. *MtbΔiscS* shows enhanced sensitivity to anti-tuberculosis (TB) drugs. (**A**) *Mtb*, *MtbΔiscS*, and *iscS-comp* grown until OD_{600} values of 0.6 were treated with various concentrations of Rif, Mox, Bdq, and Inh, and MIC_{90} was determined using Alamar blue assay. Data are representative of two independent experiments done in duplicate. (**B**) Alamar blue dataset was used to calculate percent inhibition of *MtbΔiscS* by Rif compared to *Mtb* and *iscS-comp*. The strains *Mtb*, *MtbΔiscS*, and *iscS-comp* were treated with 1× MIC_{90} of (**C**) Mox (**D**) Rif, and (**E**) Inh, and survival over time was monitored by enumerating colony-forming units (CFUs). Data are presented as means ± SEM. (B to E) *$P \leq 0.05$, **$P \leq 0.01$, and ***$P \leq 0.001$ calculated by unpaired two-tailed *t* test. ns, not significant.

Disruption of IscS resulted in a hypervirulent mutant of *Mtb*

Depletion of Suf components (SufR and SufT) attenuated the survival and persistence of *Mtb* in vivo (*10*, *11*). However, the contribution of IscS to the pathogenesis of *Mtb* remains unknown. We examined the requirement for IscS in coordinating *Mtb's* virulence in a mice model of experimental TB. BALB/c mice were infected with WT *Mtb*, *MtbΔiscS*, and *iscS-comp* via the aerosol route, and survival was determined by CFU counts at days 28 and 56 after infection. WT *Mtb* having a functional IscS showed increased bacterial burden until 28 days after infection, after which the lung bacillary load stabilized (Fig. 7A). In contrast with the poor survival of *MtbΔiscS* in vitro, the mutant showed higher survival and persistence in mice (Fig. 7, A and B). Lung bacterial burden in mice with *MtbΔiscS* was significantly higher (~50-fold) than that in those infected with the WT *Mtb* at 28 days after infection (Fig. 7A). The bacillary load in the lungs reached a maximum of ~100-fold ($P \leq 0.0001$) higher for *MtbΔiscS* as compared to WT *Mtb*. A similar trend of elevated bacterial burden in the spleen of mice infected with *MtbΔiscS* as compared to WT *Mtb* was also detected (Fig. 7B).

Gross organ examination revealed that the lung surface of mice infected with *MtbΔiscS* showed discrete, well-circumscribed lesions (Fig. 7C) compared with poorly circumscribed and diffuse lesions in lungs of WT *Mtb*-infected mice. Histopathologic examination of the lungs of mice infected with WT *Mtb* revealed moderate granulomatous pneumonia with relatively smaller granulomas as compared to mild to severe granulomatous pneumonia characterized by multiple foci of granulomas with varying degrees of severity in the case of *MtbΔiscS* (Fig. 7D and fig. S11A). The *iscS-comp* strain showed partial attenuation of the hypervirulence phenotype in mice (Fig. 7A). Overall, the disruption of *iscS* in *Mtb* led to hypervirulence and abnormal granuloma formation in mice.

Hypervirulence of *MtbΔiscS* is reduced by blocking NO-dependent *suf* induction

ROI, RNI, iron starvation, and an intraphagosomal environment increase expression of the *suf* operon but not IscS in *Mtb* (*9*, *13*, *16*). We confirmed this observation by qRT-PCR and found that 5 mM H_2O_2 marginally induced (1.5- to 2.0-fold) *sufS* and *sufB* in WT *Mtb* and *MtbΔiscS* (fig. S12A). Notably, treatment with a bacteriostatic concentration of NO (0.5 mM DETA NO) induces an ~40- to 60-fold higher expression of *suf* genes (*sufS* and *sufB*) in WT *Mtb* and *MtbΔiscS* (fig. S12B). In contrast, NO reduces the expression of *iscS* (fig. S12B). However, at a bactericidal concentration of NO (2 mM DETA NO), the expression of *suf* genes was consistently higher in *MtbΔiscS* than in WT *Mtb* and *iscS-comp* (fig. S13A). We also performed qRT-PCR of *suf* genes on bacterial RNA isolated from immune-activated RAW264.7 infected with WT *Mtb* and *MtbΔiscS* in the presence or absence of iNOS inhibitor 1400W. Immune activation of macrophages induces the expression of *suf* genes by 100- to 300-fold in WT *Mtb* and 300- to 500-fold in *MtbΔiscS* (Fig. 8A). Inhibition of iNOS by 1400W uniformly represses the expression of *suf* genes to comparable levels in both strains (Fig. 8B).

On the basis of the above findings, we hypothesized that NO could be an environmental cue that induces *suf* genes, and the

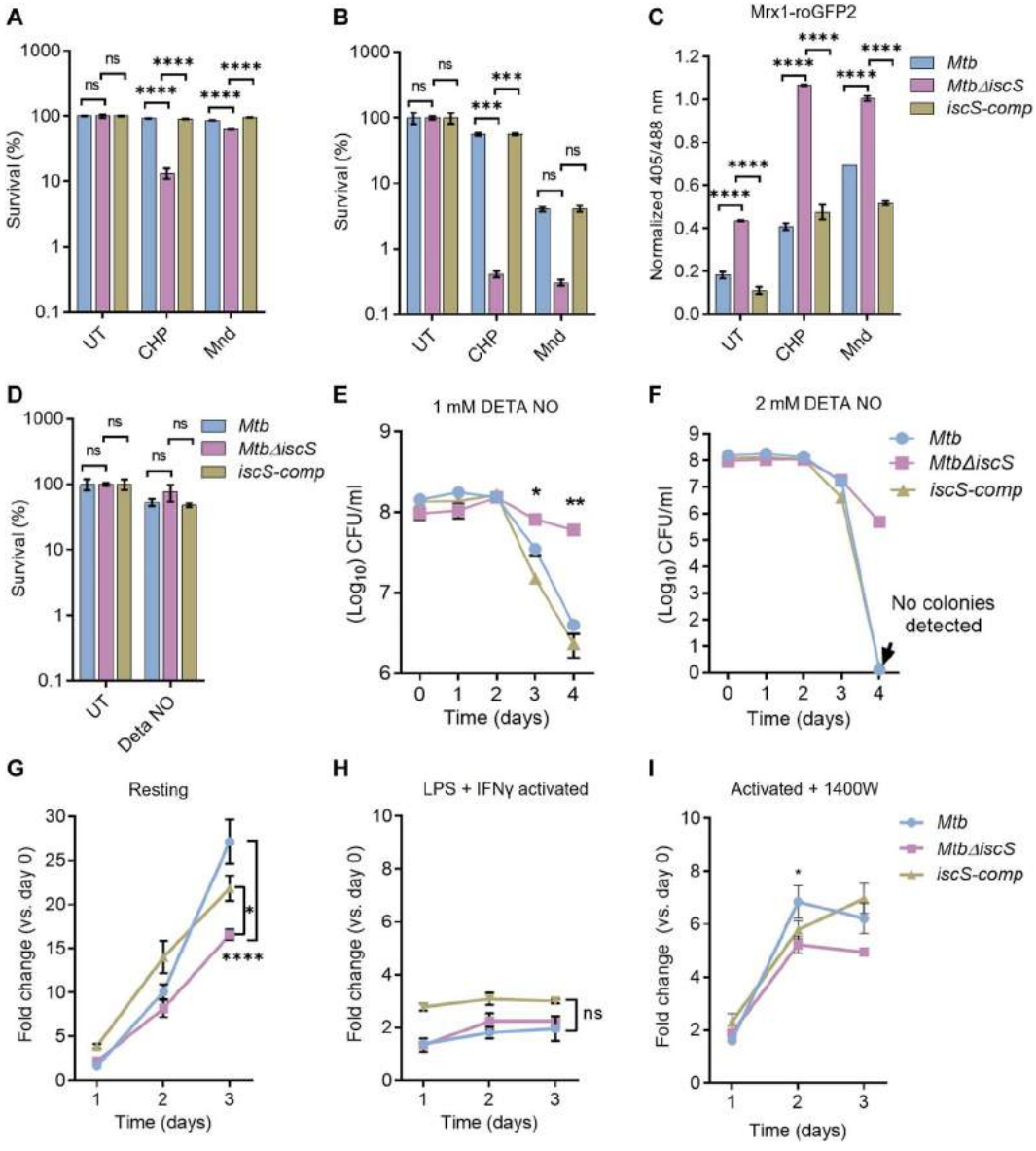

Fig. 6. IscS provides resistance to oxidative stress but not nitrosative stress in *Mycobacterium tuberculosis* (*Mtb*). (**A** to **C**) Exponentially grown cells of *Mtb*, *Mtb*Δ*iscS*, and *iscS-comp* with or without Mrx1-roGFP2 were exposed to 80 μM cumene hydroperoxide (CHP) and 60 μM menadione (Mnd), followed by enumeration of colony-forming units (CFUs) for survival after 4 hours (A) and 24 hours (B). (C) Mrx1-roGFP2 ratio was measured at 4 hours after treatment with CHP or Mnd. (**D**) Survival of *Mtb*, *Mtb*Δ*iscS*, and *iscS-comp* after 24-hour exposure to nitric oxide (NO) donor diethylenetriamine (DETA) NO (1 mM). (**E** and **F**) Survival of *Mtb*, *Mtb*Δ*iscS*, and *iscS-comp* after repeated exposure to NO donor DETA NO (1 and 2 mM) was tracked for 4 days by CFU enumeration. Raw CFU values are plotted. (**G**) Naïve, (**H**) Interferon-γ (IFN-γ) + lipopolysaccharide (LPS)–activated RAW264.7, and (**I**) activated + 1400W (iNOS inhibitor)–treated macrophage were infected with *Mtb*, *Mtb*Δ*iscS*, and *iscS-comp* at an multiplicity of infection (MOI) of 1:2 for 4 hours, and intramacrophage survival was monitored over time by CFU enumeration. Data are presented as means ± SEM. (A to I) $P \geq 0.05$, $^{*}P \leq 0.05$, $^{**}P \leq 0.01$, $^{***}P \leq 0.001$, and $^{****}P \leq 0.0001$ calculated by two-way analysis of variance (ANOVA) with Bonferroni's multiple comparisons test. ns, not significant.

absence of IscS results in a compensatory, albeit unregulated increase in the *suf* operon, leading to a higher bacillary load with *Mtb*Δ*iscS* in mice. To test the above possibilities, we measured the expression of *sufS* as a proxy for the *suf* operon in bacterial RNA extracted from the lungs of mice infected with *Mtb* strains at 56 days after infection. We observed that the expression of *sufS* was 6.5-fold induced in WT *Mtb* derived from animal lungs compared to in vitro grown *Mtb* (Fig. 8C). Consistent with our hypothesis, the transcript of *sufS* was ~600-fold greater in *Mtb*Δ*iscS* than in vitro grown mutant bacilli (Fig. 8C). The *iscS-comp* strain showed a partial reduction in *sufS* transcript as compared to *Mtb*Δ*iscS* (Fig. 8C), which is consistent with partial complementation noted above. Induction of NO production was evident in mice after 14 to 24 days of infection with *Mtb* (*53*). Therefore, we quantified *sufS* expression in the lungs of infected mice at 21 days after infection. The expression of *sufS* was induced twofold in WT *Mtb*, whereas a

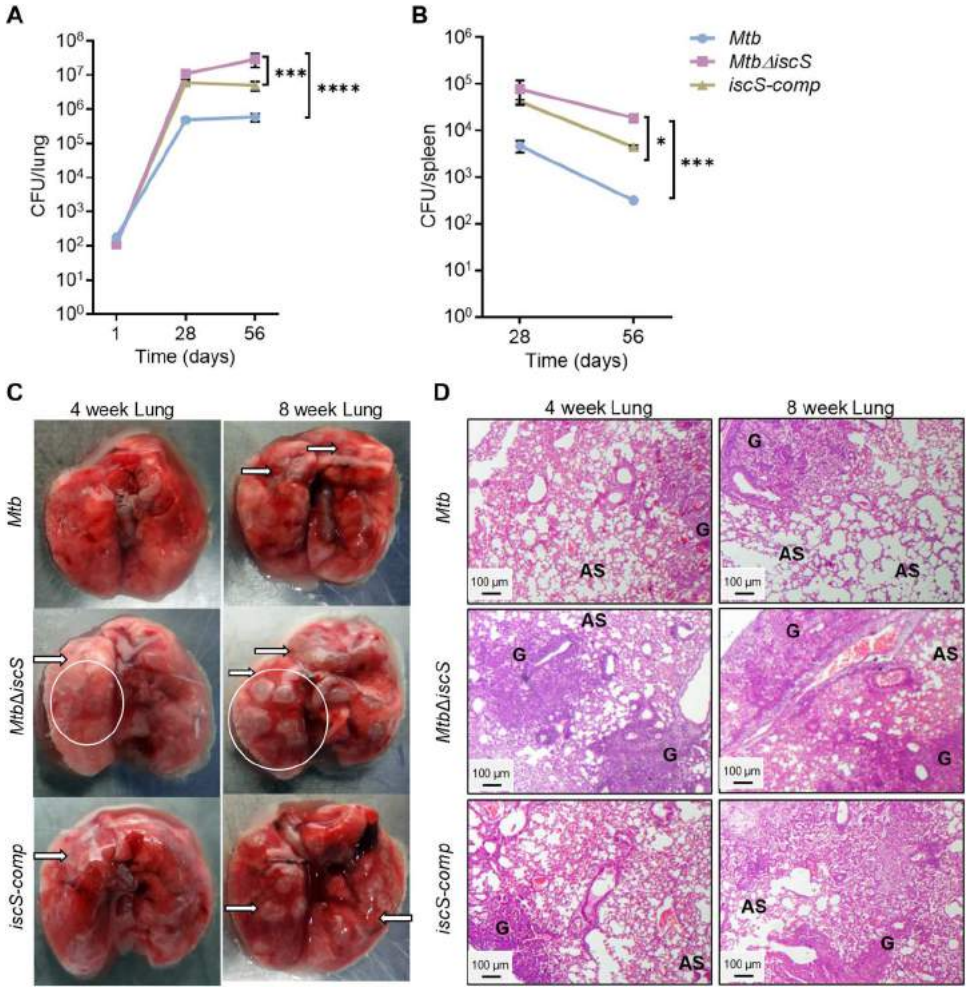

Fig. 7. *MtbΔiscS* displays hypervirulence in mice. BALB/c female mice ($n = 5$) were given aerosol challenge with *Mycobacterium tuberculosis* (*Mtb*) , *MtbΔiscS*, *and iscS-comp* and assessed for survival in (**A**) lungs and (**B**) spleen at indicated time points. (**C**) The gross pathology of the infected lungs is shown after 4 and 8 weeks of infection. Black arrows show the granulomatous lesions formed upon *Mtb* infection. The white circles highlight the patches of lung consisting of multiple granulomatous lesions in the *MtbΔiscS*-infected lungs. (**D**) Hematoxylin and eosin–stained lung sections were imaged (at ×4 magnification) and analyzed for histopathology on *Mtb* infection. Changes in lung morphology are shown with formation of granuloma (G) and the normal alveolar spaces (AS). (A) $P \geq 0.05$, $^{*}P \leq 0.05$, $^{***}P \leq 0.001$, and $^{****}P \leq 0.0001$ calculated by two-way analysis of variance (ANOVA) with Bonferroni's multiple comparisons test. (B) $^{*}P \leq 0.05$ and $^{***}P \leq 0.001$ calculated by unpaired two-tailed *t* test.

75-fold increase was detected in *MtbΔiscS* compared to in vitro grown conditions (Fig. 8D). To confirm that NO leads to the higher expression of the Suf system in mice, we infected a mouse strain lacking iNOS (iNOS$^{-/-}$) with WT *Mtb* and *MtbΔiscS*, extracted bacterial RNA from lungs at 4 weeks after infection, and examined the expression of *sufS*. We found that the expression of *sufS* was 40- and 90-fold down-regulated in WT *Mtb* and *MtbΔiscS* derived from the lungs of iNOS$^{-/-}$ mice as compared to in vitro grown bacteria, respectively (Fig. 8E). Consistent with these findings, we found that both the strains proliferated in mouse lungs without iNOS with no sign of hypervirulence exhibited by *MtbΔiscS* (Fig. 8F). The gross pathology of the lungs in both cases was comparable (fig. S14). While there was no difference in the bacillary burden for WT *Mtb* and *MtbΔiscS* in the lungs of iNOS$^{-/-}$ mice, we observed that the colonies of *MtbΔiscS* recovered from the lung homogenates of iNOS$^{-/-}$ mice were notably smaller than those of WT *Mtb*. The mutant colonies appeared only after 8 weeks of incubation as opposed to 2 to 3 weeks for WT *Mtb*. The reasons behind the delayed resumption of growth and small colony size of *MtbΔiscS* isolated from iNOS$^{-/-}$ mice need future experimentation. Our data suggest that *Mtb* preferentially mobilizes the Suf system under Fe-S cluster–damaging conditions such as NO in vivo and the hypervirulence of *MtbΔiscS* is associated with NO-dependent overexpression of the *suf* operon during infection in mice.

Depleting Suf system attenuates hypervirulence of *MtbΔiscS* during infection

We next sought to determine the impact of the *suf* operon on *MtbΔiscS*. Because the *suf* operon (*sufBCDSUT*) is essential (*7*), we interrupted its expression by anhydrotetracycline (ATc)–dependent CRISPRi-mediated depletion of *sufS* in WT *Mtb* and *MtbΔiscS* (fig. S15A) (*54*). Coexpression of *dCas9* (fig. S15B) and *sufS*-specific guide RNA (sgRNA) in response to ATc treatment uniformly

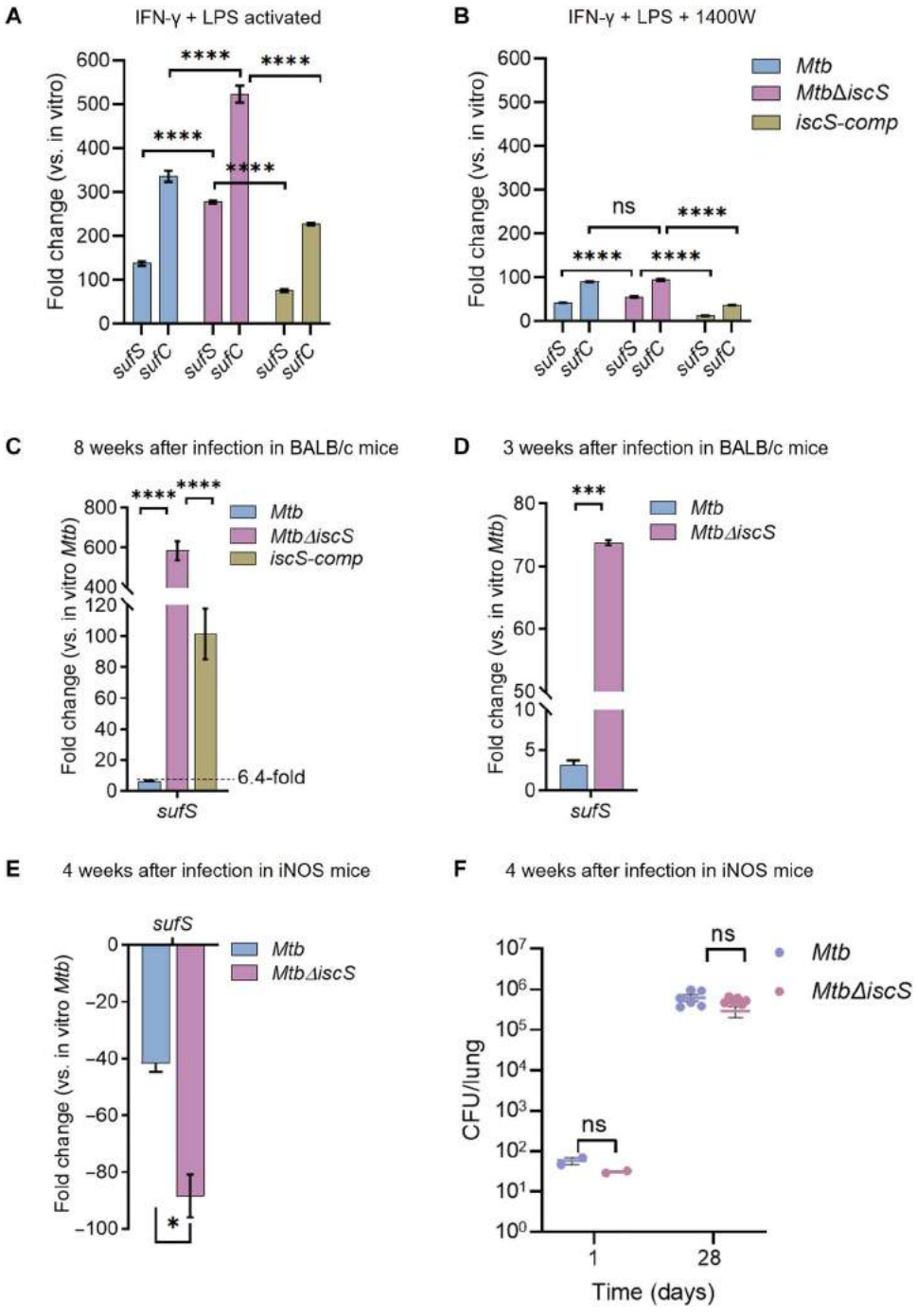

Fig. 8. Nitric oxide (NO) induces the expression of Suf system and contributes to hypervirulence of *MtbΔiscS* in mice. Gene expression analysis by quantitative reverse transcription polymerase chain reaction (qRT-PCR) of bacterial Suf genes (*sufS* and *sufC*) in *Mtb*, *MtbΔiscS*, and *iscS-comp* isolated from infected RAW264.7 murine macrophages (**A**) Lipopolysaccharide (LPS) + interferon-γ (IFN-γ) activated and (**B**) activated + iNOS inhibitor (1400W) after 48 hours of infection. (**C**) Gene expression of *sufS* was analyzed in *Mtb*, *MtbΔiscS*, *and iscS-comp* isolated from mouse lung after 8 weeks of infection. (**D**) Similarly, transcript levels of *sufS* were determined in *Mtb* and *MtbΔiscS* isolated from 3-week–infected mouse lung. (A and B) Fold change in transcript levels is compared to that of respective strains grown under standard in vitro conditions and compared to in vitro *Mtb* (C to D). Data are presented as means ± SEM. (**E** and **F**) iNOS$^{-/-}$ female mice ($n = 6$) were given aerosol challenge with *Mtb* and *MtbΔiscS* and assessed for survival in the lung after 4 weeks of infection. (F) Bacterial burden was determined by plating lung homogenates and colony-forming unit (CFU) enumeration. (E) The transcript levels of *sufS* were estimated in *Mtb* and *MtbΔiscS* isolated from 4-week–infected lungs of iNOS$^{-/-}$ mice. (A, B, and F) ****$P \leq 0.0001$, calculated by two-way analysis of variance (ANOVA) with Bonferroni's multiple comparisons test. (C to E) Statistical significance was analyzed over untreated control by paired two-tailed *t* test (**$P < 0.01$ and ****$P < 0.0001$). ns, not significant.

reduced (~10-fold) the expression of *sufS* and downstream genes *sufU* and *sufT* in WT *Mtb* (*sufS*-KD) and *Mtb*Δ*iscS* (Δ*iscS*-*sufS* KD) (fig. S15, C and F). A ~10-fold reduction in *sufS* did not affect the survival of *sufS*-KD under aerobic growth conditions (fig. S15D) or in response to 5 mM H_2O_2 (fig. S15E). In contrast, Δ*iscS*-*sufS* KD grew slower than *Mtb*Δ*iscS* under aerobic conditions, and treatment with 5 mM H_2O_2 for 24 hours reduced the survival of Δ*iscS*-*sufS* KD by ~150- and 20,000-fold as compared to *Mtb*Δ*iscS* and WT *Mtb*, respectively (fig. S15, D and E). These data suggest that in the absence of IscS, *Mtb* uses the Suf system to sustain aerobic growth and survive H_2O_2 challenge. Expression of Suf system depends on a 4Fe-4S cluster containing the transcription factor SufR (*10*). Under Fe-S cluster–deficient conditions (e.g., NO and low iron), the cluster-less form of SufR (apo-SufR) derepresses the expression of the Suf system (*10*). We substantiated the compensatory role of the Suf system in the absence of IscS by examining the relative expression of the *suf* operon in WT *Mtb*, *Mtb*Δ*iscS*, *sufS*-KD, and Δ*iscS*-*sufS* KD by RNA-seq. Defects in both *iscS* and *sufS* (Δ*iscS*-*sufS* KD) induced the expression of the *suf* operon, which is higher than *Mtb*Δ*iscS* and marginally supersedes *sufS*-KD as compared to WT *Mtb* (fig. S15F). These findings demonstrate that Δ*iscS*-*sufS* KD is severely impaired in building Fe-S clusters, which results in defective aerobic growth and hypersensitivity to H_2O_2.

We infected BALB/c mice with the *sufS*-KD and Δ*iscS*-*sufS* KD strains by aerosol. As previously reported (*11*), we initiated SufSUT depletion in both strains at day 7 after infection to assess acute-phase phenotype and for the chronic phase at day 21 after infection by feeding doxycycline (Fig. 9A), a tetracycline derivative commonly used for gene silencing in vivo (*11*). The *sufS*-KD strain that retained IscS, but depleted SufSUT, showed the lowest lung bacillary load during both the acute and chronic phases of infection (Fig. 9, B and C). The Δ*iscS*-*sufS* KD mutant that lacked IscS and had depleted SufSUT exhibited a lung bacillary load intermediate between that of the severely attenuated *sufS*-KD and hypervirulent *Mtb*Δ*iscS* (Fig. 9, B and C). The bacterial burden of Δ*iscS*-*sufS* KD was similar with that of WT *Mtb* (Fig. 9, B and C). The gross and histopathological changes observed in the lungs of chronically infected mice were proportionate with the bacillary load observed (Fig. 9, D and E). The extent of pulmonary tissue destruction was highest in animals infected with *Mtb*Δ*iscS*, intermediate in WT *Mtb* and Δ*iscS*-*sufSKD* (score, ~15), and lowest in *sufS*-KD (score, 3.5) (fig. S16A). Thus, overinduction of the *suf* operon is likely responsible for the hypervirulence of *Mtb*Δ*iscS* in mice.

DISCUSSION

Mtb expresses a nearly complete Suf system, thereby satisfying the demand for de novo Fe-S cluster assembly under normal growth conditions and repair in response to stress (*10*, *11*). Why *Mtb* retained a single gene (IscS) of the ISC system was initially unclear. The genetic, biochemical, and infection experiments described above show that IscS is required for maintaining redox balance, bioenergetics, antibiotic susceptibility, resistance to ROS, and survival inside macrophages. In the context of infection, deletion of IscS led to hypervirulence in mice, a phenotype linked to uncontrolled induction of the Suf system in response to NO. Our data indicate that *Mtb* uses the IscS and Suf systems to attain an intermediate degree of virulence that is critical for persistence.

Earlier transposon mutagenesis studies indicated that IscS is essential for *Mtb* (*55*). However, this is not the case, although IscS promotes optimal overall growth of *Mtb*. Previous studies were done at a subsaturating level, requiring statistical tools for downstream data processing to estimate essentiality. This affected the ability to assess the essentiality of many genes, including IscS, reliably. Consistent with this, a follow-up study used a completely saturated transposon library more authoritative cataloging of essential genes in *Mtb* and confirmed that *Mtb* IscS is not essential (*56*). Generally, Fe-S cluster biogenesis occurs during de novo assembly on the nascent apoproteins and repair of damaged Fe-S clusters (*57*). Similar to the IscS mutant of *E. coli* (*19*), assessment of *Mtb*Δ*iscS* indicated that most of the phenotypes exhibited by the mutant are likely due to inadequate de novo assembly rather than an inability to repair oxidized clusters. For example, when cells grow aerobically, the Fe-S clusters appear to be more sensitive to oxidative damage than in anaerobic conditions. Therefore, if IscS is functioning through the repair of oxidatively damaged Fe-S clusters, then the general growth defect of *Mtb*Δ*iscS* should show a greater dependence on oxygen. However, *Mtb*Δ*iscS* exhibited impaired survival under both aerobic and hypoxic conditions. Furthermore, *Mtb*Δ*iscS* accumulates ROS, which is known to convert $[4Fe\text{-}4S]^{2+}$ clusters to $[3Fe\text{-}4S]^{1+}$ clusters (*19*, *33*). The 3Fe-4S clusters can be repaired back to 4Fe-4S clusters upon scavenging of ROS without a requirement for either cysteine desulfurase or a sulfur source (*19*). In contrast, the reduction in ROS levels of *Mtb*Δ*iscS* by Thio did not restore the aerobic growth defect of the mutant. In the absence of IscS, *Mtb* likely accumulates incomplete Fe-S clusters that lack sulfur atoms, which differ from oxidatively damaged Fe-S clusters. Consistent with this idea, the pool of unincorporated intracellular iron was elevated in *Mtb*Δ*iscS*. Free iron could cause ROS accumulation in *Mtb*Δ*iscS* via the Fenton reaction (*26*). However, in contrast to our expectations, ROS accumulation and the slow growth defect were accentuated upon treatment of *Mtb*Δ*iscS* with an iron chelator. These results suggest that ROS increase in *Mtb*Δ*iscS* is not a consequence of free iron. We have recently shown that increased $NADH/NAD^+$ ratio and NADH-reductive stress are critical for iron-mediated ROS surge (*58*). *Mtb*Δ*iscS* showed neither an increased NADH pool nor higher $NADH/NAD^+$ poise, which suggests that iron accumulation is unlikely to drive ROS generation in the mutant. Because iron is a cofactor for several antioxidant enzymes (e.g., superoxide dismutase and catalase) (*59*, *60*), ROS accumulation could be due to disruption of their activities upon iron limitation. A possible explanation for the elevated oxidative stress upon iron chelation in *Mtb*Δ*iscS* is an impairment of the metabolic and respiratory functions, mainly due to reduced synthesis of Fe-S clusters for enzymes of the TCA cycle and respiratory chain. Similarly, dysfunction of mechanisms that prevented the assembly of mitochondrial Fe-S cluster led to ROS accumulation and DNA damage (*61*).

The slow-growth phenotype of *Mtb*Δ*iscS* was expected because several metabolic enzymes and respiratory complexes contain Fe-S clusters. Consistent with this, *Mtb*Δ*iscS* had diminished glycolytic, PPP, and TCA cycle intermediate pool. These results aligned well with impaired oxygen consumption, reduced glycolysis, and reductant levels (NADH/NADPH) in *Mtb*Δ*iscS*. Surprisingly, despite a previous study showing ~50% reduction in aconitase and succinate dehydrogenase activities in *Mtb*Δ*iscS* (*17*), the respective substrates and products of these enzymes remain unaltered in the mutant. One possibility is that the residual activity of aconitase and succinate

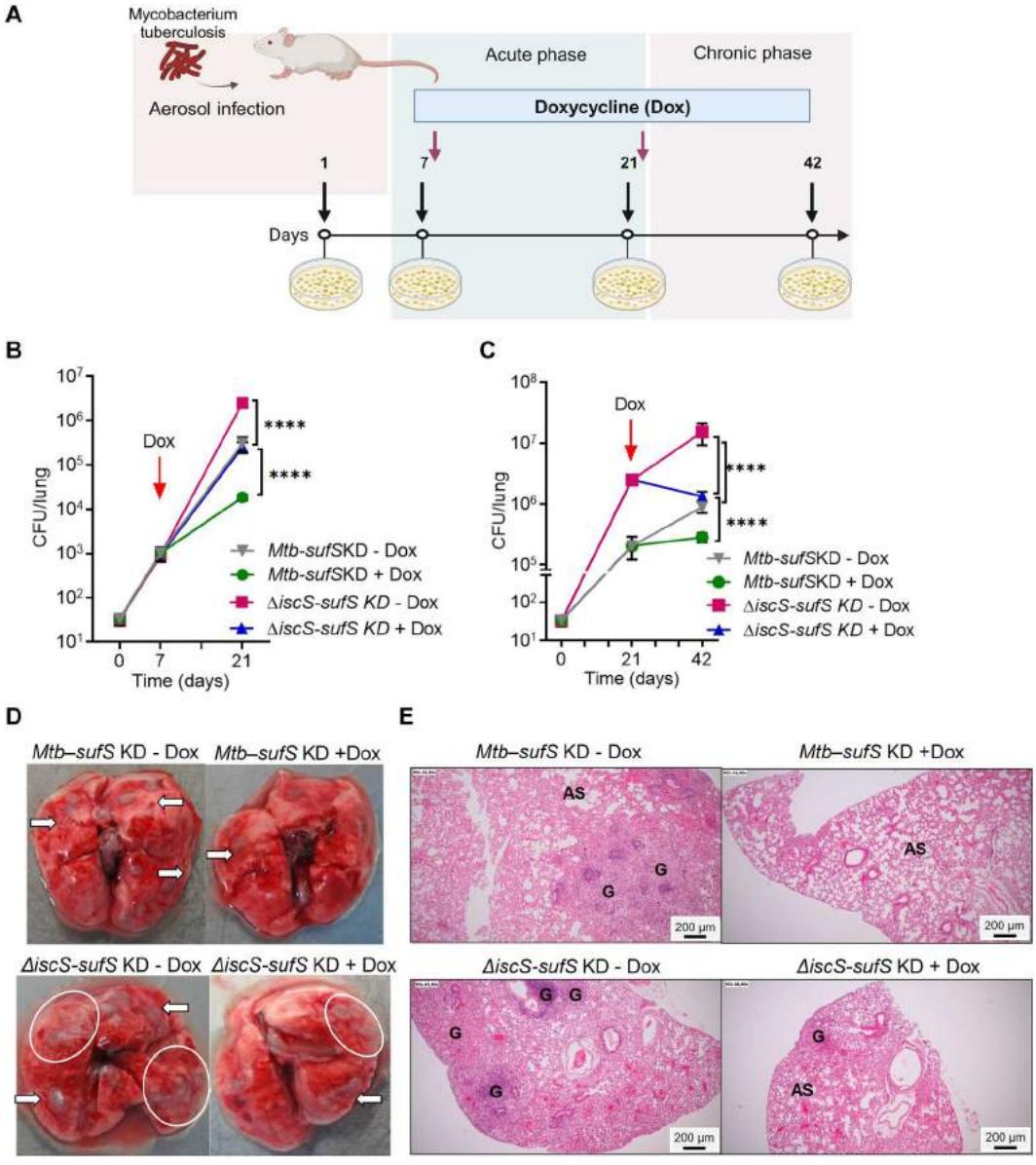

Fig. 9. Overexpression of Suf system contributes to hypervirulence of *MtbΔiscS* in mice. (**A**) BALB/c mice ($n = 5$) were given aerosol challenge with *Mtb-sufS*KD and Δ*iscS-sufS*KD and divided into three groups of (i) no doxycycline treatment (−Dox), (ii) acute phase [doxycycline started at 7 days after infection (+Dox acute)], and (iii) chronic phase [doxycycline started at 21 days after infection (+Dox chronic)] (credit: BioRender.com). Post-infection animals were sacrificed from the (**B**) acute group at days 7 and 21 and (**C**) at days 21 and 42 from the chronic group, and colony-forming unit (CFU) per lung was measured. (**D**) Gross pathology of *Mtb-sufS*KD and Δ*iscS-sufS*KD–infected lungs at 42 days after infection. White arrows and white circles show the granulomatous lesions formed upon *Mycobacterium tuberculosis* (*Mtb*) infection. (**E**) Hematoxylin and eosin–stained lung sections were imaged (at ×40 magnification) and analyzed for histopathology on *Mtb* infection. Changes in lung morphology are shown with formation of granuloma (G) and the normal alveolar spaces (AS). (B and C) ****$P \leq 0.0001$, calculated by two-way analysis of variance (ANOVA) with Bonferroni's multiple comparisons test.

dehydrogenase is due to the Suf system. Alternatively, in the absence of IscS, *Mtb* could attempt to restore metabolism by operating the TCA cycle in the reverse direction. This appears to be partially successful and could have resulted in the restoration of citrate, α-KG, and oxaloacetate in *MtbΔiscS*. However, accumulation of fumarate and reduction in succinate and malate indicate the impaired activity of a reverse TCA cycle enzyme fumarate reductase, which contains an Fe-S cluster (*39*), and a canonical TCA enzyme fumarate hydratase in *MtbΔiscS*, respectively. Our RNA-seq data confirm that genes expressing fumarate reductase are down-regulated in *Mtb*, which could be another reason why fumarate reductase activity is likely more affected than succinate dehydrogenase.

The gene encoding fumarate hydratase was unaffected in the mutant. The fumarate hydratase catalyzes the stereospecific hydration of fumarate to malate and is essential for *Mtb's* survival in vitro and in vivo (*62*). At least two possible mechanisms could link fumarate hydratase with redox balance and Fe-S cluster biogenesis in *Mtb*. First, fumarate hydratase maintains redox homeostasis by

preventing fumarate accumulation and subsequent covalent modification of mycothiol and thiol-containing proteins via succination in *Mtb* (*62*). Second, in mammalian cells, proteins involved in Fe-S cluster biogenesis and respiration are sensitive targets of succination, directly linking fumarate hydratase functionality with Fe-S cluster biogenesis and bioenergetics (*63*). Additional experiments are needed to determine whether IscS activity is regulated by fumarate hydratase and succination in *Mtb*.

While any of the above Fe-S cluster–dependent mechanisms could have contributed to the slow growth rate of *Mtb*Δ*iscS*, other cellular functions requiring IscS as a sulfur donor, such as the thiolation of tRNA, might contribute to these metabolic phenotypes. In this context, IscS exists in an operon with *trmU*, which encodes 2-thiouridylase. This enzyme is known to catalyze the formation of 2-thiourdine *in E. coli* tRNA (*64*). While IscS physically associates with TrmU, deletion of *trmU* neither reduced aconitase activity nor affected the survival of *Mtb* under H_2O_2 stress (*17*). However, our transcriptomics data suggest that *trmU* expression remained downregulated in *Mtb*Δ*iscS* and showed only partial restoration in *iscS-comp*, which could explain incomplete complementation of the mutant phenotypes in some of our assays. A more careful examination is needed to decipher the role of IscS and TrmU in the sulfur metabolism of *Mtb*.

Our metabolomics and transcriptomics data provide insight into why *Mtb* harbors a truncated ISC system in the backdrop of a complete SUF pathway. Both IscS and Suf systems are expressed and contribute to enzymatic activities of the Fe-S cluster proteins aconitase and succinate dehydrogenase under normal growth conditions (*11*, *17*). However, the absence of IscS mainly affected metabolites unrelated to Fe-S cluster enzymes (e.g., glycolysis and PPP), except for the TCA cycle enzyme fumarate reductase. In contrast, depletion of SufT resulted in an altered pool of many metabolites directly or indirectly dependent on Fe-S cluster enzymes (*11*). These observations explain why the Suf system is essential for the growth of *Mtb,* whereas disruption of IscS only slows growth under aerobic conditions. Because the expression of the Suf system was maintained in *Mtb*Δ*iscS*, the residual metabolic, redox, and bioenergetic activities in the mutant could be due to the action of the Suf system.

The connection between the Suf system and IscS becomes clearer under conditions that highly induce the *suf* operon. NO treatment induces an elevated and long-lasting expression of the *suf* operon in *Mtb* (*9*), which remained comparable in *Mtb*Δ*iscS* (Fig. 8B). In contrast, hypoxia represses the *suf* operon (*65*). In line with this, nitrosative stress did not affect *Mtb*Δ*iscS*, whereas hypoxic conditions reduced survival of *Mtb*Δ*iscS*. In general, mild oxidizing conditions, such as low concentrations of H_2O_2 or O_2, oxidize a $[4Fe\text{-}4S]^{2+}$ cluster to a $[3Fe\text{-}4S]^{+}$ cluster that can be repaired back to the original $[4Fe\text{-}4S]^{2+}$ under reducing conditions in the presence of ferrous ion (*6*). For these environmental situations, basal expression of both IscS and Suf is sufficient. However, for proteins whose clusters are degraded beyond the $[3Fe\text{-}4S]^{+}$ state or to apo-form or dinitrosyl-iron dithiol complex (DNIC), wherein the sulfide ligands of the 4Fe-4S clusters were displaced by NO to form $[Fe\text{-}(NO)_2]$, sulfur atoms must be supplied by inducing de novo–style Fe-S cluster biogenesis pathways for rebuilding the Fe-S clusters (*6*, *10*). This seems to be the case with *Mtb*, wherein the expression of the *suf* operon is repressed by a 4Fe-4S cluster containing SufR (holo-SufR) under standard aerobic growth conditions. At the same time, cluster-less SufR (apo-SufR) derepresses Suf expression (*10*). The 4Fe-4S cluster of SufR is resistant to mild oxidizing conditions (O_2) (*10*). NO or high molar concentrations of H_2O_2 rapidly damage 4Fe-4S of SufR to DNIC or apo-form, respectively, resulting in the de-repression of the *suf* operon in vitro and in vivo (*10*). In this context, data using iNOS inhibitor and $iNOS^{-/-}$ mice confirm the induction of the *suf* operon in response to NO during infection of macrophages and mice. The absence of a survival defect of *Mtb*Δ*iscS* when inside the immune-activated murine macrophages suggests that the NO/H_2O_2-driven induction of *suf* operon might compensate for the loss of IscS. Consistent with this observation, we showed that residual survival of *Mtb*Δ*iscS* under aerobic or H_2O_2 stress is due to the expression of the *suf* operon.

Our phenotypic data suggest that IscS and Suf systems work in distinct ways. *Mtb* requires IscS system more under hypoxic conditions where the demand for Fe-S clusters is minimal. As the demand for Fe-S cluster increases, such as during growth in an oxygen-rich environment, H_2O_2, and upon exposure to NO stress, *Mtb* gradually shifts its reliance from IscS to Suf for maintaining Fe-S cluster homeostasis and survival. The *E. coli* Isc system is generally poisoned with as low as 1 μM H_2O_2, whereas the Suf system remains resistant to oxidative stress (*6*). Similar differences in sensitivity to oxidants are expected for *Mtb* IscS and Suf systems (*10*, *11*, *17*). However, the artificial overproduction of IscS suppresses the growth defect of *Mtb*Δ*iscS* and renders the mutant more resistant to H_2O_2 than WT *Mtb* (*17*). Thus, in principle, the induction of SUF/ISC pathways elevates the total cellular capacity for cluster assembly during high-demand conditions rather than being intrinsically more resistant to H_2O_2 or NO. Agreeing with this, overexpression of the Suf system in *Mtb*Δ*iscS* inside murine lungs increased bacillary load and pathological defects more than WT *Mtb*.

During infection in mice, *Mtb* is exposed to a more potent RNI-peroxynitrite that primarily damages Fe-S clusters with a high-rate constant ($\sim 1.0 \times 10^{10}\ M^{-1}\ s^{-1}$) (*66*). While NO largely induces the Suf operon to the same level in WT *Mtb* and *Mtb*Δ*iscS* in vitro, peroxynitrite exposure during murine infection could have caused additional damage to Fe-S cluster proteins including SufR in the mutant, leading to more induction of Suf system in *Mtb*Δ*iscS* and hence hypervirulence. This agrees with our findings showing both the loss of *suf* inducibility and hypervirulence phenotype of *Mtb*Δ*iscS* in $iNOS^{-/-}$ mice lacking the ability to produce peroxynitrite. Consistent with a dominant role of the Suf system during stress, organisms that are routinely exposed to H_2O_2 (e.g., lactic acid bacteria, *Enterococcus faecalis*, *Xylella fastidiosa,* and chloroplasts) rely upon Suf rather than ISC for cluster assembly (*6*, *67*, *68*). While true for other organisms, *Mtb's* persistence depends upon an adequate response toward oxidative/nitrosative stress and hypoxia. Therefore, the importance of IscS in mediating the response to hypoxia in vitro and suppressing hypervirulence by adjusting Suf expression in vivo provides the biological significance of IscS in the persistence of *Mtb*. This notion must be tested in animal models (e.g., guinea pigs and nonhuman primates) (*69*), exposing *Mtb* to hypoxic lesions during infection.

MATERIALS AND METHODS

Bacterial strains and culture conditions

The *Mtb*Δ*iscS* and *iscS-comp* ($pHsp_{60}$) strains were gifts from S. T. Cole (Pasteur Institute, Paris, France). The *iscS-comp* was constructed for this study by cloning 500–base pair (bp) upstream

region of *iscS* into the integrative plasmid pCV125. *Mtb*-roGFP2 strain was generated by transforming *Mtb* strains with an *E. coli*–mycobacterial shuttle vector, pMV762-Mrx1-roGFP2 (biosensor construct), with hygromycin resistance gene as selection marker (*22*). All mycobacterial strains were grown in Middlebrook 7H9 broth (Becton, Dickinson and Company, USA) liquid medium supplemented with 0.2% glycerol, 0.05% Tween 80, and ADS (0.5% albumin, 20% dextrose, and 0.085% NaCl) or OADC (ADS plus 0.05% oleic acid and 0.004% catalase) with shaking at 180 rpm in a shaker incubator (Lab Therm LT-X, Kuhner, Basel, Switzerland) or on 7H11 agar (solid medium) supplemented with ADS or OADC at 37°C. As per the requirement, antibiotics were added to the culture medium at a concentration of kanamycin (KAN; 25 μg/ml) (Amresco, USA) and hygromycin (HYG; 50 μg/ml) (MP Biomedicals, Santa Ana, CA). *E. coli* DH5α strains were grown in LB broth/agar (Himedia, India) with antibiotic concentrations of KAN (50 μg/ml) and HYG (100 μg/ml).

Measurement of E_{MSH} using the Mrx1-roGFP2 redox biosensor

The intra-mycobacterial E_{MSH} (defined as the standard reduction potential of the $MSH_{reduced}/MSSM_{oxidized}$ redox couple) determination during in vitro growth of *Mtb*, *Mtb*Δ*iscS*, and *iscS-comp* was performed as in (*22*). Briefly, bacterial cultures expressing Mrx1-roGFP2 were treated with 5 mM *N*-ethylmaleimide (Sigma-Aldrich, St. Louis, MO) for 5 min at room temperature followed by 4% paraformaldehyde (PFA) fixation (Himedia, Mumbai, India) for 1 hour at room temperature. Bacteria were analyzed using a FACSVerse flow cytometer (BD Biosciences, San Jose, CA). The E_{MSH} was calculated using the Nernst equation as described previously in (*22*). The biosensor response was quantified by measuring the fluorescence ratio at a fixed emission (510 nm) on excitation at 405 and 488 nm. The data obtained were analyzed with the BD FACSuite software. These ratiometric data were normalized to measurements of cells treated with 10 mM CHP (Sigma-Aldrich, St. Louis, MO), giving maximal oxidation of the biosensor, and 20 mM dithiothreitol (Sigma-Aldrich, St. Louis, MO), yielding a readout of maximal reduction of the biosensor. Ten thousand events per sample were analyzed. Biosensor response was measured in a similar way for bacterial cells exposed to ROS (80 μM CHP or 60 μM Mnd) after 4-hour treatment.

ROS measurement using CellROX deep red

Exponentially growing cultures of *Mtb*, *Mtb*Δ*iscS*, and *iscS-comp* were taken for measurement of intracellular ROS. According to the manufacturer's instructions, CellROX Deep Red (Invitrogen, Waltham, MA) was added to a final concentration of 5 μM, and cells were stained by incubating on a rocker for 30 min at 37°C. The cells were then washed with 1× phosphate-buffered saline (PBS; pH 7.4) to remove residual dye by centrifugation (5000 rpm for 5 min). Last, cells were resuspended in 300 μl of PBS and fixed using 4% PFA for 1 hour at room temperature. Fluorescence was measured using a BD FACSVerse flow cytometer (BD Biosciences, San Jose, CA) at a fixed emission maxima of 670 nm allophycocyanin (APC) channel) after excitation with a red laser (640 nm) for 10,000 events per sample. No autofluorescence was observed.

For determination of intracellular ROS in the presence of Bip and Thio, exponentially grown cultures at an initial OD_{600} (optical density at 600 nm) of 0.6 (10 ml) were treated with 250 μM Bip and 10 mM Thio separately and incubated for 24 hours in a shaker incubator (180 rpm, 37°C). This was followed by the above procedure for CellROX Deep Red staining and ROS measurement.

Cellular iron estimation

Intracellular iron levels were measured using the ferrozine-based colorimetric assay described previously (*70*, *71*). Briefly, exponentially grown cultures of *Mtb* strains (OD_{600} ~ 0.8) were harvested by centrifugation and washed twice with ice-cold PBS. The cell pellets were resuspended in 1 ml of 50 mM NaOH and lysed using a bead beater (MP Biomedicals, Santa Ana, CA). HCl (10 mM, 300 μl) was added to the cell lysate samples (300 μl), followed by the addition of the Fe-detection reagent (6.5 mM ferrozine, 6.5 mM neocuproine, 1 M ascorbic acid, and 2.5 M ammonium acetate in water) (90 μl). This reaction mix was incubated for 30 min at 37°C, followed by reading the absorbance of the samples at 562 nm using a microplate reader (Versa-Max; Molecular Devices, San Jose, CA). The cellular free iron concentration was equated by plotting the absorbance values against a standard curve of $FeCl_3$ concentration gradient and readouts normalized to the protein content of the respective samples. Protein concentration was estimated using a Pierce bicinchoninic acid (BCA) protein assay kit (Thermo Fisher Scientific, Rockford, IL).

Determination of bacterial survival

The number of viable bacilli was determined after treatment with 250 μM iron chelator Bip or 10 mM ROS scavenger Thio by removing aliquots from the cultures followed by preparation of 10-fold dilutions. Twenty microliters of dilutions was trailed on 7H11 agar plates. Plates were incubated for 3 to 5 (for *Mtb*Δ*iscS*) weeks at 37°C, followed by CFU enumeration.

Establishment of hypoxia

To determine the viability of *Mtb*, *Mtb*Δ*iscS*, and *iscS-comp* under hypoxic conditions, bacterial cultures (OD_{600} = 0.1) were injected into vacutainer tubes (Becton Dickinson, Franklin Lakes, NJ) followed by incubation at 37°C for 12 to 16 days (*58*, *72*). A marker for the achievement of hypoxia was the decoloration of MB (final concentration of 1.5 μg/ml) (Sigma-Aldrich, St. Louis, MO) in the culture medium. Once hypoxia was established, cells were harvested for determination of bacterial survival by CFU.

Growth curves for *Mtb* strains

Freezer stocks of *Mtb* strains were revived in 7H9-OADC broth with 1:10 dilution and grown for 1 week. These cultures were subcultured and inoculated in 7H9-ADS at OD_{600} ~ 0.05 and incubated at 37°C at 180 rpm, and growth was tracked for 8 to 9 days by measuring the OD_{600} until the cultures reached a stationary phase.

Aconitase activity

The aconitase activity was measured by monitoring the disappearance of *cis*-aconitate at wavelength (λ) 240 nm in an ultraviolet spectrophotometer (Thermo Fisher Scientific, Biomat 3S, USA) as described (*11*). One unit of aconitase activity is defined as 1 μmol of *cis*-aconitate formed or converted per minute. Reaction mixtures for aconitase assay contained 25 mM tris-HCl (pH 8.0), 100 mM NaCl, and 50 μg of *Mtb* cell lysates in 1 ml of reaction volume. Reaction was initiated by adding 0.15 mM *cis*-aconitate and monitored

by following the disappearance of *cis*-aconitate at λ 240 nm after every 15 s for 30 min. Absorbance at λ 240 nm was plotted against time. Aconitase activity was calculated from linear portion of the curve in initial 5 min. An extinction coefficient of 3500 M^{-1} cm^{-1} was used to calculate the rates.

Metabolite extraction and analysis

Metabolite extraction from all *Mtb* strains was performed as outlined in (*11*). Briefly, exponentially growing *Mtb*, *Mtb*Δ*iscS*, and *iscS-comp* cultures (OD_{600} ~ 0.6) were quenched with four volumes of 60% methanol for 5 min (maintained at −45°C) in a dry ice-methanol bath, followed by centrifugation at 4000 rpm for 5 min (at −5°C). The pellet was resuspended in 700 μl of 60% methanol (maintained at −45°C) and centrifuged at 4000 rpm for 5 min. The pellet obtained was resuspended in 1 ml of 75% ethanol and incubated at 80°C for exactly 3 min, with intermittent mixing at 1.5-min intervals, followed by incubation on ice for 5 min and centrifugation at 13,000 rpm for 15 min. The final supernatant was lyophilized and then stored at −80°C until further analysis.

Steady-state levels of metabolites were analyzed using methods described in (*73*). Briefly, extracted metabolites were first separated using a Synergi 4-μm Fusion-RP 80 Å (150 × 4.6 mm, Phenomenex) LC column on the Shimadzu Nexera ultrahigh-performance LC system. For TCA intermediates, derivatization was done before separation. The following solvent systems were used: 0.1% formic acid in water (solvent A) and 0.1% formic acid in methanol (solvent B) for amino acids, nucleotides, and TCA metabolites and 5 mM ammonium acetate in water (solvent A) and 100% acetonitrile (solvent B) for sugar phosphates. The flow parameters used were as described in (*73*). The mass spectrometer used was AB Sciex Qtrap 5500, and data acquisition was made by Analyst 1.6.2 software (Sciex). Amino acids and TCA intermediates were detected in positive polarity, while sugar phosphates were detected in negative polarity mode. The parent and daughter ion masses for each metabolite are given in table S3. The data were analyzed by calculating the area under the obtained peaks by using Multi Quant (version 3.0.1) software.

Estimation of NAD^+, NADH, $NADP^+$, and NADPH

Mtb strains were grown to OD_{600} ~ 0.8 and harvested for the detection of pyridine nucleotide levels by a redox-cycling assay as described in (*74*, *75*). NADPH and $NADP^+$ concentrations were normalized to the protein contents of NADH and NAD^+ extracts using BCA protein assay.

OCR and ECAR measurements

To estimate the basal OCR and ECAR, *Mtb*, *Mtb*Δ*iscS*, and *iscS-comp* cultures of OD_{600} ~ 0.6 were briefly (24 hours) incubated in 7H9 medium containing the nonmetabolizable detergent tyloxapol (MP Biomedicals, Santa Ana, CA) and devoid of ADS or any carbon source. These cultures were then harvested, and single-cell suspensions of bacteria were prepared by passing five times through a 26-gauge syringe needle followed by centrifugation at 100*g* for 1 min. Cells (2×10^6 per well) were seeded into the wells of an XF cell culture microplate (Agilent/Seahorse Biosciences, Santa Clara, CA) coated with Cell-Tak (Corning, Corning, NY). Measurements were carried out using a Seahorse XFp analyzer (Agilent Technologies, CA) with unbuffered 7H9 as the assay media (pH 7.35; lacking disodium phosphate and monopotassium phosphate). Basal readings were taken for an initial 18 min, followed by an injection of D-glucose (10 mM), giving glucose-induced respiration rates. The maximum rate of respiration was achieved by the addition of two consecutive doses of 2 and 8 μM CCCP (Sigma-Aldrich, St. Louis, MO). Readouts were normalized to the number of bacteria seeded.

RNA isolation, amplification, and library preparation for RNA-seq

Mtb strains grown to an OD_{600} of 0.4 were harvested in 5 M guanidinium thiocyanate (GTC) buffer (containing 1% 2-mercaptoethanol, 0.5% sarcosyl, and 0.5% Tween 80) for total RNA extraction. Total RNA was extracted using a FastRNA Pro Blue kit (MP Biomedicals, USA) and further purified with RNeasy spin columns (Qiagen, USA) as described (*14*). The concentration and quality of extracted RNA were checked spectrophotometrically using NanoDrop ND-1000 (Thermo Fisher Scientific). Total RNA was then enriched for mRNA by depletion of 16*S* and 23*S* rRNA using the MICROBExpress Kit (Life Technologies, USA), and the concentration of the ribo-depleted RNA was quantified by the QuBit RNA HS Assay Kit (Life Technologies). Fifteen nanograms of mRNA per sample was taken for fragmentation and random priming, followed by first and second cDNA synthesis and library preparation using the NEBNextUltra II Directional RNA Library Prep Kit for Illumina (New England Biolabs), according to the manufacturer's protocol. The library size distribution and quality were assessed using a high-sensitivity DNA chip (Agilent Technologies). Last, equimolar quantities of all libraries were pooled and sequenced in a high-throughput run on the Illumina HiSeq 2500 sequencer (*14*).

Differential gene expression and statistical analysis for RNA-seq

The reference genome sequence (.fna) and annotation (.gff) files for the *Mtb* H37Rv strain (accession number: NC_000962.3) were downloaded from the National Center for Biotechnology Information (NCBI) ftp website ("ftp.ncbi.nlm.nih.gov"). The annotation file format (.gff) was changed to .bed using an in-house Python script. Sequencing-based raw reads obtained (as .fastq) were checked for quality using FastQC software (version v0.11.5; http://www.bioinformatics.babraham.ac.uk/projects/fastqc). BWA (version 0.7.12-r1039) (*76*) was used to index the reference genome. Reads having raw read quality of ≥20 were aligned using the BWA aln -q option. SAMTOOLS (version 0.1.19-96b5f2294a) (*77*) was used to filter out the multiple mapped reads. Read count per gene was calculated using BEDTOOLS (version 2.25.0) (*78*) with the annotation (.bed) file. The normalization and DEG analysis for the data were carried out using edgeR, as mentioned previously (*79*). DEGs were determined on the basis of the cutoff: absolute fold change ≥ 1.5 and FDR ≤ 0.05.

For overlap analysis of DEGs with the processed data of other studies, the significance of gene number overlap was determined by Fisher's exact test on a two-by-two contingency table. The universal set of the genes was calculated on the basis of the intersection of total genes analyzed in the studies with our study. If this information was not available, then we took 3975 genes as the universal set (table S2).

Bacterial stress survival assay

Exponentially growing *Mtb*, *Mtb*Δ*iscS*, and *iscS-comp* (OD_{600} ~ 0.6) cultures were diluted to an OD_{600} of ~0.15 and exposed to 80 μM CHP, 60 μM Mnd (Sigma-Aldrich, St. Louis, MO), 1 mM DETA-NO (Cayman Chemical, USA) and incubated at 37°C in a shaker incubator. After 4 and 24 hours of treatment, cells were serially diluted and plated on 7H11-ADS plates. Colonies were enumerated after an incubation of 3 to 5 weeks at 37°C.

Macrophage preparation and *Mtb* infection

RAW264.7 murine macrophage cell line was used for the ex vivo infection study. This cell line was acquired from the American Type Culture Collection (Manassas, VA) and tested negative for mycoplasma contamination using the DE-MycoX Mycoplasma PCR Detection Kit (CELLclone, catalog no. GX-E-250). *Mtb* infection was performed in either naïve or activated macrophages. Macrophage activation was achieved by treating RAW264.7 cells with interferon-γ (IFN-γ) (30 ng/ml; PeproTech, catalog no. 315-05) and *E. coli* lipopolysaccharide (LPS) (10 ng/ml; Sigma-Aldrich, catalog no. L2630) for 16 hours. These activated macrophages were separately treated with a specific inhibitor of iNOS, 1400W dihydrochloride (25 μM) (Sigma-Aldrich, catalog no. W4262). Macrophage cells were infected with *Mtb*, *Mtb*Δ*iscS*, and *iscS-comp* at an MOI of 1:2 for 4 hours, followed by washing thoroughly with warm PBS (137 mM NaCl + 2.7 mM KCl + 10 mM Na_2HPO_4 + 1.4 mM KH_2PO_4) and Dulbecco′s modified Eagle′s medium (DMEM; CELLclone) to remove all extracellular bacteria and finally added fresh media [DMEM + 10% fetal bovine serum (MP Biomedicals, catalog no. 092916754)] with or without IFN-γ and incubated at 37°C with 5% CO_2. To determine bacterial survival after infection at different time points, infected cells were lysed in 0.06% SDS in PBS. Lysates were serially diluted and plated on 7H11-OADC agar plates. Plates were incubated at 37°C until colonies appeared for CFU enumeration.

Determination of MIC and antibiotic susceptibility assay

MIC was evaluated by a MABA in a 96-well plate format (*58*). Exponentially growing *Mtb* strains (OD_{600} ~ 0.6) were harvested to prepare 1×10^6 cells/ml density culture. Approximately 1×10^5 bacteria were added per well in a total volume of 200 μl of 7H9 + ADS medium containing a gradient of drug concentrations. Controls for the assay consisted of wells lacking *Mtb* for a media background and wells devoid of a drug for maximum bacterial growth. Following an incubation period of 5 days at 37°C, 30 μl of 0.02% resazurin (Sigma-Aldrich, catalog no. R7017) was added, and plates were incubated for another 24 hours at 37°C. Fluorescence intensity was detected using a SpectraMax M3 plate reader (Molecular Devices, San Jose, CA) in a bottom-reading mode with excitation at 530 nm and emission at 590 nm. Percent inhibition for respective antibiotics was derived from the relative fluorescence values compared to the untreated control. MIC was considered the minimum antibiotic concentration that yielded at least 90% reduction in fluorescence compared to the untreated growth control. Antibiotic concentration ranges were as follows: Bdq (1.8 to 0.005 μM), Mox (1 to 0.003 μM), Rif (1.13 to 0.003 μM), and Inh (7.3 to 0.021 μM).

Antibiotic kill kinetic assay

Exponentially growing cultures of *Mtb* strains were brought to a density of 1×10^6 CFU/ml and incubated with or without 1× MIC_{90} (for *Mtb*) of antibiotics: Mox, Rif, and Inh in 10-ml cultures for a period of 10 days in a shaker incubator at 37°C. The survival kinetics of the bacteria was monitored by plating for viable cells on days 0, 1, 3, 5, 7, and 10 after treatments. Following incubation at 37°C for 3 to 5 weeks, viable colonies were enumerated.

In vivo infection experiments

For the mice infection model, 5- to 6-week-old female BALB/c mice (n = 5 per group) were infected via an aerosol route with approximately 100 bacilli per mouse with *Mtb*, *Mtb*Δ*iscS*, and *iscS-comp* strains using a Madison chamber by aerosol generation. At indicated times after infection, mice were sacrificed, and the lungs and spleens were harvested for determination of bacillary load and tissue histopathology analysis as described (*14*). The bacillary load was quantified by plating serial dilutions of tissue homogenates on 7H11-OADC agar plates supplemented with lyophilized BBL MGIT PANTA antibiotic cocktail (polymyxin B, amphotericin B, nalidixic acid, trimethoprim, and azlocillin; as supplied by BD Biosciences, USA). Colonies were enumerated after 4 weeks of incubation at 37°C. Pathological analyses were represented as granuloma scores as described previously (*14*).

Mice infection experiment with the SufS-KD strains was performed similarly, where mice were divided into six groups, *Mtb-sufS* KD − Dox (without doxycycline), *Mtb-sufS* KD + Dox acute phase (doxycycline started after 7 days of infection), *Mtb-sufS* KD + Dox chronic phase (doxycycline started after 21 days of infection), Δ*iscS-sufS* KD − Dox (without doxycycline), Δ*iscS-sufS* KD + Dox acute phase (doxycycline started after 7 days of infection), and Δ*iscS-sufS* KD − Dox chronic phase (doxycycline started at 21 days after infection). Doxycycline (1 mg/ml) was given in drinking water with a 5% sucrose solution. Water feeders were light-protected and replaced twice a week (*11*).

To determine the role of NO in *Mtb* infection and pathogenesis, 5- to 7-week-old female $iNOS^{-/-}$ mice (n = 6) were infected with approximately 100 bacilli per mouse with *Mtb* and *Mtb*Δ*iscS* strains using a Madison chamber by aerosol generation. Mice were humanely sacrificed, and the lungs were harvested for determination of bacillary load. The bacillary load was quantified by plating serial dilutions of tissue homogenates as described above. All mice for the above experiments were obtained from the institute Central Animal Facility (CAF).

Generation of conditional knockdowns using CRISPRi strategy

Construction of SufS-KD strains was carried out using the CRISPRi technology as described in (*54*). Briefly, an inactive form of *Streptococcus pyogenes Cas9* enzyme harboring mutations D10A and H820A (*dCas9*) resulting in nuclease inactivity offers the ability to control targeted gene expression transiently or stably without altering the genomic sequence. dCas9 was expressed in the integrative plasmid system pRH2502 from a TetR-regulated uvtetO promoter. *sufS* was targeted by expressing a gene-specific sgRNA in the episomal vector pRH2521 under the control of a TetR-regulated smyc promoter (Pmyc1*tetO*). For *sufS* depletion, sgRNAs were designed for the region 52 to 75 bp of the *sufS* ORF and cloned in pRH2521. Both the plasmids pRH2502-*dCas9* and pRH2521-sgRNA were sequentially electroporated into *Mtb* and *Mtb*Δ*iscS* strains, followed by the selection of positive clones on KAN + HYG plates. The $SufS^{-}$ KD was achieved by culturing the KD

strains in 7H9 media and treating them with ATc (200 ng/ml) when OD_{600} reached 0.1 to 0.2, with the addition of ATc every 48 hours. Levels of *sufS* depletion were verified by RT-qPCR after 48 hours of ATc treatment.

RT-qPCR analysis

Total bacterial RNA was extracted using the FastRNA Pro Blue Kit (MP Biomedicals, Santa Ana, CA) and further purified using RNeasy spin columns (Qiagen, USA) in accordance with the manufacturer's instructions. For qRT-PCR analysis under different experiment setups, total RNA was extracted at indicated time points, followed by treatment with deoxyribonuclease (DNase). Approximately 600 ng of DNase-treated RNA was used for cDNA synthesis using random hexamer oligonucleotide primers (iScript Select cDNA Synthesis Kit, Bio-Rad, USA). Gene-specific primers and iQ SYBR Green Supermix (Bio-Rad, USA) were used for qRT-PCR (StepOne Plus, Thermo Fisher Scientific, USA). For gene expression analysis, 16*S* rRNA levels were used as internal normalization control in all cases. A list of primers used for qRT-PCR is given in table S4.

RT-qPCR on RNA of *Mtb* derived from mouse lungs and infected macrophages

Bacterial RNA was extracted from infected mouse lungs as described in (*80*), with slight modification. Briefly, lung tissues were dissociated in a buffer containing Liberase TM (0.2 mg/ml; Roche, Basel, Switzerland), DNase I (0.1 mg/ml; Roche, Basel, Switzerland), and 5 mM $MgCl_2$ for 1 hour at 37°C at 180 rpm. Cells were spun down at 5000 rpm for 15 min, and the pellet was resuspended in 1× red blood cell lysis buffer and incubated at room temperature for 10 min with intermittent mixing. Samples were centrifuged at 5000 rpm for 5 min, and the pellet was resuspended in 1 ml of RNA Pro solution (FastRNA Pro Blue Kit) to lyse most of the mammalian cells. Samples were centrifuged at 12,000*g* for 15 min at 4°C, the supernatant was carefully removed, and the pellet was resuspended again in 1 ml of RNA Pro solution and lysed by bead beating followed by chloroform-isopropanol–based isolation of RNA. The total RNA isolated was quantified, and quality was checked spectrophotometrically using NanoDrop. RNA was treated with DNase (Turbo DNase, RiboPure-Blood kit, Invitrogen), followed by first-strand cDNA synthesis using Maxima H minus RT enzyme mix (Thermo Fisher Scientific) using gene-specific primers for 16*S* rRNA and *sufS* (table S4). The cDNA obtained is amplified using Taq DNA polymerase (NEB) with gene-specific primer pairs. Last, real-time qPCR of the amplified cDNA is performed using iQ SYBR Green Supermix. For gene expression analysis, 16*S* rRNA levels were used as internal normalization control in all cases.

Bacterial RNA was isolated from infected RAW264.7 murine macrophages after 48 hours of infection as described in (*14*). Briefly, infected macrophages were harvested and treated with 5 M GTC buffer for differential lysis of only macrophages. The samples were centrifuged at 13,000 rpm for 20 min to separate the bacterial pellet. The bacterial pellet was resuspended in 1 ml of RNA Pro solution (FastRNA Pro Blue Kit) and lysed by bead beating. Total RNA isolation, cDNA synthesis, and PCR steps were followed as mentioned above. A list of primers used is given in table S4.

Statistical analysis

All data were graphed and analyzed with Prism v9.0 (GraphPad Software, San Diego, CA) unless otherwise stated. Representative data of at least three independent biological replicates are indicated as means ± SEM. Statistical significance was determined with two-tailed unpaired *t* test or with one-way or two-way analysis of variance (ANOVA) for comparison of multiple groups. All *P* values are given in each figure legend.

Ethics statement

This study was carried out strictly following the guidelines provided by the Committee for the Purpose of Control and Supervision on Experiments on Animals (CPCSEA), Government of India. The protocol for the animal experiment was approved by the animal ethical committee on the Ethics of Animal Experiments, Indian Institute of Science (IISc), Bangalore, India (approval number: CAF/Ethics/544/2017). All humane efforts were made to minimize the suffering.

Supplementary Materials

This PDF file includes:
Figs. S1 to S16
Legends for tables S1 to S4

Other Supplementary Material for this manuscript includes the following:
Tables S1 to S4

REFERENCES AND NOTES

1. S. Ehrt, D. Schnappinger, Mycobacterial survival strategies in the phagosome: Defence against host stresses. *Cell. Microbiol.* **11**, 1170–1178 (2009).
2. F. C. Fang, Antimicrobial reactive oxygen and nitrogen species: Concepts and controversies. *Nat. Rev. Microbiol.* **2**, 820–832 (2004).
3. H. K. Miller, V. Auerbuch, Bacterial iron-sulfur cluster sensors in mammalian pathogens. *Metallomics* **7**, 943–956 (2015).
4. V. Saini, A. Farhana, J. N. Glasgow, A. J. Steyn, Iron sulfur cluster proteins and microbial regulation: Implications for understanding tuberculosis. *Curr. Opin. Chem. Biol.* **16**, 45–53 (2012).
5. I. Elchennawi, S. Ollagnier de Choudens, Iron–Sulfur Clusters toward Stresses: Implication for Understanding and Fighting Tuberculosis. *Inorganics* **10**, 174 (2022).
6. S. Jang, J. A. Imlay, Hydrogen peroxide inactivates the *Escherichia coli* Isc iron-sulphur assembly system, and OxyR induces the Suf system to compensate. *Mol. Microbiol.* **78**, 1448–1467 (2010).
7. M. A. DeJesus, E. R. Gerrick, W. Xu, S. W. Park, J. E. Long, C. C. Boutte, E. J. Rubin, D. Schnappinger, S. Ehrt, S. M. Fortune, C. M. Sassetti, T. R. Ioerger, C. Manoil, D. Lampe, Comprehensive essentiality analysis of the *Mycobacterium tuberculosis* genome via saturating transposon mutagenesis. *mBio* **8**, (2017).
8. G. Huet, M. Daffe, I. Saves, Identification of the *Mycobacterium tuberculosis* SUF machinery as the exclusive mycobacterial system of [Fe-S] cluster assembly: Evidence for its implication in the pathogen's survival. *J. Bacteriol.* **187**, 6137–6146 (2005).
9. M. I. Voskuil, I. L. Bartek, K. Visconti, G. K. Schoolnik, The response of *Mycobacterium tuberculosis* to reactive oxygen and nitrogen species. *Front. Microbiol.* **2**, 105 (2011).
10. K. Anand, A. Tripathi, K. Shukla, N. Malhotra, A. K. Jamithireddy, R. K. Jha, S. N. Chaudhury, R. S. Rajmani, A. Ramesh, V. Nagaraja, B. Gopal, G. Nagaraju, A. S. Narain Seshayee, A. Singh, *Mycobacterium tuberculosis* SufR responds to nitric oxide via its 4Fe-4S cluster and regulates Fe-S cluster biogenesis for persistence in mice. *Redox Biol.* **46**, 102062 (2021).
11. A. Tripathi, K. Anand, M. das, R. A. O'Niel, S. P. S, C. Thakur, R. R. R. L., R. S. Rajmani, N. Chandra, S. Laxman, A. Singh, *Mycobacterium tuberculosis* requires SufT for Fe-S cluster maturation, metabolism, and survival in vivo. *PLOS Pathog.* **18**, e1010475 (2022).
12. M. Kumar, F. G. Khan, S. Sharma, R. Kumar, J. Faujdar, R. Sharma, D. S. Chauhan, R. Singh, S. K. Magotra, I. A. Khan, Identification of *Mycobacterium tuberculosis* genes preferentially expressed during human infection. *Microb. Pathog.* **50**, 31–38 (2011).

13. K. Kurthkoti, H. Amin, M. J. Marakalala, S. Ghanny, S. Subbian, A. Sakatos, J. Livny, S. M. Fortune, M. Berney, G. M. Rodriguez, The capacity of *Mycobacterium tuberculosis* to survive iron starvation might enable it to persist in iron-deprived microenvironments of human granulomas. *MBio* **8**, (2017).
14. R. Mishra, S. Kohli, N. Malhotra, P. Bandyopadhyay, M. Mehta, M. H. Munshi, V. Adiga, V. K. Ahuja, R. K. Shandil, R. S. Rajmani, A. S. N. Seshasayee, A. Singh, Targeting redox heterogeneity to counteract drug tolerance in replicating *Mycobacterium tuberculosis*. *Sci. Transl. Med.* **11**, (2019).
15. S. Mishra, P. Shukla, A. Bhaskar, K. Anand, P. Baloni, R. K. Jha, A. Mohan, R. S. Rajmani, V. Nagaraja, N. Chandra, A. Singh, Efficacy of β-lactam/β-lactamase inhibitor combination is linked to WhiB4-mediated changes in redox physiology of *Mycobacterium tuberculosis*. *eLife* **6**, (2017).
16. D. Schnappinger, S. Ehrt, M. I. Voskuil, Y. Liu, J. A. Mangan, I. M. Monahan, G. Dolganov, B. Efron, P. D. Butcher, C. Nathan, G. K. Schoolnik, Transcriptional adaptation of mycobacterium tuberculosis within macrophages: Insights into the phagosomal environment. *J. Exp. Med.* **198**, 693–704 (2003).
17. J. Rybniker, F. Pojer, J. Marienhagen, G. S. Kolly, J. M. Chen, E. van Gumpel, P. Hartmann, S. T. Cole, The cysteine desulfurase IscS of *Mycobacterium tuberculosis* is involved in iron-sulfur cluster biogenesis and oxidative stress defence. *Biochem. J.* **459**, 467–478 (2014).
18. A. Singh, L. Guidry, K. V. Narasimhulu, D. Mai, J. Trombley, K. E. Redding, G. I. Giles, J. R. Lancaster Jr., A. J. C. Steyn, *Mycobacterium tuberculosis* WhiB3 responds to O2 and nitric oxide via its [4Fe-4S] cluster and is essential for nutrient starvation survival. *Proc. Natl. Acad. Sci. U.S.A.* **104**, 11562–11567 (2007).
19. O. Djaman, F. W. Outten, J. A. Imlay, Repair of oxidized iron-sulfur clusters in *Escherichia coli*. *J. Biol. Chem.* **279**, 44590–44599 (2004).
20. T. G. Dong, S. Dong, C. Catalano, R. Moore, X. Liang, J. J. Mekalanos, Generation of reactive oxygen species by lethal attacks from competing microbes. *Proc. Natl. Acad. Sci. U.S.A.* **112**, 2181–2186 (2015).
21. E. L. Mettert, P. J. Kiley, Fe-S proteins that regulate gene expression. *Biochim. Biophys. Acta* **1853**, 1284–1293 (2015).
22. A. Bhaskar, M. Chawla, M. Mehta, P. Parikh, P. Chandra, D. Bhave, D. Kumar, K. S. Carroll, A. Singh, Reengineering redox sensitive GFP to measure mycothiol redox potential of *Mycobacterium tuberculosis* during infection. *PLOS Pathog.* **10**, e1003902 (2014).
23. E. L. MacKenzie, K. Iwasaki, Y. Tsuji, Intracellular iron transport and storage: From molecular mechanisms to health implications. *Antioxid. Redox Signal.* **10**, 997–1030 (2008).
24. A. Latifi, R. Jeanjean, S. Lemeille, M. Havaux, C. C. Zhang, Iron starvation leads to oxidative stress in *Anabaena* sp. strain PCC 7120. *J. Bacteriol.* **187**, 6596–6598 (2005).
25. L. Leaden, L. G. Silva, R. A. Ribeiro, N. M. dos Santos, A. P. R. Lorenzetti, T. G. P. Alegria, M. L. Schulz, M. H. G. Medeiros, T. Koide, M. V. Marques, Iron deficiency generates oxidative stress and activation of the SOS response in *Caulobacter crescentus*. *Front. Microbiol.* **9**, 2014 (2018).
26. J. A. Imlay, Where in the world do bacteria experience oxidative stress? *Environ. Microbiol.* **21**, 521–530 (2019).
27. C. D. Sohaskey, M. I. Voskuil, In vitro models that utilize hypoxia to induce non-replicating persistence in mycobacteria. *Methods Mol. Biol.* **1285**, 201–213 (2015).
28. B. Tizzano, T. K. Dallenga, C. Utpatel, J. Behrends, S. Homolka, T. A. Kohl, S. Niemann, Survival of hypoxia-induced dormancy is not a common feature of all strains of the *Mycobacterium tuberculosis* complex. *Sci. Rep.* **11**, 2628 (2021).
29. A. V. Kareyeva, V. G. Grivennikova, A. D. Vinogradov, Mitochondrial hydrogen peroxide production as determined by the pyridine nucleotide pool and its redox state. *Biochim. Biophys. Acta* **1817**, 1879–1885 (2012).
30. A. D. Vinogradov, V. G. Grivennikova, Oxidation of NADH and ROS production by respiratory complex I. *Biochim. Biophys. Acta* **1857**, 863–871 (2016).
31. T. L. Clanton, Hypoxia-induced reactive oxygen species formation in skeletal muscle. *J. Appl. Physiol.* **102**, 2379–2388 (2007).
32. J. Duranteau, N. S. Chandel, A. Kulisz, Z. Shao, P. T. Schumacker, Intracellular signaling by reactive oxygen species during hypoxia in cardiomyocytes. *J. Biol. Chem.* **273**, 11619–11624 (1998).
33. B. Py, F. Barras, Building Fe-S proteins: Bacterial strategies. *Nat. Rev. Microbiol.* **8**, 436–446 (2010).
34. M. Hillion, J. Bernhardt, T. Busche, M. Rossius, S. Maaß, D. Becher, M. Rawat, M. Wirtz, R. Hell, C. Rückert, J. Kalinowski, H. Antelmann, Monitoring global protein thiol-oxidation and protein S-mycothiolation in *Mycobacterium smegmatis* under hypochlorite stress. *Sci. Rep.* **7**, 1195 (2017).
35. M. Rawat, Y. Av-Gay, Mycothiol-dependent proteins in actinomycetes. *FEMS Microbiol. Rev.* **31**, 278–292 (2007).
36. M. R. Hasan, M. Rahman, S. Jaques, E. Purwantini, L. Daniels, Glucose 6-phosphate accumulation in mycobacteria: Implications for a novel F420-dependent anti-oxidant defense system. *J. Biol. Chem.* **285**, 19135–19144 (2010).
37. A. Stincone, A. Prigione, T. Cramer, M. M. C. Wamelink, K. Campbell, E. Cheung, V. Olin-Sandoval, N. M. Grüning, A. Krüger, M. Tauqeer Alam, M. A. Keller, M. Breitenbach, K. M. Brindle, J. D. Rabinowitz, M. Ralser, The return of metabolism: Biochemistry and physiology of the pentose phosphate pathway. *Biol. Rev. Camb. Philos. Soc.* **90**, 927–963 (2015).
38. G. L. Newton, N. Buchmeier, R. C. Fahey, Biosynthesis and functions of mycothiol, the unique protective thiol of actinobacteria. *Microbiol. Mol. Biol. Rev.* **72**, 471–494 (2008).
39. S. Watanabe, M. Zimmermann, M. B. Goodwin, U. Sauer, C. E. Barry, H. I. Boshoff, Fumarate reductase activity maintains an energized membrane in anaerobic *Mycobacterium tuberculosis*. *PLOS Pathog.* **7**, e1002287 (2011).
40. P. Bandyopadhyay, I. Pramanick, R. Biswas, S. PS, S. Sreedharan, S. Singh, R. S. Rajmani, S. Laxman, S. Dutta, A. Singh, *S*-Adenosylmethionine-responsive cystathionine β-synthase modulates sulfur metabolism and redox balance in *Mycobacterium tuberculosis*. *Sci. Adv.* **8**, eabo0097 (2022).
41. P. R. Wheeler, N. G. Coldham, L. Keating, S. V. Gordon, E. E. Wooff, T. Parish, R. G. Hewinson, Functional demonstration of reverse transsulfuration in the *Mycobacterium tuberculosis* complex reveals that methionine is the preferred sulfur source for pathogenic mycobacteria. *J. Biol. Chem.* **280**, 8069–8078 (2005).
42. S. D. Yelamanchi, A. Surolia, Targeting amino acid metabolism of *Mycobacterium tuberculosis* for developing inhibitors to curtail its survival. *IUBMB Life* **73**, 643–658 (2021).
43. V. Saini, B. M. Cumming, L. Guidry, D. A. Lamprecht, J. H. Adamson, V. P. Reddy, K. C. Chinta, J. H. Mazorodze, J. N. Glasgow, M. Richard-Greenblatt, A. Gomez-Velasco, H. Bach, Y. Av-Gay, H. Eoh, K. Rhee, A. J. C. Steyn, Ergothioneine maintains redox and bioenergetic homeostasis essential for drug susceptibility and virulence of *Mycobacterium tuberculosis*. *Cell Rep.* **14**, 572–585 (2016).
44. D. A. Lamprecht, P. M. Finin, M. A. Rahman, B. M. Cumming, S. L. Russell, S. R. Jonnala, J. H. Adamson, A. J. C. Steyn, Turning the respiratory flexibility of *Mycobacterium tuberculosis* against itself. *Nat. Commun.* **7**, 12393 (2016).
45. B. M. Cumming, M. A. Rahman, D. A. Lamprecht, K. H. Rohde, V. Saini, J. H. Adamson, D. G. Russell, A. J. C. Steyn, *Mycobacterium tuberculosis* arrests host cycle at the G_1-S transition to establish long term infection. *PLOS Pathog.* **13**, e1006389 (2017).
46. M. A. Kohanski, D. J. Dwyer, B. Hayete, C. A. Lawrence, J. J. Collins, A common mechanism of cellular death induced by bactericidal antibiotics. *Cell* **130**, 797–810 (2007).
47. B. Ezraty, A. Vergnes, M. Banzhaf, Y. Duverger, A. Huguenot, A. R. Brochado, S. Y. Su, L. Espinosa, L. Loiseau, B. Py, A. Typas, F. Barras, Fe-S cluster biosynthesis controls uptake of aminoglycosides in a ROS-less death pathway. *Science* **340**, 1583–1587 (2013).
48. C. Vilcheze, Coresistance to isoniazid and ethionamide maps to mycothiol biosynthetic genes in *Mycobacterium bovis*. *Antimicrob. Agents Chemother.* **55**, 4422–4423 (2011).
49. E. S. Boyd, K. M. Thomas, Y. Dai, J. M. Boyd, F. W. Outten, Interplay between oxygen and Fe-S cluster biogenesis: Insights from the Suf pathway. *Biochemistry* **53**, 5834–5847 (2014).
50. M. Buhning, A. Valleriani, S. Leimkuhler, The role of SufS is restricted to Fe-S cluster biosynthesis in *Escherichia coli*. *Biochemistry* **56**, 1987–2000 (2017).
51. U. Tokumoto, S. Kitamura, K. Fukuyama, Y. Takahashi, Interchangeability and distinct properties of bacterial Fe-S cluster assembly systems: Functional replacement of the isc and suf operons in *Escherichia coli* with the nifSU-like operon from *Helicobacter pylori*. *J. Biochem.* **136**, 199–209 (2004).
52. J. Braverman, S. A. Stanley, Nitric oxide modulates macrophage responses to *Mycobacterium tuberculosis* infection through activation of HIF-1α and repression of NF-κB. *J. Immunol.* **199**, 1805–1816 (2017).
53. J. D. MacMicking, R. J. North, R. LaCourse, J. S. Mudgett, S. K. Shah, C. F. Nathan, Identification of nitric oxide synthase as a protective locus against tuberculosis. *Proc. Natl. Acad. Sci. U.S.A.* **94**, 5243–5248 (1997).
54. A. K. Singh, X. Carette, L. P. Potluri, J. D. Sharp, R. Xu, S. Prisic, R. N. Husson, Investigating essential gene function in *Mycobacterium tuberculosis* using an efficient CRISPR interference system. *Nucleic Acids Res.* **44**, e143 (2016).
55. C. M. Sassetti, D. H. Boyd, E. J. Rubin, Genes required for mycobacterial growth defined by high density mutagenesis. *Mol. Microbiol.* **48**, 77–84 (2003).
56. Y. Minato, D. M. Gohl, J. M. Thiede, J. M. Chacón, W. R. Harcombe, F. Maruyama, A. D. Baughn, Genomewide assessment of *Mycobacterium tuberculosis* conditionally essential metabolic pathways. *mSystems* **4**, e00070-19 (2019).
57. M. Das, A. Dewan, S. Shee, A. Singh, The multifaceted bacterial cysteine desulfurases: From metabolism to pathogenesis. *Antioxidants (Basel)* **10**, (2021).
58. S. Shee, S. Singh, A. Tripathi, C. Thakur, A. Kumar T, M. Das, V. Yadav, S. Kohli, R. S. Rajmani, N. Chandra, H. Chakrapani, K. Drlica, A. Singh, Moxifloxacin-mediated killing of *Mycobacterium tuberculosis* involves respiratory downshift, reductive stress, and accumulation of reactive oxygen species. *Antimicrob. Agents Chemother.* **66**, e0059222 (2022).
59. T. Bertrand, N. A. J. Eady, J. N. Jones, Jesmin, J. M. Nagy, B. Jamart-Grégoire, E. L. Raven, K. A. Brown, Crystal structure of *Mycobacterium tuberculosis* catalase-peroxidase. *J. Biol. Chem.* **279**, 38991–38999 (2004).

60. J. B. Cooper, K. McIntyre, M. O. Badasso, S. P. Wood, Y. Zhang, T. R. Garbe, D. Young, X-ray structure analysis of the iron-dependent superoxide dismutase from *Mycobacterium tuberculosis* at 2.0 angstroms resolution reveals novel dimer-dimer interactions. *J. Mol. Biol.* **246**, 531–544 (1995).
61. T. R. Figueira, M. H. Barros, A. A. Camargo, R. F. Castilho, J. C. B. Ferreira, A. J. Kowaltowski, F. E. Sluse, N. C. Souza-Pinto, A. E. Vercesi, Mitochondria as a source of reactive oxygen and nitrogen species: From molecular mechanisms to human health. *Antioxid. Redox Signal.* **18**, 2029–2074 (2013).
62. N. Ruecker, R. Jansen, C. Trujillo, S. Puckett, P. Jayachandran, G. G. Piroli, N. Frizzell, H. Molina, K. Y. Rhee, S. Ehrt, Fumarase deficiency causes protein and metabolite succination and intoxicates *Mycobacterium tuberculosis*. *Cell Chem. Biol.* **24**, 306–315 (2017).
63. P. A. Tyrakis, M. E. Yurkovich, M. Sciacovelli, E. K. Papachristou, H. R. Bridges, E. Gaude, A. Schreiner, C. D'Santos, J. Hirst, J. Hernandez-Fernaud, R. Springett, J. R. Griffiths, C. Frezza, Fumarate hydratase loss causes combined respiratory chain defects. *Cell Rep.* **21**, 1036–1047 (2017).
64. R. Kambampati, C. T. Lauhon, MnmA and IscS are required for in vitro 2-thiouridine biosynthesis in *Escherichia coli*. *Biochemistry* **42**, 1109–1117 (2003).
65. T. R. Rustad, M. I. Harrell, R. Liao, D. R. Sherman, The enduring hypoxic response of *Mycobacterium tuberculosis*. *PLOS ONE* **3**, e1502 (2008).
66. C. Prolo, M. N. Alvarez, R. Radi, Peroxynitrite, a potent macrophage-derived oxidizing cytotoxin to combat invading pathogens. *Biofactors* **40**, 215–225 (2014).
67. A. Averyanov, Oxidative burst and plant disease resistance. *Front. Biosci. (Elite Ed.)* **1**, 142–152 (2009).
68. J. M. Robinson, Phagocytic leukocytes and reactive oxygen species. *Histochem. Cell Biol.* **131**, 465–469 (2009).
69. L. E. Via, P. L. Lin, S. M. Ray, J. Carrillo, S. S. Allen, S. Y. Eum, K. Taylor, E. Klein, U. Manjunatha, J. Gonzales, E. G. Lee, S. K. Park, J. A. Raleigh, S. N. Cho, D. N. McMurray, J. A. L. Flynn, C. E. Barry III, Tuberculous granulomas are hypoxic in guinea pigs, rabbits, and nonhuman primates. *Infect. Immun.* **76**, 2333–2340 (2008).
70. T. M. Jeitner, Optimized ferrozine-based assay for dissolved iron. *Anal. Biochem.* **454**, 36–37 (2014).
71. C. Vilcheze, Enhanced respiration prevents drug tolerance and drug resistance in *Mycobacterium tuberculosis*. *Proc. Natl. Acad. Sci. U.S.A.* **114**, 4495–4500 (2017).
72. N. K. Taneja, J. S. Tyagi, Resazurin reduction assays for screening of anti-tubercular compounds against dormant and actively growing *Mycobacterium tuberculosis*, *Mycobacterium bovis* BCG and *Mycobacterium smegmatis*. *J. Antimicrob. Chemother.* **60**, 288–293 (2007).
73. A. Walvekar, Z. Rashida, H. Maddali, S. Laxman, A versatile LC-MS/MS approach for comprehensive, quantitative analysis of central metabolic pathways. *Wellcome Open Res.* **3**, 122 (2018).
74. M. Chawla, P. Parikh, A. Saxena, M. H. Munshi, M. Mehta, D. Mai, A. K. Srivastava, K. V. Narasimhulu, K. E. Redding, N. Vashi, D. Kumar, A. J. C. Steyn, A. Singh, *Mycobacterium tuberculosis* WhiB4 regulates oxidative stress response to modulate survival and dissemination in vivo. *Mol. Microbiol.* **85**, 1148–1165 (2012).
75. A. Singh, D. K. Crossman, D. Mai, L. Guidry, M. I. Voskuil, M. B. Renfrow, A. J. C. Steyn, *Mycobacterium tuberculosis* WhiB3 maintains redox homeostasis by regulating virulence lipid anabolism to modulate macrophage response. *PLOS Pathog.* **5**, e1000545 (2009).
76. H. Li, R. Durbin, Fast and accurate short read alignment with Burrows-Wheeler transform. *Bioinformatics* **25**, 1754–1760 (2009).
77. H. Li, B. Handsaker, A. Wysoker, T. Fennell, J. Ruan, N. Homer, G. Marth, G. Abecasis, R. Durbin; 1000 Genome Project Data Processing Subgroup, The sequence alignment/map format and SAMtools. *Bioinformatics* **25**, 2078–2079 (2009).
78. A. R. Quinlan, I. M. Hall, BEDTools: A flexible suite of utilities for comparing genomic features. *Bioinformatics* **26**, 841–842 (2010).
79. M. D. Robinson, D. J. McCarthy, G. K. Smyth, edgeR: A Bioconductor package for differential expression analysis of digital gene expression data. *Bioinformatics* **26**, 139–140 (2010).
80. D. Pisu, L. Huang, J. K. Grenier, D. G. Russell, Dual RNA-Seq of MTB-Infected macrophages in vivo reveals ontologically distinct host-pathogen interactions. *Cell Rep.* **30**, 335–350. e4 (2020).

Acknowledgments: We thank K. Drlica for providing critical comments on the manuscript. We are thankful to A. Pandit and Next Generation Genomics Facility (NGGF) at the National Centre for Biological Sciences (NCBS), Bangalore for conducting the RNA-seq experiment. We acknowledge the biosafety level 3 (BSL-3) facilities at CIDR, IISc, Bangalore. **Funding:** This work was supported by Wellcome Trust Department of Biotechnology (DBT) India Alliance grant IA/S/16/2/502700 (to A.S.) and in part by DBT grant BT/PR29098/Med/29/1324/2018 (to A.S.), DST-SERB grants SPR/2021/000175 and SERB/CRG/2022/002009 (to A.S.), UGC-DAE Consortium for Scientific Research, University Grants Commission UGC special Assistance (to A.S.), Crypto Relief grant ODAA/INT/20-21 (to A.S.), Ignite Life Science Foundation SP/ILSF-22-0001 (to A.S.), Department of Atomic Energy (DAE) 12-R&D-TFR-5.04-0800 (to A.S.N.S.), and the Revati and Satya Nadham Atturi Chair Professorship (to A.S.). M.D. was supported by GATE Ph.D fellowship from IISc. The funders had no role in study design, data collection and analysis, or preparation of the manuscript. **Author contributions:** Conceptualization: M.D. and A.S. Methodology: M.D., S. Sh., S.Sr., N.M., M.N., U.B., S.K., and R.S.R. Bioinformatic analysis: N.M., M.N., U.B., N.C., and A.S.N.S. Investigation: M.D., S.Sh., S.Sr., N.M., M.N., U.B., S.K., and R.S.R. Supervision: M.D. and A.S. Data analysis: M.D., S.Sh., N.M., N.C., A.S.N.S., S.L., and A.S. Writing—original draft: M.D. and A.S. Writing—review and editing: M.D. and A.S. All authors read and approved the final manuscript. **Competing interests:** The authors declare that they have no competing interests. **Data and materials availability:** All data needed to evaluate the conclusions in the paper are present in the paper and/or the Supplementary Materials. All the strains and plasmids generated for this study are available from the corresponding author upon reasonable request. The RNA-seq datasets have been submitted in Gene Expression Omnibus (GEO) *MtbΔiscS* (GSE224043) and *Mtb whiB1* KD (GSE224027).

Submitted 22 February 2023
Accepted 10 November 2023
Published 13 December 2023
10.1126/sciadv.adh2858

Published in final edited form as:
Sci Transl Med. 2019 November 13; 11(518): . doi:10.1126/scitranslmed.aaw6635.

Targeting redox heterogeneity to counteract drug tolerance in replicating *Mycobacterium tuberculosis*

Richa Mishra[1,2], **Sakshi Kohli**[1,2], **Nitish Malhotra**[3], **Parijat Bandyopadhyay**[1,2], **Mansi Mehta**[1,2], **MohamedHusen Munshi**[1,2], **Vasista Adiga**[2], **Vijay Kamal Ahuja**[4], **Radha K. Shandil**[4], **Raju S. Rajmani**[2], **Aswin Sai Narain Seshasayee**[3], **Amit Singh**[1,*]

[1]Department of Microbiology and Cell Biology, Indian Institute of Science, Bangalore 560012, India

[2]Centre for Infectious Disease Research, Indian Institute of Science, Bangalore 560012, India

[3]National Centre for Biological Sciences (NCBS), Tata Institute of Fundamental Research (TIFR), Bangalore 560065, India

[4]Foundation for Neglected Disease Research, Bangalore 560065, India

Abstract

The capacity of *Mycobacterium tuberculosis* (*Mtb*) to tolerate multiple antibiotics represents a major problem in tuberculosis (TB) management. Heterogeneity in *Mtb* populations is one of the factors that drives antibiotic tolerance during infection. However, the mechanisms underpinning this variation in bacterial population remain poorly understood. Here, we show that phagosomal acidification alters the redox physiology of *Mtb* to generate a population of replicating bacteria that display drug tolerance during infection. RNA sequencing of this redox-altered population revealed the involvement of iron-sulfur (Fe-S) cluster biogenesis, hydrogen sulfide (H_2S) gas, and drug efflux pumps in antibiotic tolerance. The fraction of the pH- and redox-dependent tolerant population increased when *Mtb* infected macrophages with actively replicating HIV-1, suggesting that redox heterogeneity could contribute to high rates of TB therapy failure during HIV-TB coinfection. Pharmacological inhibition of phagosomal acidification by the antimalarial drug chloroquine (CQ) eradicated drug-tolerant *Mtb*, ameliorated lung pathology, and reduced postchemotherapeutic relapse in in vivo models. The pharmacological profile of CQ (C_{max} and AUC_{last}) exhibited no major drug-drug interaction when coadministered with first line anti-TB drugs in mice. Our data establish a link between phagosomal pH, redox metabolism, and drug

*Corresponding author. asingh@iisc.ac.in.

Author contributions: R.M. and A.S. conceptualized the research and prepared the manuscript. R.M. and S.K. performed the experiments and analyzed data. N.M. and A.S.N.S. conducted the RNA-seq analysis. P.B., M. Mehta, and M. Munshi constructed the knockout and complemented strains and conducted the HIV-TB coinfection and H_2S measurement assays. V.A. performed the flow sorting. V.K.A. and R.K.S. conducted the pharmacokinetic drug-drug interaction studies. R.S.R. conducted animal experiments.

Competing interests: The authors declare that they have no competing interests.

Data and materials availability: All data associated with this study are present in the paper or the Supplementary Materials. RNA-seq data generated and analyzed in this study have been uploaded to the NCBI Gene Expression Omnibus under accession number GSE123267.

Europe PMC Funders Author Manuscripts

tolerance in replicating *Mtb* and suggest repositioning of CQ to shorten TB therapy and achieve a relapse-free cure.

Introduction

An unusually long-term (6 months) therapy involving multiple antibiotics is required to cure tuberculosis (TB) in humans. This protracted treatment is necessary to prevent relapses due to genetically drug-sensitive bacteria that become transiently resistant inside host cells and tissues, a phenomenon called phenotypic drug tolerance. Thus, the mechanistic basis of phenotypic drug tolerance needs to be studied to develop new drugs with treatment-shortening properties. Recent studies indicate that heterogeneity in both the host environment and the bacterial population can promote phenotypic drug tolerance. For example, variability in the activation status of macrophages distinctly modulates drug tolerance in *Mycobacterium tuberculosis* (*Mtb*) (1). Immune activation of macrophages leads to release of antibacterial effectors such as reactive nitrogen species and reactive oxygen species (ROS) (2, 3), leading to a quiescent drug-tolerant state of *Mtb* (4). In support of this theme, drug tolerance is diminished in mice and macrophages deficient in producing nitric oxide (NO) (1). Moreover, extracellular *Mtb* present in the cavity caseum derived from *Mtb*-infected rabbits show slow replication and extreme tolerance to several first- and second-line anti-TB drugs (5). Single-cell measurements have revealed that stress conditions (for example, starvation) in vitro and host immune pressures (interferon-γ, a cytokine critical for anti-TB host immunity) in vivo create phenotypic heterogeneity within the *Mtb* population, which allows for the selection of nongrowing metabolically active bacteria responsible for postchemotherapeutic relapse (4).

However, recent studies suggest that adoption of a nongrowing state is not a prerequisite for drug tolerance (6–10). A fraction of both replicating and nonreplicating bacteria shows regrowth after drug withdrawal (4, 7), emphasizing that growth-arrested bacteria do not solely mediate tolerance. Alternate mechanisms—such as induction of drug efflux pumps, asymmetric cell division, and increased mistranslation rates—can contribute to substantial drug tolerance in actively multiplying cells (6, 8, 9, 11). Induction of efflux pumps is, so far, the only mechanism known to confer drug tolerance in replicating *Mtb* inside macrophages (6). Despite their importance, we lack understanding of macrophage-specific cue(s) and associated changes in the physiology of replicating *Mtb* that drive drug tolerance. Filling this knowledge gap will help in developing strategies to target both bacterial and host determinants crucial for mobilizing a drug-tolerant phenotype in vivo. A detailed summary of our current understanding of phenotypic drug tolerance in *Mtb* is described in fig. S1.

Using a ratiometric fluorescence biosensor (Mrx1-roGFP2) of the major mycobacterial antioxidant mycothiol (MSH), we previously showed that the environment inside macrophages rapidly generates heterogeneity in the MSH redox potential (E_{MSH}) of the *Mtb* population (12). Confocal and flow cytometry measurements categorized infected macrophages into two distinct populations, one predominantly harboring E_{MSH}-reduced bacteria (−300 ± 6 mV) and the other predominantly harboring E_{MSH}-basal bacteria (−275 ± 5 mV) (12). In addition, a minor fraction of infected macrophages was enriched for *Mtb* in

Europe PMC Funders Author Manuscripts

the E_{MSH}-oxidized state (−242 ± 6 mV) (12). These results are consistent with the heterogeneous and dynamic nature of both host and pathogen (13–15), suggesting that their interaction is likely to result in bacterial populations with diverse phenotypes. The E_{MSH}-reduced population was found to be refractory to anti-TB drugs compared to other populations (E_{MSH}-oxidized and E_{MSH}-basal) (12). Therefore, understanding the basis of redox heterogeneity could inform strategies that result in better targeting of drug-tolerant *Mtb*. In this study, we performed RNA sequencing (RNA-seq) of redox-altered intraphagosomal *Mtb* populations and identified bacterial factors and host cues associated with drug tolerance.

Results

Transcriptional profiling of redox-diverse populations identifies determinants of drug tolerance

We followed our previously developed flow cytometry protocol that averages median fluorescence ratio (405 nm/488 nm) of the Mrx1-roGFP2 biosensor expressed by intraphagosomal *Mtb* to gate macrophages into fractions enriched with either E_{MSH}-reduced (E_{MSH} = −300 ± 6 mV) or E_{MSH}-basal (E_{MSH} = −275 ± 5 mV) bacteria (fig. S2) (12). Using this gating strategy, we sorted THP-1 macrophages infected with *Mtb*/Mrx1-roGFP2 at 24 hours postinfection (p.i.), treated them with isoniazid [Inh; threefold the in vitro minimal inhibitory concentration (MIC)] for 48 hours, and confirmed that the E_{MSH}-reduced fraction is more tolerant to Inh than E_{MSH}-basal fraction (fig. S3). As reduced susceptibility to Inh originated from a population of intraphagosomal *Mtb*, our findings align with a recent consensus statement defining tolerance as the general ability of a population to survive longer antibiotic exposure (16). To investigate the physiological basis of the differential tolerance of redox-altered *Mtb*, we performed global transcriptional profiling by RNA-seq of E_{MSH}-reduced and E_{MSH}-basal populations derived from THP-1 macrophages flow-sorted 24 hours after infection with *Mtb*/Mrx1-roGFP2 (Fig. 1).

We isolated total bacterial RNA, performed RNA-seq, and analyzed data using DESeq2 (Fig. 1A). Control RNA was isolated from logarithmically grown *Mtb* resuspended in complete RPMI for 24 hours (in vitro control). We compared the transcription profiles of macrophage-derived populations to in vitro control and to one another to identify responses that were induced in both populations and responses that were significantly induced in E_{MSH}-reduced bacteria [false discovery rate (FDR), ≤0.05]. Principal components analysis and clustering of heat map plots showed that the three samples clustered by their biological replicates (fig. S4 and tables S1, A to C). As compared to the in vitro control, the expression of 560 and 617 genes was affected in the E_{MSH}-reduced and E_{MSH}-basal populations, respectively (FDR, ≤0.05; fold change, ≥1.5) (table S1, B and C). Of 295 genes showing overlap, 151 were more induced in the drug-tolerant E_{MSH}-reduced population (Fig. 1B and table S1D). The transcriptome of both populations considerably overlapped with that of a previously reported transcriptional signature of intraphagosomal *Mtb* ($P < 0.05$, Fisher's exact test; Fig. 1C) (17). Consistent with studies showing phagosomal acidification as the earliest cue that alters the transcriptome of *Mtb* inside unstimulated macrophages (18, 19), RNA-seq data of the E_{MSH}-reduced fraction overlapped significantly with the transcriptome

of *Mtb* grown in 7H9 broth at pH 5.5 ($P = 1.05 \times 10^{-2}$) and pH 4.5 ($P = 1.5 \times 10^{-15}$) (Fig. 1C) (17, 20). The E_{MSH}-basal transcriptome showed little similarity to the genes down-regulated at pH 5.5 (Fig. 1C) (17).

Using *Mtb*/Mrx1-roGFP2 conjugated with pHrodo dye, which emits fluorescence only in acidic pH (21), we infected THP-1 macrophages and confirmed phagosomal pH to be 6.25 ± 0.14, as previously reported for unstimulated macrophages (fig. S5) (22). Likewise, we examined the pH of flow-sorted macrophages enriched with E_{MSH}-basal or E_{MSH}-reduced bacteria. Macrophages enriched in E_{MSH}-reduced bacteria are more acidic (pH 5.79 ± 0.2) than E_{MSH}-basal bacteria (pH 6.67 ± 0.08) (fig. S5D), indicating that subtle variations in phagosomal pH underlie heterogeneity in E_{MSH} of *Mtb* during infection. We also compared the transcriptional profiles of E_{MSH}-altered *Mtb* and a mutant of the redox-sensitive transcription factor WhiB3 (*Mtb*Δ*whiB3*), which has been linked to *Mtb*'s transcriptional response to low pH (20). We isolated RNA from wild-type (WT) *Mtb*, *Mtb*Δ*whiB3*, and *whiB3*-complement (*whiB3*-Comp) cultured in 7H9 broth at neutral pH (6.6) and acidic pH (4.5) and performed RNA-seq. The WhiB3-specific, low pH–induced gene set showed comparable expression in the E_{MSH}-reduced population. In contrast, only a fraction of the WhiB3 regulon coincided with the transcriptome of E_{MSH}-basal bacteria, with lesser induction of the regulon than that seen in the case of the E_{MSH}-reduced *Mtb* (fig. S6 and table S2D). These findings link the transcriptome of E_{MSH}-reduced bacteria with *Mtb*'s response to low pH.

Low pH increases the solubility of transition metals including iron and copper (23), thereby allowing these metals to cross biological membranes and participate in metal-catalyzed ROS generation via the Fenton reaction (24). Consistent with this phenomenon, transcriptional sensors of metal toxicity (*furA*, *csoR*, and *cmtR*), exporters of toxic metals (*ctpV* and *ctpG*), redox sensors (*whiBs* and *sufR*), and antioxidant systems (*rubA/B*, *ahpC*, and *trxB2*) were induced in the E_{MSH}-reduced fraction (Fig. 1D and table S3). Because ROS damages DNA, proteins, and lipids, we observed that several genes implicated in DNA repair, protein quality control, and envelope stress were induced in E_{MSH}-reduced fraction (Fig. 1D and table S3). A previous study linked the stochastic expression of catalase (*katG*) in mediating Inh tolerance (7). However, *katG* expression was not differentially regulated in the E_{MSH}-reduced fraction, indicating that redox-mediated Inh tolerance is unrelated to *katG* expression. Genes coordinating glyoxylate and methyl citrate cycles (*icl1* and *prpD*) and alternate respiration (*cydAB*) were up-regulated in the E_{MSH}-reduced fraction (Fig. 1D and table S3); both *icl1* and *cydAB* are vital for mitigating oxidative stress and promoting multidrug tolerance in *Mtb* (25–27). The overlap between acidic pH and oxidative stress responses has been reported in several bacteria (28–30), indicating a link between pH- and oxidative stress–driven adaptations.

A reductive shift in the E_{MSH} of *Mtb* indicates an increase in the cytoplasmic pool of reduced MSH. Supporting this, genes associated with the biogenesis of cysteine (CySH), a component of MSH (31), were up-regulated in the E_{MSH}-reduced fraction. For example, *lat*, *metA*, and *metC* involved in methionine (Met) biogenesis (32), and *metB* encoding a bifunctional enzyme (cystathionine-γ-lyase/cystathionine-γ-synthase) that incorporates sulfur from Met to CySH (reverse transsulfuration pathway) (33) were induced in the E_{MSH}-

reduced fraction (Fig. 1D). The enzyme MetB generates H_2S gas as a by-product (33), which protects several bacterial species from antibiotics and oxidative stress (34–36). We detected that *Mtb* cultured in 7H9 broth at pH 6.2 and pH 4.5 generated more H_2S than at neutral pH (fig. S7), indicating a link between H_2S biogenesis, acid stress, and reductive shift in E_{MSH}. CySH also serves as a source of sulfide for the biogenesis of Fe-S clusters, which modulate bacterial response to antibiotics (37). Accordingly, genes involved in Fe-S cluster biogenesis [Rv1460 (*sufR*) and Rv1461 (*sufB*)] (38, 39) were up-regulated in the E_{MSH}-reduced fraction (Fig. 1D and table S3). Other transcriptional changes in E_{MSH}-reduced cells involving genes that are known to promote drug refractoriness include genes associated with *S*-adenosyl methionine (SAM) biosynthesis (*metK*) (32), methyl transferases (*menH*, Rv0560c, Rv1403c, and Rv1405c) (40–42), and drug efflux pumps (*mmr*, Rv1258c, and Rv1250) (6, 43, 44) (Fig. 1D and table S3). In conclusion, the RNA-seq data suggest a major role of host acidification and bacterial mechanisms involved in alleviating metal toxicity, ROS remediation, and realignment of sulfur metabolism in the emergence of drug-tolerant E_{MSH}-reduced population during infection.

CySH-disposal pathways coordinate redox-mediated drug tolerance in *Mtb*

CySH-dependent pathways such as biogenesis of H_2S, low molecular–weight thiols, and Fe-S clusters protect bacteria against antibiotics and oxidative stress (37, 45). In *Mtb*, supplementation with H_2S donor [sodium hydrosulfide NaHS)] restored the imbalance in the E_{MSH} of MSH recycling mutants (46), and Fe-S cluster–dependent regulators (for example, WhiB3 and WhiB7) mediate a reductive shift in E_{MSH} of *Mtb* in response to acidic pH and antibiotics (20, 47). On this basis, we reasoned that the induction of *metB* (H_2S biogenesis) and *sufR* (regulator of Fe-S cluster biogenesis) could contribute to the emergence of a drug-tolerant E_{MSH}-reduced population (Fig. 2A). To test this idea, we independently disrupted *metB* (*Mtb*Δ*metB*) and *sufR* (*Mtb*Δ*sufR*) in *Mtb* H37Rv (fig. S8, A to E). As expected, *Mtb*Δ*metB* displayed a reduced capability to produce H_2S compared to WT *Mtb* (fig. S8F). Similarly, disruption of *sufR* abrogated the induction of the *suf* operon (Rv1461 to Rv1466) involved in Fe-S cluster biogenesis (fig. S8G). Because WhiB3 promotes the emergence of E_{MSH}-reduced population inside macrophages (20), we used the *Mtb*Δ*whiB3* strain as a control. THP-1 macrophages infected with *Mtb*Δ*metB* or *Mtb*Δ*sufR* expressing Mrx1-roGFP2 showed a significant decrease in the reductive-E_{MSH} fraction compared to WT *Mtb* ($P < 0.01$) (Fig. 2B). We next examined the influence of these pathways on Inh tolerance during infection. THP-1 macrophages infected for 24 hours with *Mtb* strains were exposed to 3× in vitro MIC of Inh, and survival was determined at 48 hours of Inh treatment. Intramacrophage growth of the mutants was marginally reduced compared to WT *Mtb* (Fig. 2C). However, upon Inh treatment, *Mtb*Δ*metB*, *Mtb*Δ*sufR*, and *Mtb*Δ*whiB3* displayed 8.75-, 7-, and 9-fold reductions in survival compared to WT *Mtb*, respectively. Decreased tolerance displayed by these mutants was restored in the complemented strains to a degree similar to WT (Fig. 2C).

It can be argued that the loss of MetB and SufR functions can profoundly affect the normal growth and metabolism of *Mtb*, complicating any association with redox heterogeneity and drug tolerance. However, we found that the growth of *Mtb*Δ*metB* and *Mtb*Δ*sufR* in 7H9 broth was not different from WT *Mtb* (fig. S9, A and B). Furthermore, E_{MSH} of *Mtb*Δ*metB*

(−280 ± 3 mV) and *Mtb*Δ*sufR* (−276 ± 4 mV) remained comparable to WT *Mtb* (−275 ± 2 mV) in vitro. In addition, *metB* or *sufR* disruption did not perturb the oxygen consumption rate or extracellular acidification rate (fig. S9, C and D), quantifiable readouts of oxidative phosphorylation and glycolysis, respectively (48). Last, we examined whether *metB* and *sufR* influenced tolerance to Inh under acidic pH. The MIC of Inh remained comparable (0.06 to 0.1 μg/ml) for *Mtb*Δ*metB* and *Mtb*Δ*sufR* at neutral pH. However, at pH 4.5, WT *Mtb* showed 79 ± 3.97% survival to 10× MIC of Inh as compared to 19.79 ± 0.58% and 18.8 ± 1.85% in the case of *Mtb*Δ*metB* and *Mtb*Δ*sufR*, respectively (Fig. 2, D and E). These data indicate that *metB* and *sufR* influence drug tolerance in the context of acidic pH and the intramacrophage milieu. In sum, the genetic data support our RNA-seq findings indicating CySH flux as an important mechanism underlying redox diversity and drug tolerance in *Mtb* during infection.

Phagosomal acidification is required for the redox-dependent multidrug tolerance of *Mtb*

To clarify the link between phagosomal pH, redox heterogeneity, and drug tolerance during infection, we pretreated THP-1 macrophages with nontoxic doses of well-established inhibitors of phagosomal acidification [bafilomycin A1 (BafA1), ammonium chloride (NH_4Cl), and chloroquine (CQ)], infected them with *Mtb*/Mrx1-roGFP2, and measured E_{MSH} (12, 20, 49–51). Pretreatment with BafA1/NH_4Cl/CQ uniformly diminished the fraction of *Mtb* displaying reductive E_{MSH} at 24 hours p.i. (Fig. 3A). Next, we examined whether phagosomal pH enhanced drug tolerance during infection. THP-1 macrophages with or without BafA1 pretreatment were infected with *Mtb* for 24 hours and exposed to 3× MIC of Inh for an additional 48 hours before lysis and enumeration of viable counts. The addition of BafA1 further increased Inh-mediated killing of *Mtb* by fivefold (Fig. 3B). A similar increase in killing was observed upon substitution of Inh with rifampicin (Rif) or BafA1 with CQ (Fig. 3, B and C). We noted that although CQ and BafA1 uniformly increased killing efficacy of Inh and Rif, the effect was more pronounced in the case of Inh (Fig. 3, B and C). Consistent with findings in THP-1 cells, infection of peritoneal macrophages from BALB/c mice also led to a pH-dependent increase in the E_{MSH}-reduced fraction and Inh tolerance in *Mtb* (fig. S10, A and B). These results suggest that phagosomal pH is a potent enhancer of multidrug tolerance in *Mtb*.

We next examined whether the drug tolerance and redox heterogeneity displayed by intraphagosomal *Mtb* were a reversible phenotypic change or a stable genetic variation. We flow-sorted THP-1 macrophages infected with *Mtb*/Mrx1-roGFP2 for 24 hours into E_{MSH}-reduced and E_{MSH}-basal fractions, lysed the macrophages in 7H9 broth, and measured E_{MSH} of the released *Mtb*. Incubation in 7H9 broth resulted in the loss of redox heterogeneity within 2 hours, indicating that the macrophage environment supports the emergence of drug-tolerant E_{MSH}-reduced population (Fig. 3D). When these redox-homogeneous bacteria were used to reinfect THP-1 macrophages with or without CQ pretreatment, both the heterogeneity in E_{MSH} and tolerance to Inh returned in untreated macrophages but not in CQ-treated macrophages (Fig. 3, D and E). Last, the bacteria that survived Inh treatment inside THP-1 macrophages showed an MIC comparable to the parental strain in 7H9 broth (fig. S10C). We conclude that pH- and redox-dependent tolerance of *Mtb* inside macrophages was due to reversible phenotypic changes rather than stable genetic mutations.

Phagosomal pH and redox heterogeneity drive drug tolerance during HIV-TB coinfection

Limited acidification is one of the hallmarks of *Mtb*-containing alveolar macrophages derived from HIV-TB–coinfected patients (52). We reasoned that pH- and redox-driven tolerance to anti-TB drugs could contribute to the lower TB treatment success rates commonly observed in HIV-TB–coinfected patients (53). To test this idea, we used the U1 monocytic cell line model of HIV-TB coinfection (54). U1 cells are derived from U937 monocytes wherein two copies of the HIV-1 genome are integrated and viral replication can be induced by phorbol 12-myristate 13-acetate (PMA) and tumor necrosis factor–α(55, 56). We confirmed viral replication by monitoring the expression of the HIV-1 *gag* transcript by quantitative reverse transcription polymerase chain reaction (qRT-PCR). Treatment with PMA (5 ng/ml) induced HIV-1 replication in a time-dependent manner in U1 cells (Fig. 4A). Next, we infected PMA-treated U1 and U937 (uninfected HIV-1 control) with *Mtb*/Mrx1-roGFP2 and measured heterogeneity in E_{MSH}. Both U1 and U937 macrophages showed the emergence of redox-diverse fractions upon infection. However, a marked increase in the E_{MSH}-reduced fraction was clearly evident in U1 compared to U937 macrophages (Fig. 4, B and C), indicating that HIV-1 replication is accompanied with the rise of E_{MSH}-reduced population. Furthermore, treatment with BafA1, NH_4Cl, and CQ uniformly decreased the E_{MSH}-reduced fraction in U1 (Fig. 4D), confirming the role of phagosomal pH in the emergence of redox heterogeneity. Last, we tested Inh tolerance in U1 and U937 cells, as described earlier. Consistent with the increased E_{MSH}-reduced fraction, a significantly higher proportion of *Mtb* tolerates exposure to 3× MIC of Inh in U1 (65.9 ± 11.67%) versus U937 (21.93 ± 0.42%) ($P = 0.0015$) (Fig. 4, E and F). As expected, pretreatment with CQ/BafA1 increased Inh-mediated killing of *Mtb* in U1 and U937 (Fig. 4, E and F). These results suggest that the phagosomal acidification encountered by *Mtb* inside HIV-*Mtb*–coinfected macrophages facilitates the development of a redox-altered drug-tolerant population.

The drug-tolerant E_{MSH}-reduced population is replicative inside macrophages

We next examined whether drug tolerance exhibited by the E_{MSH}-reduced population is associated with slow replication as shown in several bacteria, including *Mtb* (1, 4, 57). We used an unstable replication clock plasmid, pBP10, which is uniformly lost from replicating but not from nonreplicating *Mtb* (58). Because the plasmid is resistant to kanamycin (Kan), its retention or loss can be easily estimated by determining colony-forming units (CFUs) on Kan-containing medium. We infected THP-1 macrophages with pBP10-containing *Mtb*/Mrx1-roGFP2. At 0, 24, and 72 hours p.i., 0.5×10^6 macrophages harboring an E_{MSH}-reduced or E_{MSH}-basal population were flow-sorted, after which, the bacteria were released and differences in replication were measured by enumerating Kan^r (Kan-resistant) and Kan^s (Kan-sensitive) colonies. Expression of the pBP10 plasmid in *Mtb*/Mrx1-roGFP2 did not influence redox heterogeneity during infection (fig. S11A). The pattern of pBP10 plasmid loss indicated that both populations were replicative; however, the plasmid loss was faster over time in the E_{MSH}-reduced population than the E_{MSH}-basal population (Fig. 5, B and C). For example, at 72 hours p.i., only 17.8 ± 0.2% of cells retained pBP10 in the E_{MSH}-reduced population as opposed to 61.19 ± 0.02% in the E_{MSH}-basal population (Fig. 5, B and C). The cumulative bacterial burden, which provides the total number of living, dead, or damaged *Mtb* based on a mathematical model established for the clock plasmid (58), also

confirmed the comparatively higher replication rate in the E_{MSH}-reduced population (Fig. 5, B and C).

We examined the health of *Mtb* in the E_{MSH}-reduced and E_{MSH}-basal fractions using a fluorogenic cell-permeable dye calcein violet–acetoxy-methyl ester (CV-AM), an established metabolic indicator (59, 60). THP-1 macrophages infected for 24 hours with *Mtb*/Mrx1-roGFP2 were flow-sorted, and then, bacteria were released from the E_{MSH}-reduced and E_{MSH}-basal fractions and stained with CV-AM. Bacilli in the E_{MSH}-reduced (91.5 ± 0.07%) and E_{MSH}-basal fractions (99.1 ± 0.14%) showed strong CV-AM fluorescence, indicating healthy metabolic activity (Fig. 5D). As expected, metabolically active *Mtb* cultured in 7H9 broth at 37°C showed 91.3 ± 0.99% CV-AM staining as compared to negligible staining in bacteriostatic cells incubated at 4°C (Fig. 5D). Treatment of *Mtb*/Mrx1-roGFP2 with 2 mM cell-permeable thiol-reductant dithiothreitol (DTT) induces a reductive shift in E_{MSH} (−320 mV) without any influence on metabolism and viability in vitro (20). Consistent with this, 83.9 ± 2.97% of DTT-treated *Mtb* cells scored positive for CV-AM staining (Fig. 5D). Together, these results suggest that the drug-tolerant E_{MSH}-reduced population is replicative and metabolically active inside macrophages.

Redox-diverse populations of *Mtb* show differential activation of efflux pumps

Induction of efflux pumps is associated with drug tolerance in replicating *Mtb* during infection (6). We investigated whether the drug-tolerant E_{MSH}-reduced population exhibited variation in efflux pump activity relative to the E_{MSH}-basal population. THP-1 macrophages infected for 24 hours with *Mtb*/Mrx1-roGFP2 were flow-sorted into E_{MSH}-reduced and E_{MSH}-basal populations, and bacterial RNA was isolated for qRT-PCR of efflux pump transcripts. As a control, we performed qRT-PCR of efflux pumps on *Mtb* grown in 7H9 broth. We selected efflux pumps (Rv0194, Rv1348, Rv1250, *ctpV*, *mmr*, and Rv1819c) that are induced in intraphagosomal *Mtb* upon exposure to anti-TB drugs (44, 61–64). The transcripts of *ctpV*, *mmr*, Rv1348, and Rv1250c were enriched in the E_{MSH}-reduced fraction (Fig. 5E). We tested pH- and redox-dependent expression of efflux pumps by examining transcripts in response to pH 6.2, pH 4.5, and 2 mM DTT in vitro. Each of these conditions uniformly induces reductive shift in E_{MSH} of *Mtb* in vitro (12, 20). All of these treatments increased expression of the efflux pumps (fig. S11, B and C). As a control, we analyzed efflux pump expression in an *Mtb* strain lacking the antioxidant buffer MSH (*Mtb*Δ*mshA*); this strain maintains oxidative E_{MSH} (>−240 mV) at both neutral and acidic pH (20, 65). The expression of pH-inducible efflux pumps was significantly down-regulated in *Mtb*Δ*mshA* relative to WT *Mtb* ($P < 0.05$) (fig. S11D), suggesting redox-dependent regulation of efflux pump expression in *Mtb*.

To clarify the association between efflux pump activity and E_{MSH} of *Mtb*, we assessed the steady-state distribution of Inh in E_{MSH}-reduced and E_{MSH}-basal populations inside THP-1 macrophages using [^{14}C]-labeled Inh. We infected THP-1 macrophages with *Mtb*/Mrx1-roGFP2 cells preloaded with [^{14}C]-Inh (0.5 μCi/ml for 2 hours). At 24 hours p.i., equal numbers of macrophages harboring either E_{MSH}-reduced or E_{MSH}-basal populations were sorted using flow cytometry. We chose the 24-hour time point because bacterial load was comparable in both populations (10^6 CFU/ml). Infected macrophages were lysed, the

bacterial (pellet) and macrophage (supernatant) fractions were separated, and [^{14}C]-labeled Inh radioactivity was measured. The distribution of [^{14}C]-Inh was different in macrophages containing E_{MSH}-reduced *Mtb* versus E_{MSH}-basal *Mtb* and in the bacteria themselves. Whereas macrophages harboring E_{MSH}-reduced *Mtb* showed high counts for [^{14}C]-Inh and corresponding lower counts remained in the bacteria, the E_{MSH}-basal population showed an inverse drug distribution. These data indicate higher efflux from the E_{MSH}-reduced population into macrophages (Fig. 5F). Direct comparison of [^{14}C]-Inh counts in E_{MSH}-reduced and E_{MSH}-basal bacterial pellets confirmed lower accumulation of the drug in the former (Fig. 5F). In summary, our data indicate that variations in efflux pump activity can be one of the factors managing drug tolerance in the E_{MSH}-reduced population during infection.

CQ counteracts drug tolerance and relapse in vivo

Given our findings that acidic pH promotes redox heterogeneity and enhances drug tolerance in vitro, we sought to determine the impact of pharmacological inhibition of phagosomal acidification on drug tolerance in vivo. We used the antimalarial drug CQ, which deacidifies endosomes and lysosomes (66, 67), to test *Mtb*'s response to Inh in a chronic murine model of infection (Fig. 6A) (68).

We treated chronically infected BALB/c mice (4 weeks p.i.) with Inh (25 mg/kg body weight), CQ (10 mg/kg body weight), or Inh along with CQ. After 2 and 8 weeks of therapy, we harvested the lungs and quantified the recovered bacteria. As reported (68), Inh monotherapy reduced the bacterial load from 10^6 to 10^4 at 2 weeks ($P = 0.00012$) and 10^3 per lung at 8 weeks ($P = 0.0022$) of treatment (Fig. 6B). CQ treatment alone showed no effect on bacterial viability over time (Fig. 6B). Relative to the control regimen (Inh alone), the addition of CQ did not alter lung CFUs after 2 weeks of treatment (Fig. 6B). However, 8 weeks of treatment with a combination of CQ with Inh (CQ plus Inh) completely sterilized the lungs of mice compared to 10^3 CFUs in the animals treated with Inh alone (Fig. 6B). The gross and histopathological changes observed in the lungs after 8 weeks of therapy were proportionate with the bacillary load observed (Fig. 6, D and E, and fig. S12A). After 8 weeks of treatment, the extent of pulmonary tissue destruction was highest in the untreated (score, 4) and CQ-treated animals (score, 3), intermediate in the case of the Inh-treated animals (score, 2), and negligible in CQ plus Inh–treated animals (score, 1 or 0). We also examined whether adjunct therapy with CQ for 8 weeks increased the efficacy of Rif (10 mg/kg body weight). The addition of CQ substantially reduced the fraction of Rif-tolerant *Mtb* in animal lungs ($P = 0.021$ for Rif alone versus a combination of CQ with Rif) (Fig. 6, C to E, and fig. S12A). However, the influence of CQ in reducing tolerance was more notable in the case of Inh as compared to Rif.

Because the pathophysiology of human TB is more closely recapitulated in guinea pigs (69), we aerosol-infected outbred Hartley guinea pigs with *Mtb*, followed 4 weeks later by treatment with Inh, CQ, or CQ plus Inh for an additional 8 weeks, and then estimated the lung bacillary load. The bacterial burden in the lungs of guinea pigs was 10^3 CFUs in Inh-treated animals and 10^5 CFUs in CQ-treated animals, compared to 100 CFUs in CQ plus Inh–treated animals (Fig. 6F). The effectiveness of CQ plus Inh was also reflected in the lung histopathology of guinea pigs (Fig. 6G and fig. S12B). Studying relapse can be another

predictor of therapeutic efficacy in TB. Therefore, we aerosol-infected mice with WT *Mtb*, followed 4 weeks later by treatment of infected animals with Inh or CQ plus Inh for 8 weeks. As shown earlier, 8 weeks of CQ plus Inh treatment completely sterilized mouse lungs. At 20 weeks p.i., which was 8 weeks after completion of therapy, mice received immunosuppressant dexamethasone (10 mg/kg body weight) for 2 weeks, and the lung bacillary load was determined at 22 weeks p.i. Relapse of disease was observed in five of five Inh-treated mice with bacterial loads of 2×10^4 CFUs in the lungs. Only three of five CQ plus Inh–treated mice relapsed, with only 30 CFUs in the lungs ($P = 0.0069$) (Fig. 6H).

Although in vitro studies indicate that CQ mainly exerts its influence on intracellular *Mtb* by raising the vacuolar pH (70), CQ can interfere with other cellular processes such as DNA synthesis, generation of ROS, and necrosis (71, 72). Therefore, we questioned whether the effect of CQ in reducing tolerance was associated with pH alkalization in vivo. Using Magic Red cathepsin B substrate that fluoresces only upon cleavage by cathepsin B protease inside acidic lysosomes (73), we confirmed that 6 weeks of CQ treatment raised the vacuolar pH of macrophages isolated from the lungs of mice chronically infected with *Mtb* (fig. S13, A and B). Other antibacterial mechanisms such as ROS production and necrosis were not stimulated in macrophages derived from the lungs of mice chronically infected with *Mtb* after 6 weeks of treatment with CQ plus Inh as compared to Inh or CQ alone (fig. S13, A, C, and D). Together, these results confirm that adjunct therapy with CQ counteracts drug tolerance and reduces disease relapse.

CQ exhibits no adverse interaction with anti-TB drugs

Excellent oral bioavailability, oral human pharmacokinetics (half-life of 10 to 15 days), high tissue penetration, and years of clinical use in humans (74) make CQ a good candidate for developing new therapeutic combinations for the treatment of TB. We investigated the pharmacological compatibility of CQ by measuring its potential drug-drug interactions with first-line anti-TB drugs (Inh or H, Rif or R, Emb or E, and Pza or Z) given as a combination. A single-dose pharmacokinetic interaction test was performed by administering anti-TB drugs with and without CQ [10 mg/kg body weight, intraperitoneally (i.p.)] in mice. Another group of mice was dosed with CQ (10 mg/kg body weight, i.p.) to compare the pharmacokinetic behavior of CQ in the presence of combination therapy (Fig. 7A). Plasma samples were analyzed for individual drugs using liquid chromatography–mass spectrometry, and key pharmacokinetic parameters such as maximum plasma concentration (C_{max}) and area under the plasma concentration-time curve (AUC_{last}) were calculated as a ratio for combination versus single-treatment groups. Pharmacokinetic profiles revealed no adverse drug-drug interactions when CQ was coadministered with HREZ (Fig. 7, B and G). C_{max} and AUC_{last} for CQ alone was 228.5 ng/ml and 1358.0 ng·hour/ml and 297.2 ng/ml and 1358.0 ng·hour/ml for HREZ, respectively (Fig. 7, B and G).

The plasma pharmacokinetic profiles of anti-TB drugs remained largely unchanged in the presence of CQ. We observed no major interaction for Rif, Emb, or Pza in the presence or absence of CQ (Fig. 7, D to G) because C_{max} and AUC_{last} were within 80 to 125% criteria for equivalence (Fig. 7G) (75). Comparative ratios of C_{max} and AUC_{last} for Rif, Emb, and Pza, with and without CQ, were close to one except for Inh, which showed a minor

interaction (C_{max} ratio, 0.685), although AUC_{last} was not affected (Fig. 7, C and G). This minor influence of CQ on the pharmacokinetics of Inh may be due to the effect of CQ in reducing Inh influx in the intestines (76). Overall, the pharmacokinetic results suggested no adverse drug-drug interactions between the HREZ combination regimen versus CQ and vice versa. In summary, our study shows an effect of CQ on drug susceptibility, no major drug-drug interaction with HREZ, and enhanced in vivo efficacy of CQ-based combinations. With years of safe clinical history for CQ, these findings suggest that CQ could be repurposed for developing new curative combinations for TB.

Discussion

Generation of phenotypic heterogeneity and metabolic quiescence in response to stresses induced by immune activation is the most commonly invoked mechanism of antibiotic tolerance in *Mtb* (1, 4). However, clinical evidence in humans indicates that tolerance can also be associated with growing bacterial populations (77, 78). Consistent with this idea, early tolerance was documented in actively multiplying *Mycobacterium marinum* and *Mtb* in zebrafish larvae and in macrophages, respectively (6). In the present study, we showed a dominant role of phagosomal acidification in facilitating heterogeneity in the redox physiology of *Mtb* to generate an actively replicating, drug-tolerant population exhibiting higher antioxidant capacity (E_{MSH}-reduced) during infection. Our study constitutes an important foundation linking the macrophage environment with the core redox physiology of *Mtb* to promote drug tolerance in replicating *Mtb*, a population not typically associated with tolerance.

Host-induced oxidative stress is a major environmental stress encountered by *Mtb* during infection and is further exacerbated by anti-TB drugs (12, 79). Because a modest decrease in vacuolar pH is the earliest cue *Mtb* encounters (18), a pH-dependent reductive shift in E_{MSH} might offer cross-protection to oxidative stress generated by immune activation and drugs. This is supported by the identification of a small molecule (AC2P36) that interferes with thiol homeostasis at acidic pH and increases vulnerability to antibiotics in vitro (80). We also found that the expression of drug efflux pumps and consequent accumulation of antibiotics in *Mtb* populations are also dependent on the pH-induced remodeling of intramycobacterial E_{MSH}. Because efflux pumps have recently been shown to export oxidatively damaged proteins in *Mtb* (81), the pH-responsive induction of efflux pumps may be an elegant adaptation strategy to maintain redox homeostasis and tolerance in the face of antibiotics and host immune pressures. Consistent with this idea, the *Mtb* Rv1258c efflux pump is required for both survival and drug efflux during infection (6).

Because acidic pH encountered inside macrophages does not perturb intramycobacterial pH homeostasis (82), it is more likely that the phagosomal pH-dependent selection of an E_{MSH}-reduced population is part of a bacterial adaptation program during infection. In support of this notion, we have recently found that a redox-sensitive transcription factor, WhiB3, is required to generate an E_{MSH}-reduced population in response to phagosomal acidification (20). As a consequence, a WhiB3-deficient strain showed a growth defect in macrophages and guinea pigs (34) and also exhibited increased susceptibility to Inh. Acidic pH-mediated changes in gene expression and redox potential of *Mtb* were also reported to be dependent

on the PhoPR two-component system (83), indicating overlapping roles of WhiB3/PhoPR in modulating *Mtb* adaptation to pH stress. Data from our transcriptional profiling also align with the adaptation model wherein the drug-tolerant population (E_{MSH}-reduced) showed enhanced expression of stress-responsive regulons relative to the drug-sensitive fraction (E_{MSH}-basal) inside macrophages. However, although heterogeneity in *Mtb* populations has been reported during infection (4, 78), it was unclear whether there were variations in the expression of stress regulons or virulence factors in *Mtb* populations as seen with other pathogens including *Salmonella typhimurium* and *Yersinia pseudotuberculosis* (84, 85). Our data demonstrate heterogeneity in the expression of several regulators involved in sensing toxic metals and oxidative stress in redox-altered populations. We also observed a major realignment of sulfur metabolism and proposed that the flux of reduced sulfur metabolites such as CySH into Fe-S cluster assembly, reverse transsulfuration, SAM biosynthesis, and MSH biosynthesis is likely to coordinate *Mtb*'s defense against antibiotics. Deviations in CySH flux contribute to potentiation of the mycobactericidal efficacy of anti-TB drugs (86). Furthermore, increased expression of SAM-dependent methyl transferases in E_{MSH}-reduced bacteria can promote drug tolerance by *N*-methylation of antibiotics (40). These transcriptional changes—along with the reduced tolerance shown by *Mtb*Δ*metB*, *Mtb*Δ*sufR*, and *Mtb*Δ*whiB3*—led us to propose a model of how phagosomal acidification and bacterial pathways integrate to reset *Mtb*'s redox physiology for successfully counteracting anti-TB drugs (fig. S14).

Our data also suggest that redox-dependent drug tolerance in replicating *Mtb* is multifactorial. Although the deletion of single redox-responsive pathways (WhiB3, SufR, and MetB) exhibited substantial influence on drug tolerance, complete clearance of *Mtb* was not achieved. Similar to our findings, drug tolerance in the growth-arrested *Mtb* population possibly requires activation of multiple stress regulons and toxin-antitoxin modules (DosR, PhoP, MprA, and MazEF) (1). These studies imply that targeting few bacterial genes or pathways is unlikely to severely affect the ability of *Mtb* to mobilize drug tolerance in response to host-induced pressures. Conversely, targeting host cues that alter the physiology of *Mtb* could be an effective mechanism to diminish phenotypic heterogeneity-driven drug tolerance. Our animal data showing the nearly sterilizing effect of CQ in combination with anti-TB drugs provide a compelling argument for targeting vacuolar pH to subvert early emergence of drug tolerance in vivo. Although CQ reinstates redox homogeneity and drug susceptibility mainly by increasing phagosomal pH, other immunomodulatory properties of CQ such as iron depletion (70), blocking phagosomal maturation and autophagy (66), and reversing inflammation-dependent efflux pumps (51) could also contribute to the effect of CQ on multidrug tolerance in vivo. It has been recently shown that CQ potentiates the antimycobacterial activity of Inh and Pza in immune-activated macrophages (51). Because shortening TB chemotherapy requires rapid sterilization of *Mtb*, our study provides empirical evidence that targeting phagosomal acidification by small molecules has the potential to provide relapse-free control by subverting redox heterogeneity. Because CQ is clinically used, stable, cost effective, and highly tolerable with few side effects, it can be conveniently repurposed to formulate new combinations with the current anti-TB regimen to reduce therapy duration. CQ also reduced redox heterogeneity and Inh tolerance in a HIV-TB coinfection background. Along with clinical evidence showing anti-HIV properties of

CQ (87), this raises the possibility of potentiating current anti-TB and anti-HIV therapies by CQ. Last, redox-mediated multidrug tolerance may be relevant to other chronic pathogens. For example, heightened antioxidant capacity is linked to the acquisition of phenotypic antibiotic resistance in the human pathogen *Pseudomonas aeruginosa* (88). Thus, our findings may have broad relevance to several human pathogens where a sterilizing cure is therapeutically challenging.

Although CQ therapy reduced drug tolerance in vivo, several issues remain to be addressed before it can be combined with the standard anti-TB therapy. First, it needs to be investigated whether a combination of CQ with current therapeutic regimens reduces therapy duration and facilitates the development of immunological memory to prevent relapse. Second, the efficacy of CQ in shortening regimens for drug-resistant *Mtb* infections remains to be evaluated. Third, despite treatment with anti-TB drugs, *Mtb* cells persist in animal tissues and the sputum of patients with TB in a metabolically altered state and remain undetectable by viable counts (89, 90). It will be interesting to investigate the impact of CQ on these heterogeneous subpopulations of *Mtb* that are difficult to detect and retain persister phenotypes in animal models. All these issues require further experimentation using animal models and prospective clinical trials to properly test the efficacy of CQ as adjunct anti-TB therapy.

Materials and Methods

Study design

The overall objective of this study was to evaluate host and bacterial mechanisms underlying the emergence of redox heterogeneity and drug tolerance in *Mtb* during infection. First, we characterized the transcriptome of redox-diverse *Mtb* fractions (E_{MSH}-reduced and E_{MSH}-basal), which led to the identification of CySH metabolism of *Mtb* and phagosomal acidification as important factors coordinating redox-mediated drug tolerance inside macrophages. Next, we performed detailed mechanistic studies on the role of phagosomal acidification in generating drug-tolerant E_{MSH}-reduced bacteria in macrophages infected with *Mtb* alone or coinfected with HIV-1. We applied multiple approaches to studying replication dynamics, metabolic status, and efflux pump activity in E_{MSH}-reduced and E_{MSH}-basal *Mtb* inside macrophages. We then evaluated the licensed antimalarial drug CQ, which deacidifies phagosomes, in reducing tolerance to standard anti-TB drugs and relapse in animal models of *Mtb* infection. We assessed the pharmacological compatibility of CQ with first-line anti-TB drugs in mice. Animals were randomly allocated into groups and were identifiable with respect to their treatment. All studies were carried out as per guidelines prescribed by the Committee for the Purpose of Control and Supervision of Experiments on Animals, Government of India, with approval from the Institutional Animal Ethical Committee. Drug treatment and euthanasia were carried out in humane ways to minimize suffering for animals. All experiments were carried out in a biosafety level 3 containment facility and approved by the Institutional Biosafety Committee.

In vivo experiments

For the chronic model of infection (68), 4- to 6-week-old female BALB/c mice ($n = 6$ per group) were infected by the aerosol route with 100 *Mtb* H37Rv bacilli using a Madison chamber aerosol generation instrument, housed for 4 weeks for progression of infection, and then left untreated or started under various treatment conditions: (i) 10 mg/kg body weight intraperitoneal doses of CQ on alternate days, (ii) 25 mg/kg body weight of Inh in drinking water daily, (iii) 10 mg/kg body weight of Rif in drinking water daily, (iv) a combination of CQ and Inh (CQ plus Inh) at earlier mentioned doses, and (v) a combination of CQ and Rif (CQ plus Rif) at the mentioned doses (68). At indicated time points of treatment, mice were euthanized, and the lungs were harvested for bacterial burden, gross pathology, and tissue histopathology analysis. The upper right lobe of the lungs of animals from each group was fixed in 10% neutral-buffered formalin. Fixed tissues were prepared as 5-μm-thick sections, embedded in paraffin, and stained with hematoxylin and eosin. Tissue sections were coded, and coded sections were analyzed by a certified pathologist to assess for granuloma formation and lung damage (91). Remaining tissue samples were homogenized in 2 ml of sterile 1× phosphate-buffered saline (PBS), serially diluted, and plated on 7H11-OADC agar plates supplemented with lyophilized BBL MGIT PANTA antibiotic mixture (polymyxin B, amphotericin B, nalidixic acid, trimethoprim, and azlocillin, as supplied by BD). Plates were incubated at 37°C for 3 weeks before colonies were enumerated.

For mice receiving treatment with Inh alone or a combination of CQ and Inh, all treatments were stopped at 12 weeks p.i. (when animals were found to be culture negative for *Mtb*) for remaining animals ($n = 5$ per group). Animals were further housed for 8 weeks without treatment, after which four intraperitoneal doses of dexamethasone at 10 mg/kg body weight were administered over 2 weeks for pan-immunosuppression. In the 22nd week p.i., animals in both groups were euthanized, and lung burden of reactivated *Mtb* was determined by plating lung homogenates for CFUs, as mentioned earlier.

Outbred Hartley guinea pigs ($n = 5$ per group) were given an aerosol challenge of 100 *Mtb* H37Rv (92) using a Madison chamber aerosol generation instrument, housed for 4 weeks for progression of infection, and then left untreated or started on treatment in one of three groups: (i) 5 mg/kg body weight intraperitoneal doses of CQ on alternate days, (ii) 30 mg/kg body weight of Inh in drinking water daily, and (iii) a combination of CQ and Inh (CQ plus Inh) at earlier mentioned doses. At 8 weeks after commencement of treatment, guinea pigs were euthanized, and lung burden of *Mtb* was determined by homogenizing organs in 5 ml of sterile 1× PBS, serial dilution, and plating on 7H11-OADC agar plates supplemented with PANTA. Upper right lobes of the lungs from different treatment groups were fixed in neutral-buffered formalin and prepared, as mentioned earlier, for histopathological analysis (91).

Statistical analysis

All statistical analyses were performed using GraphPad Prism software (version 6.0). All data indicated are means ± SD except figs. S12 and S13, where median ± interquartile range was plotted for animal groups. The Mann-Whitney rank sum test was used for comparison of nonparametric data between two experimental groups. Nonparametric multiple group

comparisons were analyzed using the Kruskal-Wallis test with Dunn's post hoc correction. For overlap analysis of differentially expressed (DE) genes with other microarray studies, the significance of gene number overlap was determined by Fisher's exact test on a two-by-two contingency table (93). Differences with $P < 0.05$ were considered significant.

Supplementary Material

Refer to Web version on PubMed Central for supplementary material.

Acknowledgments

We are grateful to C. Grundner at the Seattle Children's Research Institute for critical reading of the manuscript and valuable input. We acknowledge W. R. Jacobs Jr. at the Albert Einstein College of Medicine for the *Mtb*Δ*mshA* mutant and D. J. V. Beste at the University of Surrey for providing the zeocin-marked vector pANEE001. C. N. Naveen at the Foundation of Neglected Disease Research (FNDR), India is acknowledged for supporting pharmacokinetic and drug-drug interaction studies in mice. We thank S. Nayak for valuable discussions about the key findings of the study and designing of schematics and models. We acknowledge the CIDR BSL-3 facility, Indian Institute of Science (IISc) for carrying out experiments with *Mtb* and A. Pandit and the NGS facility, NCBS for RNA-seq. The *mshA* mutant of *Mtb* was obtained from W. R. Jacobs Jr. under a material transfer agreement (MTA) between the Albert Einstein College of Medicine of Yeshiva University and the International Centre for Genetic Engineering and Biotechnology.

Funding

This work was supported by Wellcome Trust–DBT India Alliance grant IA/S/16/2/502700 (to A.S.); in part, by Department of Biotechnology (DBT) grants BT/PR11911/BRB/10/1327/2014 and BT/PR13522/COE/34/27/2015 (to A.S.); and by the DBT-IISc Partnership Program (22-0905-0006-05-987436). A.S. is a senior fellow of Wellcome Trust–DBT India Alliance. A.S.N.S. is supported by the Wellcome Trust–DBT India Alliance Grant IA/I/16/2/5-2711. R.M. is supported by the IISc, Bengaluru. S.K. and M. Mehta are national postdoctoral fellows supported by the Department of Science and Technology (DST), India. N.M. is supported by the National Centre for Biological Sciences—Tata Institute of Fundamental Research (NCBS-TIFR), Bengaluru. P.B. is supported by a fellowship provided by the Council of Scientific and Industrial Research (CSIR), India.

References

1. Liu Y, Tan S, Huang L, Abramovitch RB, Rohde KH, Zimmerman MD, Chen C, Dartois V, VanderVen BC, Russell DG. Immune activation of the host cell induces drug tolerance in *Mycobacterium tuberculosis* both in vitro and *in vivo*. J Exp Med. 2016; 213:809–825. [PubMed: 27114608]
2. MacMicking J, Xie Q-W, Nathan C. Nitric oxide and macrophage function. Annu Rev Immunol. 1997; 15:323–350. [PubMed: 9143691]
3. MacMicking JD, North RJ, LaCourse R, Mudgett JS, Shah SK, Nathan CF. Identification of nitric oxide synthase as a protective locus against tuberculosis. Proc Natl Acad Sci USA. 1997; 94:5243–5248. [PubMed: 9144222]
4. Manina G, Dhar N, McKinney JD. Stress and host immunity amplify *Mycobacterium tuberculosis* phenotypic heterogeneity and induce nongrowing metabolically active forms. Cell Host Microbe. 2015; 17:32–46. [PubMed: 25543231]
5. Sarathy JP, Via LE, Weiner D, Blanc L, Boshoff H, Eugenin EA, Barry CE III, Dartois A. Extreme drug tolerance of *Mycobacterium tuberculosis* in caseum. Antimicrob Agents Chemother. 2018; 62:e02266–17. [PubMed: 29203492]
6. Adams KN, Takaki K, Connolly LE, Wiedenhoft H, Winglee K, Humbert O, Edelstein PH, Cosma CL, Ramakrishnan L. Drug tolerance in replicating mycobacteria mediated by a macrophage-induced efflux mechanism. Cell. 2011; 145:39–53. [PubMed: 21376383]
7. Wakamoto Y, Dhar N, Chait R, Schneider K, Signorino-Gelo F, Leibler S, McKinney JD. Dynamic persistence of antibiotic-stressed mycobacteria. Science. 2013; 339:91–95. [PubMed: 23288538]

8. Aldridge BB, Fernandez-Suarez M, Heller D, Ambravaneswaran V, Irimia D, Toner M, Fortune SM. Asymmetry and aging of mycobacterial cells lead to variable growth and antibiotic susceptibility. Science. 2012; 335:100–104. [PubMed: 22174129]
9. Rego EH, Audette RE, Rubin EJ. Deletion of a mycobacterial divisome factor collapses single-cell phenotypic heterogeneity. Nature. 2017; 546:153–157. [PubMed: 28569798]
10. Sakatos A, Babunovic GH, Chase MR, Dills A, Leszyk J, Rosebrock T, Bryson B, Fortune SM. Posttranslational modification of a histone-like protein regulates phenotypic resistance to isoniazid in mycobacteria. Sci Adv. 2018; 4:eaao1478. [PubMed: 29732401]
11. Javid B, Sorrentino F, Toosky M, Zheng W, Pinkham JT, Jain N, Pan M, Deighan P, Rubin EJ. Mycobacterial mistranslation is necessary and sufficient for rifampicin phenotypic resistance. Proc Natl Acad Sci USA. 2014; 111:1132–1137. [PubMed: 24395793]
12. Bhaskar A, Chawla M, Mehta M, Parikh P, Chandra P, Bhave D, Kumar D, Carroll KS, Singh A. Reengineering redox sensitive GFP to measure mycothiol redox potential of *Mycobacterium tuberculosis* during infection. PLOS Pathog. 2014; 10:e1003902. [PubMed: 24497832]
13. Marakalala MJ, Martinez FO, Plüddemann A, Gordon S. Macrophage heterogeneity in the immunopathogenesis of tuberculosis. Front Microbiol. 2018; 9:1028. [PubMed: 29875747]
14. Helaine S, Thompson JA, Watson KG, Liu M, Boyle C, Holden DW. Dynamics of intracellular bacterial replication at the single cell level. Proc Natl Acad Sci USA. 2010; 107:3746–3751. [PubMed: 20133586]
15. Helaine S, Cheverton AM, Watson KG, Faure LM, Matthews SA, Holden DW. Internalization of *Salmonella* by macrophages induces formation of nonreplicating persisters. Science. 2014; 343:204–208. [PubMed: 24408438]
16. Balaban NQ, Helaine S, Lewis K, Ackermann M, Aldridge B, Andersson DI, Brynildsen MP, Bumann D, Camilli A, Collins JJ, Dehio C, et al. Definitions and guidelines for research on antibiotic persistence. Nat Rev Microbiol. 2019; 17:441–448. [PubMed: 30980069]
17. Rohde KH, Abramovitch RB, Russell DG. *Mycobacterium tuberculosis* invasion of macrophages: Linking bacterial gene expression to environmental cues. Cell Host Microbe. 2007; 2:352–364. [PubMed: 18005756]
18. Armstrong JA, Hart PD. Response of cultured macrophages to *Mycobacterium tuberculosis* with observations on fusion of lysosomes with phagosomes. J Exp Med. 1971; 134:713–740. [PubMed: 15776571]
19. Wong D, Li W, Chao JD, Zhou P, Narula G, Tsui C, Ko M, Xie J, Martinez-Frailes C, Av-Gay Y. Protein tyrosine kinase, PtkA, is required for *Mycobacterium tuberculosis* growth in macrophages. Sci Rep. 2018; 8
20. Mehta M, Rajmani RS, Singh A. *Mycobacterium tuberculosis* WhiB3 responds to vacuolar pH-induced changes in mycothiol redox potential to modulate phagosomal maturation and virulence. J Biol Chem. 2016; 291:2888–2903. [PubMed: 26637353]
21. Wong D, Bach H, Sun J, Hmama Z, Av-Gay Y. *Mycobacterium tuberculosis* protein tyrosine phosphatase (PtpA) excludes host vacuolar-H^+–ATPase to inhibit phagosome acidification. Proc Natl Acad Sci USA. 2011; 108:19371–19376. [PubMed: 22087003]
22. Queval CJ, Song O-R, Carralot J-P, Saliou J-M, Bongiovanni A, Deloison G, Deboosère N, Jouny S, Iantomasi R, Delorme V, Debrie A-S, et al. *Mycobacterium tuberculosis* controls phagosomal acidification by targeting CISH-mediated signaling. Cell Rep. 2017; 20:3188–3198. [PubMed: 28954234]
23. Cunningham TM, Koehl JL, Summers JS, Haydel SE. pH-dependent metal ion toxicity influences the antibacterial activity of two natural mineral mixtures. PLOS ONE. 2010; 5:e9456. [PubMed: 20209160]
24. Stohs SJ, Bagchi D. Oxidative mechanisms in the toxicity of metal ions. Free Radic Biol Med. 1995; 18:321–336. [PubMed: 7744317]
25. Nandakumar M, Nathan C, Rhee KY. Isocitrate lyase mediates broad antibiotic tolerance in *Mycobacterium tuberculosis*. Nat Commun. 2014; 5
26. Forte E, Borisov VB, Davletshin A, Mastronicola D, Sarti P, Giuffrè A. Cytochrome *bd* oxidase and hydrogen peroxide resistance in *Mycobacterium tuberculosis*. mBio. 2013; 4:e01006–13. [PubMed: 24345747]

27. Lu P, Heineke MH, Koul A, Andries K, Cook GM, Lill H, van Spanning R, Bald D. The cytochrome *bd*-type quinol oxidase is important for survival of *Mycobacterium smegmatis* under peroxide and antibiotic-induced stress. Sci Rep. 2015; 5
28. Wilks JC, Kitko RD, Cleeton SH, Lee GE, Ugwu CS, Jones BD, BonDurant SS, Slonczewski JL. Acid and base stress and transcriptomic responses in *Bacillus subtilis*. Appl Environ Microbiol. 2009; 75:981–990. [PubMed: 19114526]
29. Maurer LM, Yohannes E, Bondurant SS, Radmacher M, Slonczewski JL. pH regulates genes for flagellar motility, catabolism, and oxidative stress in *Escherichia coli* K-12. J Bacteriol. 2004; 187:304–319.
30. Vandal OH, Roberts JA, Odaira T, Schnappinger D, Nathan CF, Ehrt S. Acid-susceptible mutants of *Mycobacterium tuberculosis* share hypersusceptibility to cell wall and oxidative stress and to the host environment. J Bacteriol. 2009; 191:625–631. [PubMed: 19011036]
31. Newton GL, Buchmeier N, Fahey RC. Biosynthesis and functions of mycothiol, the unique protective thiol of *Actinobacteria*. Microbiol Mol Biol Rev. 2008; 72:471–494. [PubMed: 18772286]
32. Berney M, Berney-Meyer L, Wong K-W, Chen B, Chen M, Kim J, Wang J, Harris D, Parkhill J, Chan J, Wang F, et al. Essential roles of methionine and *S*-adenosylmethionine in the autarkic lifestyle of *Mycobacterium tuberculosis*. Proc Natl Acad Sci USA. 2015; 112:10008–10013. [PubMed: 26221021]
33. Wheeler PR, Coldham NG, Keating L, Gordon SV, Wooff EE, Parish T, Hewinson RG. Functional demonstration of reverse transsulfuration in the *Mycobacterium tuberculosis* complex reveals that methionine is the preferred sulfur source for pathogenic Mycobacteria. J Biol Chem. 2005; 280:8069–8078. [PubMed: 15576367]
34. Shatalin K, Shatalina E, Mironov A, Nudler E. H_2S: A universal defense against antibiotics in bacteria. Science. 2011; 334:986–990. [PubMed: 22096201]
35. Shukla P, Khodade VS, SharathChandra M, Chauhan P, Mishra S, Siddaramappa S, Pradeep BE, Singh A, Chakrapani H. "On demand" redox buffering by H_2S contributes to antibiotic resistance revealed by a bacteria-specific H_2S donor. Chem Sci. 2017; 8:4967–4972. [PubMed: 28959420]
36. Pal VK, Bandyopadhyay P, Singh A. Hydrogen sulfide in physiology and pathogenesis of bacteria and viruses. IUBMB Life. 2018; 70:393–410. [PubMed: 29601123]
37. Kohanski MA, Dwyer DJ, Hayete B, Lawrence CA, Collins JJ. A common mechanism of cellular death induced by bactericidal antibiotics. Cell. 2007; 130:797–810. [PubMed: 17803904]
38. Willemse D, Weber B, Masino L, Warren RM, Adinolfi S, Pastore A, Williams MJ. Rv1460, a SufR homologue, is a repressor of the suf operon in *Mycobacterium tuberculosis*. PLOS ONE. 2018; 13:e0200145. [PubMed: 29979728]
39. Huet G, Daffé M, Saves I. Identification of the *Mycobacterium tuberculosis* SUF machinery as the exclusive mycobacterial system of [Fe-S] cluster assembly: Evidence for its implication in the pathogen's survival. J Bacteriol. 2005; 187:6137–6146. [PubMed: 16109955]
40. Warrier T, Kapilashrami K, Argyrou A, Ioerger TR, Little D, Murphy KC, Nandakumar M, Park S, Gold B, Mi J, Zhang T, et al. N-methylation of a bactericidal compound as a resistance mechanism in *Mycobacterium tuberculosis*. Proc Natl Acad Sci USA. 2016; 113:E4523–E4530. [PubMed: 27432954]
41. Sukheja P, Kumar P, Mittal N, Li S-G, Singleton E, Russo R, Perryman AL, Shrestha R, Awasthi D, Husain S, Soteropoulos P, et al. A novel small-molecule inhibitor of the *Mycobacterium tuberculosis* demethylmenaquinone methyltransferase MenG is bactericidal to both growing and nutritionally deprived persister cells. MBio. 2017; 8:e02022–16.
42. Golby P, Nunez J, Cockle PJ, Ewer K, Logan K, Hogarth P, Vordermeier HM, Hinds J, Hewinson RG, Gordon SV. Characterization of two *in vivo*-expressed methyltransferases of the *Mycobacterium tuberculosis* complex: Antigenicity and genetic regulation. Microbiology. 2008; 154:1059–1067. [PubMed: 18375799]
43. Rodrigues L, Villellas C, Bailo R, Viveiros M, Ainsa JA. Role of the Mmr efflux pump in drug resistance in *Mycobacterium tuberculosis*. Antimicrob Agents Chemother. 2013; 57:751–757. [PubMed: 23165464]

44. Li G, Zhang J, Guo Q, Jiang Y, Wei J, Zhao L, Zhao X, Lu J, Wan K. Efflux pump gene expression in multidrug-resistant *Mycobacterium tuberculosis* clinical isolates. PLOS ONE. 2015; 10:e0119013. [PubMed: 25695504]
45. Ezraty B, Vergnes A, Banzhaf M, Duverger Y, Huguenot A, Brochado AR, Su S-Y, Espinosa L, Loiseau L, Py B, Typas A, et al. Fe-S cluster biosynthesis controls uptake of aminoglycosides in a ROS-less death pathway. Science. 2013; 340:1583–1587. [PubMed: 23812717]
46. Nambi S, Long JE, Mishra BB, Baker R, Murphy KC, Olive AJ, Nguyen HP, Shaffer SA, Sassetti CM. The oxidative stress network of *Mycobacterium tuberculosis* reveals coordination between radical detoxification systems. Cell Host Microbe. 2015; 17:829–837. [PubMed: 26067605]
47. Burian J, Ramón-García S, Sweet G, Gomez-Velasco A, Av-Gay Y, Thompson CJ. The mycobacterial transcriptional regulator *whiB7* gene links redox homeostasis and intrinsic antibiotic resistance. J Biol Chem. 2012; 287:299–310. [PubMed: 22069311]
48. Zhang J, Zhang Q. Using seahorse machine to measure OCR and ECAR in cancer cells. Methods Mol Biol. 2019; 1928:353–363. [PubMed: 30725464]
49. Hart PD, Young MR. Ammonium chloride, an inhibitor of phagosome-lysosome fusion in macrophages, concurrently induces phagosome-endosome fusion, and opens a novel pathway: Studies of a pathogenic mycobacterium and a nonpathogenic yeast. J Exp Med. 1991; 174:881–889. [PubMed: 1919441]
50. Rittig MG, Alvarez-Martinez MT, Porte F, Liautard J-P, Rouot B. Intracellular survival of *Brucella* spp. in human monocytes involves conventional uptake but special phagosomes. Infect Immun. 2001; 69:3995–4006. [PubMed: 11349069]
51. Matt U, Selchow P, Dal Molin M, Strommer S, Sharif O, Schilcher K, Andreoni F, Stenzinger A, Zinkernagel AS, Zeitlinger M, Sander P, et al. Chloroquine enhances the antimycobacterial activity of isoniazid and pyrazinamide by reversing inflammation-induced macrophage efflux. Int J Antimicrob Agents. 2017; 50:55–62. [PubMed: 28506804]
52. Mwandumba HC, Russell DG, Nyirenda MH, Anderson J, White SA, Molyneux ME, Squire SB. *Mycobacterium tuberculosis* resides in nonacidified vacuoles in endocytically competent alveolar macrophages from patients with tuberculosis and HIV infection. J Immunol. 2004; 172:4592–4598. [PubMed: 15034077]
53. Ali SA, Mavundla TR, Fantu R, Awoke T. Outcomes of TB treatment in HIV co-infected TB patients in Ethiopia: A cross-sectional analytic study. BMC Infect Dis. 2016; 16:640. [PubMed: 27814693]
54. Bhaskar A, Munshi MH, Khan SZ, Fatima S, Arya R, Jameel S, Singh A. Measuring glutathione redox potential of HIV-1-infected macrophages. J Biol Chem. 2015; 290:1020–1038. [PubMed: 25406321]
55. Folks TM, Justement J, Kinter A, Dinarello CA, Fauci AS. Cytokine-induced expression of HIV-1 in a chronically infected promonocyte cell line. Science. 1987; 238:800–802. [PubMed: 3313729]
56. Poli G, Kinter A, Justement JS, Kehrl JH, Bressler P, Stanley S, Fauci AS. Tumor necrosis factor alpha functions in an autocrine manner in the induction of human immunodeficiency virus expression. Proc Natl Acad Sci USA. 1990; 87:782–785. [PubMed: 2300561]
57. Cohen NR, Lobritz MA, Collins JJ. Microbial persistence and the road to drug resistance. Cell Host Microbe. 2013; 13:632–642. [PubMed: 23768488]
58. Gill WP, Harik NS, Whiddon MR, Liao RP, Mittler JE, Sherman DR. A replication clock for *Mycobacterium tuberculosis*. Nat Med. 2009; 15:211–214. [PubMed: 19182798]
59. Kramer CE, Singh A, Helfrich S, Grunberger A, Wiechert W, Noh K, Kohlheyer D. Non-invasive microbial metabolic activity sensing at single cell level by perfusion of calcein acetoxymethyl ester. PLOS ONE. 2015; 10:e0141768. [PubMed: 26513257]
60. de Steenwinkel JEM, deKnegt GJ, Ten Kate MT, van Belkum A, Verbrugh HA, Kremer K, van Soolingen D, Bakker-Woudenberg IAJM. Time-kill kinetics of anti-tuberculosis drugs, and emergence of resistance, in relation to metabolic activity of *Mycobacterium tuberculosis*. J Antimicrob Chemother. 2010; 65:2582–2589. [PubMed: 20947621]
61. Danilchanka O, Mailaender C, Niederweis M. Identification of a novel multidrug efflux pump of *Mycobacterium tuberculosis*. Antimicrob Agents Chemother. 2008; 52:2503–2511. [PubMed: 18458127]

62. Farhana A, Kumar S, Rathore SS, Ghosh PC, Ehtesham NZ, Tyagi AK, Hasnain SE. Mechanistic insights into a novel exporter-importer system of *Mycobacterium tuberculosis* unravel its role in trafficking of iron. PLOS ONE. 2008; 3:e2087. [PubMed: 18461140]

63. De Rossi E, Branzoni M, Cantoni R, Milano A, Riccardi G, Ciferri O. *mmr*, a *Mycobacterium tuberculosis* gene conferring resistance to small cationic dyes and inhibitors. J Bacteriol. 1998; 180:6068–6071. [PubMed: 9811672]

64. Wolschendorf FA, Ackart D, Shrestha TB, Hascall-Dove L, Nolan S, Lamichhane G, Wang Y, Bossmann SH, Basaraba RJ, Niederweis M. Copper resistance is essential for virulence in *Mycobacterium tuberculosis*. Proc Natl Acad Sci USA. 2011; 108:1621–1626. [PubMed: 21205886]

65. Chawla M, Mishra S, Anand K, Parikh P, Mehta M, Vij M, Verma T, Singh P, Jakkala K, Verma HN, Ajitkumar P, et al. Redox-dependent condensation of the mycobacterial nucleoid by WhiB4. Redox Biol. 2018; 19:116–133. [PubMed: 30149290]

66. Hart PD, Young MR, Gordon AH, Sullivan KH. Inhibition of phagosome-lysosome fusion in macrophages by certain mycobacteria can be explained by inhibition of lysosomal movements observed after phagocytosis. J Exp Med. 1987; 166:933–946. [PubMed: 3309128]

67. Poole B, Ohkuma S. Effect of weak bases on the intralysosomal pH in mouse peritoneal macrophages. J Cell Biol. 1981; 90:665–669. [PubMed: 6169733]

68. Dhar N, McKinney JD. *Mycobacterium tuberculosis* persistence mutants identified by screening in isoniazid-treated mice. Proc Natl Acad Sci USA. 2010; 107:12275–12280. [PubMed: 20566858]

69. Via LE, Lin PL, Ray SM, Carrillo J, Allen SS, Eum SY, Taylor K, Klein E, Manjunatha U, Gonzales J, Lee EG, et al. Tuberculous granulomas are hypoxic in guinea pigs, rabbits, and nonhuman primates. Infect Immun. 2008; 76:2333–2340. [PubMed: 18347040]

70. Crowle AJ, May MH. Inhibition of tubercle bacilli in cultured human macrophages by chloroquine used alone and in combination with streptomycin, isoniazid, pyrazinamide, and two metabolites of vitamin D3. Antimicrob Agents Chemother. 1990; 34:2217–2222. [PubMed: 2127346]

71. Ganguli A, Choudhury D, Datta S, Bhattacharya S, Chakrabarti G. Inhibition of autophagy by chloroquine potentiates synergistically anti-cancer property of artemisinin by promoting ROS dependent apoptosis. Biochimie. 2014; 107(Pt B):338–349. [PubMed: 25308836]

72. Lee J, Repasy T, Papavinasasundaram K, Sassetti C, Kornfeld H. *Mycobacterium tuberculosis* induces an atypical cell death mode to escape from infected macrophages. PLOS ONE. 2011; 6:e18367. [PubMed: 21483832]

73. Levitte S, Adams KN, Berg RD, Cosma CL, Urdahl KB, Ramakrishnan L. Mycobacterial acid tolerance enables phagolysosomal survival and establishment of tuberculous infection in vivo. Cell Host Microbe. 2016; 20:250–258. [PubMed: 27512905]

74. Gustafsson LL, Walker O, Alvan G, Beermann B, Estevez F, Gleisner L, Lindstrom B, Sjoqvist F. Disposition of chloroquine in man after single intravenous and oral doses. Br J Clin Pharmacol. 1983; 15:471–479. [PubMed: 6849784]

75. Chow SC. Bioavailability and bioequivalence in drug development. Wiley Interdiscip Rev Comput Stat. 2014; 6:304–312. [PubMed: 25215170]

76. Nwankwo JO, Garba MA, Chinje CE, Mgbojikwe LO, Emerole GO. Possible chloroquine-induced modification of N-acetylation of isoniazid and sulphadimidine in the rat. Biochem Pharmacol. 1990; 40:654–659. [PubMed: 2383293]

77. Akira M, Sakatani M, Ishikawa H. Transient radiographic progression during initial treatment of pulmonary tuberculosis: CT findings. J Comput Assist Tomogr. 2000; 24:426–431. [PubMed: 10864081]

78. Jindani A, Dore CJ, Mitchison DA. Bactericidal and sterilizing activities of antituberculosis drugs during the first 14 days. Am J Respir Crit Care Med. 2003; 167:1348–1354. [PubMed: 12519740]

79. Kim JJ, Lee HM, Shin DM, Kim W, Yuk JM, Jin HS, Lee SH, Cha GH, Kim JM, Lee ZW, Shin SJ, et al. Host cell autophagy activated by antibiotics is required for their effective antimycobacterial drug action. Cell Host Microbe. 2012; 11:457–468. [PubMed: 22607799]

80. Coulson GB, Johnson BK, Zheng H, Colvin CJ, Fillinger R, Haiderer ER, Hammer ND, Abramovitch RB. Targeting *Mycobacterium tuberculosis* sensitivity to thiol stress at acidic pH

Europe PMC Funders Author Manuscripts

kills the bacterium and potentiates antibiotics. Cell Chem Biol. 2017; 24:993–1004.e4. [PubMed: 28781126]

81. Vaubourgeix J, Lin G, Dhar N, Chenouard N, Jiang X, Botella H, Lupoli T, Mariani O, Yang G, Ouerfelli O, Unser M, et al. Stressed mycobacteria use the chaperone ClpB to sequester irreversibly oxidized proteins asymmetrically within and between cells. Cell Host Microbe. 2015; 17:178–190. [PubMed: 25620549]
82. Vandal OH, Pierini LM, Schnappinger D, Nathan CF, Ehrt S. A membrane protein preserves intrabacterial pH in intraphagosomal *Mycobacterium tuberculosis*. Nat Med. 2008; 14:849–854. [PubMed: 18641659]
83. Baker JJ, Johnson BK, Abramovitch RB. Slow growth of *Mycobacterium tuberculosis* at acidic pH is regulated by *phoPR* and host-associated carbon sources. Mol Microbiol. 2014; 94:56–69. [PubMed: 24975990]
84. Burton NA, Schurmann N, Casse O, Steeb AK, Claudi B, Zankl J, Schmidt A, Burmann D. Disparate impact of oxidative host defenses determines the fate of *Salmonella* during systemic infection in mice. Cell Host Microbe. 2014; 15:72–83. [PubMed: 24439899]
85. Avican K, Fahlgren A, Huss M, Heroven AK, Beckstette M, Dersch P, Fallman M. Reprogramming of *Yersinia* from virulent to persistent mode revealed by complex in vivo RNA-seq analysis. PLOS Pathog. 2015; 11:e1004600. [PubMed: 25590628]
86. Vilcheze C, Hartman T, Weinrick B, Jain P, Weisbrod TR, Leung LW, Freundlich JS, Jacobs WR Jr. Enhanced respiration prevents drug tolerance and drug resistance in *Mycobacterium tuberculosis*. Proc Natl Acad Sci USA. 2017; 114:4495–4500. [PubMed: 28396391]
87. Tsai WP, Nara PL, Kung HF, Oroszlan S. Inhibition of human immunodeficiency virus infectivity by chloroquine. AIDS Res Hum Retroviruses. 1990; 6:481–489. [PubMed: 1692728]
88. Martins D, McKay G, Sampathkumar G, Khakimova M, English AM, Nguyen D. Superoxide dismutase activity confers (p)ppGpp-mediated antibiotic tolerance to stationary-phase *Pseudomonas aeruginosa*. Proc Natl Acad Sci USA. 2018; 115:9797–9802. [PubMed: 30201715]
89. McCune RM Jr, Tompsett R. Fate of *Mycobacterium tuberculosis* in mouse tissues as determined by the microbial enumeration technique. I. The persistence of drug-susceotible tubercle bacilli in the tissues despite prolonged anitmicrobial therapy. J Exp Med. 1956; 104:737–762. [PubMed: 13367341]
90. McAulay K, Saito K, Warrier T, Walsh KF, Mathurin LD, Royal-Mardi G, Lee MH, Ocheretina O, Pape JW, Fitzgerald DW, Nathan CF. Differentially detectable *Mycobacterium tuberculosis* cells in sputum from treatment-naïve subjects in Haitian and their proportionate increase after initiation of treatment. MBio. 2018; 9:e02192–18. [PubMed: 30459198]
91. Jain R, Dey B, Dhar N, Rao V, Singh R, Gupta UD, Katoch VM, Ramanathan VD, Tyagi AK. Enhanced and enduring protection against tuberculosis by recombinant BCG-Ag85C and its association with modulation of cytokine profile in lung. PLOS ONE. 2008; 3:e3869. [PubMed: 19052643]
92. Ahmad Z, Klinkenberg LG, Pinn ML, Fraig MM, Peloquin CA, Bishai WR, Nuermberger EL, Grosset JH, Karakousis PC. Biphasic kill curve of isoniazid reveals the presence of drug-tolerant, not drug-resistant, *Mycobacterium tuberculosis* in the guinea pig. J Infect Dis. 2009; 200:1136–1143. [PubMed: 19686043]
93. Glass K, Girvan M. Annotation enrichment analysis: An alternative method for evaluating the functional properties of gene sets. Sci Rep. 2014; 4
94. Ghorpade DS, Holla S, Kaveri SV, Bayry J, Patil SA, Balaji KN. Sonic hedgehog-dependent induction of microRNA 31 and microRNA 150 regulates *Mycobacterium bovis* BCG-driven toll-like receptor 2 signaling. Mol Cell Biol. 2013; 33:543–556. [PubMed: 23166298]
95. Arcila ML, Sánchez MD, Ortiz B, Barrera LF, Garcia LF, Rojas M. Activation of apoptosis, but not necrosis, during *Mycobacterium tuberculosis* infection correlated with decreased bacterial growth: Role of TNF-α, IL-10, caspases and phospholipase A2. Cell Immunol. 2007; 249:80–93. [PubMed: 18160064]
96. Chawla M, Parikh P, Saxena A, Munshi MH, Mehta M, Mai D, Srivastava AK, Narasimhulu KV, Redding KE, Vashi N, Kumar D, et al. *Mycobacterium tuberculosis* WhiB4 regulates oxidative

stress response to modulate survival and dissemination in vivo. Mol Microbiol. 2012; 85:1148–1165. [PubMed: 22780904]

97. Li H, Durbin R. Fast and accurate short read alignment with Burrows-Wheeler transform. Bioinformatics. 2009; 25:1754–1760. [PubMed: 19451168]
98. Li H, Handsaker B, Wysoker A, Fennell T, Ruan J, Homer N, Marth G, Abecasis G, Durbin R, 1000 Genome Project Data Processing Subgroup. The Sequence Alignment/Map format and SAMtools. Bioinformatics. 2009; 25:2078–2079. [PubMed: 19505943]
99. Quinlan AR, Hall IM. BEDTools: A flexible suite of utilities for comparing genomic features. Bioinformatics. 2010; 26:841–842. [PubMed: 20110278]
100. Love MI, Huber W, Anders S. Moderated estimation of fold change and dispersion for RNA-seq data with DESeq2. Genome Biol. 2014; 15:550. [PubMed: 25516281]
101. Colangeli R, Helb D, Sridharan S, Sun J, Varma-Basil M, Hazbon MH, Harbacheuski R, Megjugorac NJ, Jacobs WR Jr, Holzenburg A, Sacchettini J, et al. The *Mycobacterium tuberculosis iniA* gene is essential for activity of an efflux pump that confers drug tolerance to both isoniazid and ethambutol. Mol Microbiol. 2005; 55:1829–1840. [PubMed: 15752203]
102. Andrews S. FastQC: A quality control tool for highthroughput sequence data. 2010
103. RStudio Team. RStudio: Integrated development for R. RStudio, Inc; Boston, MA: 2015. www.rstudio.com/
104. Basic A, Blomqvist S, Carlen A, Dahlén G. Estimation of bacterial hydrogen sulfide production in vitro. J Oral Microbiol. 2015; 7
105. Lamprecht DA, Finin PM, Rahman MA, Cummin BM, Russell SL, Jonnala SR, Adamson JH, Steyn AJCS. Turning the respiratory flexibility of *Mycobacterium tuberculosis* against itself. Nat Commun. 2016; 7
106. Mishra S, Shukla P, Bhaskar A, Anand K, Baloni P, Jha RK, Mohan A, Rajmani RS, Nagaraja V, Chandra N, Singh A. Efficacy of β-lactam/β-lactamase inhibitor combination is linked to WhiB4-mediated changes in redox physiology of *Mycobacterium tuberculosis*. eLife. 2017; 6:e25624. [PubMed: 28548640]
107. Hendon-Dunn CL, Doris KS, Thomas SR, Allnutt JC, Marriott AAN, Hatch KA, Watson RJ, Bottley G, Marsh PD, Taylor SC, Bacon J. A flow cytometry method for rapidly assessing *Mycobacterium tuberculosis* responses to antibiotics with different modes of action. Antimicrob Agents Chemother. 2016; 60:3869–3883. [PubMed: 26902767]
108. Jungblut M, Oeltze K, Zehnter I, Hasselmann D, Bosio A. Standardized preparation of single-cell suspensions from mouse lung tissue using the gentleMACS Dissociator. J Vis Exp. 2009; 29:1266.
109. Chakarov S, Lim HY, Tan L, Lim SY, See P, Lum J, Zhang X-M, Foo S, Nakamizo S, Duan K, Kong WT, et al. Two distinct interstitial macrophage populations coexist across tissues in specific subtissular niches. Science. 2019; 363
110. Grosset J, Truffot-Pernot C, Lacroix C, Ji B. Antagonism between isoniazid and the combination pyrazinamide-rifampin against tuberculosis infection in mice. Antimicrob Agents Chemother. 1992; 36:548–551. [PubMed: 1622164]
111. Dutta NK, Pinn ML, Karakousis PC. Reduced emergence of isoniazid resistance with concurrent use of thioridazine against acute murine tuberculosis. Antimicrob Agents Chemother. 2014; 58:4048–4053. [PubMed: 24798290]
112. Abramovitch RB, Rohde KH, Hsu F-F, Russell DG. *aprABC*: A *Mycobacterium tuberculosis* complex-specific locus that modulates pH-driven adaptation to the macrophage phagosome. Mol Microbiol. 2011; 80:678–694. [PubMed: 21401735]

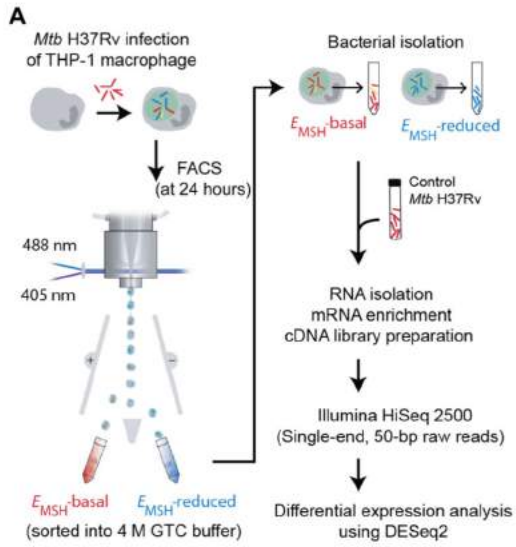

C

Stimulus	Reference list size	Overlap with E_{MSH}-reduced		Overlap with E_{MSH}-basal	
		Genes	Significance	Genes	Significance
Macrophage residence 24 hours (up)[1]	254	53	2.98×10^{-8}	55	6.98×10^{-10}
Macrophage residence 24 hours (down)[1]	109	12	2.97×10^{-3}	25	6.26×10^{-9}
Acidic stress pH 5.5 (up)[1]	249	36	1.05×10^{-2}	21	ns
Acidic stress pH 5.5 (down)[1]	364	29	1.86×10^{-3}	35	8.63×10^{-3}
Acidic stress pH 4.5 (up)[2]	473	99	1.50×10^{-15}	51	ns
Acidic stress pH 4.5 (down)[2]	458	45	1.78×10^{-7}	38	ns

[1]Rohde *et al. (17)* [2]Mehta *et al. (20)*

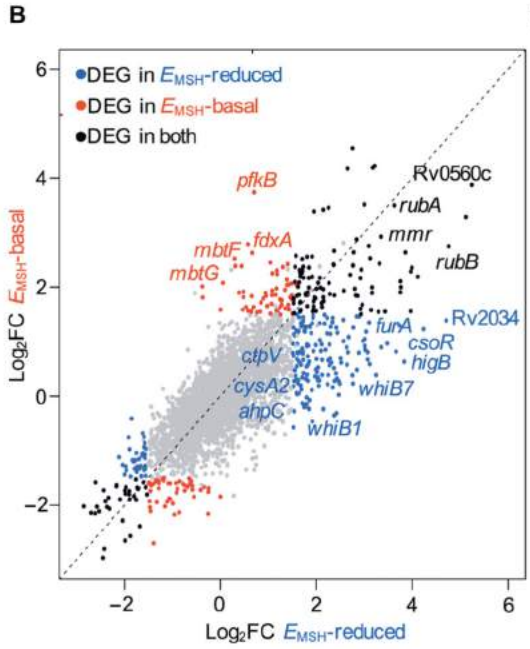

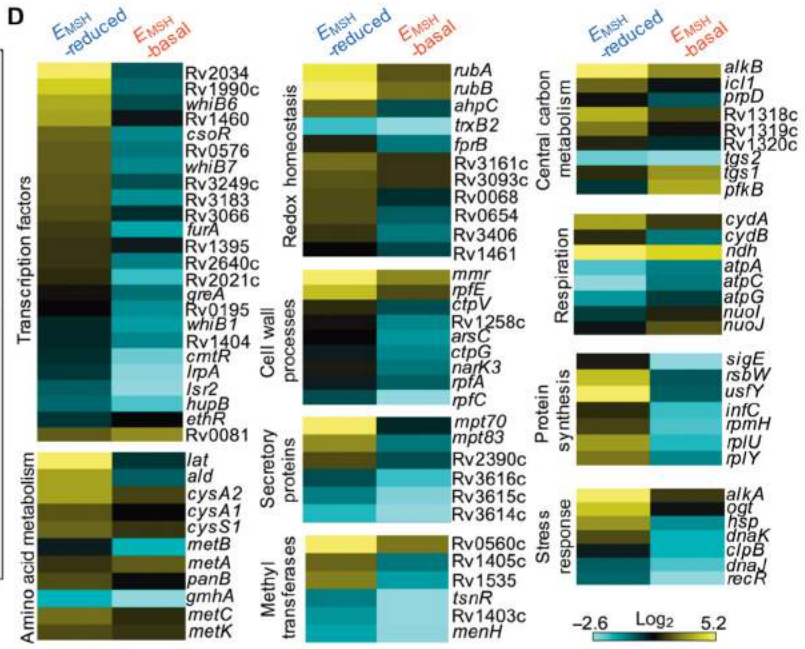

Fig. 1. RNA-seq of intraphagosomal *Mtb* derived from E_{MSH}-reduced and E_{MSH}-basal fractions.

(**A**) Schematic depiction of flow sorting–coupled RNA-seq of intraphagosomal bacteria present in E_{MSH}-basal and E_{MSH}-reduced fractions of THP-1 macrophages infected with *Mtb*/Mrx1-roGFP2. *Mtb* cells (optical density at 600 nm, 0.4) harvested and resuspended in RPMI for 24 hours were used as an in vitro control. FACS, fluorescence-activated cell sorting; GTC, guanidinium thiocyanate. (**B**) Scatter plot indicates relative distribution of differentially expressed genes (DEGs) from the E_{MSH}-reduced and E_{MSH}-basal fractions on the basis of $\log_2$ fold changes (FC) (blue, DEGs specific to E_{MSH}-reduced; red, DEGs unique to E_{MSH}-basal; black, DEGs common to both; gray, nonsignificant genes). (**C**) The table summarizes the transcriptional overlap between this study and the response of *Mtb* under intramacrophage and pH stress conditions. Fisher's exact test with $P < 0.05$ as a cutoff

for significance. ns, no significant difference. (**D**) Heat maps indicate $\log_2$ fold changes of DEGs belonging to various functional categories (obtained from Mycobrowser, École polytechnique fédérale de Lausanne) in E_{MSH}-reduced and E_{MSH}-basal fractions. Genes were considered differentially expressed on the basis of the false discovery rate (FDR) of ≤0.05 and absolute fold change of ≥1.5 (tables S1 and S3).

Europe PMC Funders Author Manuscripts

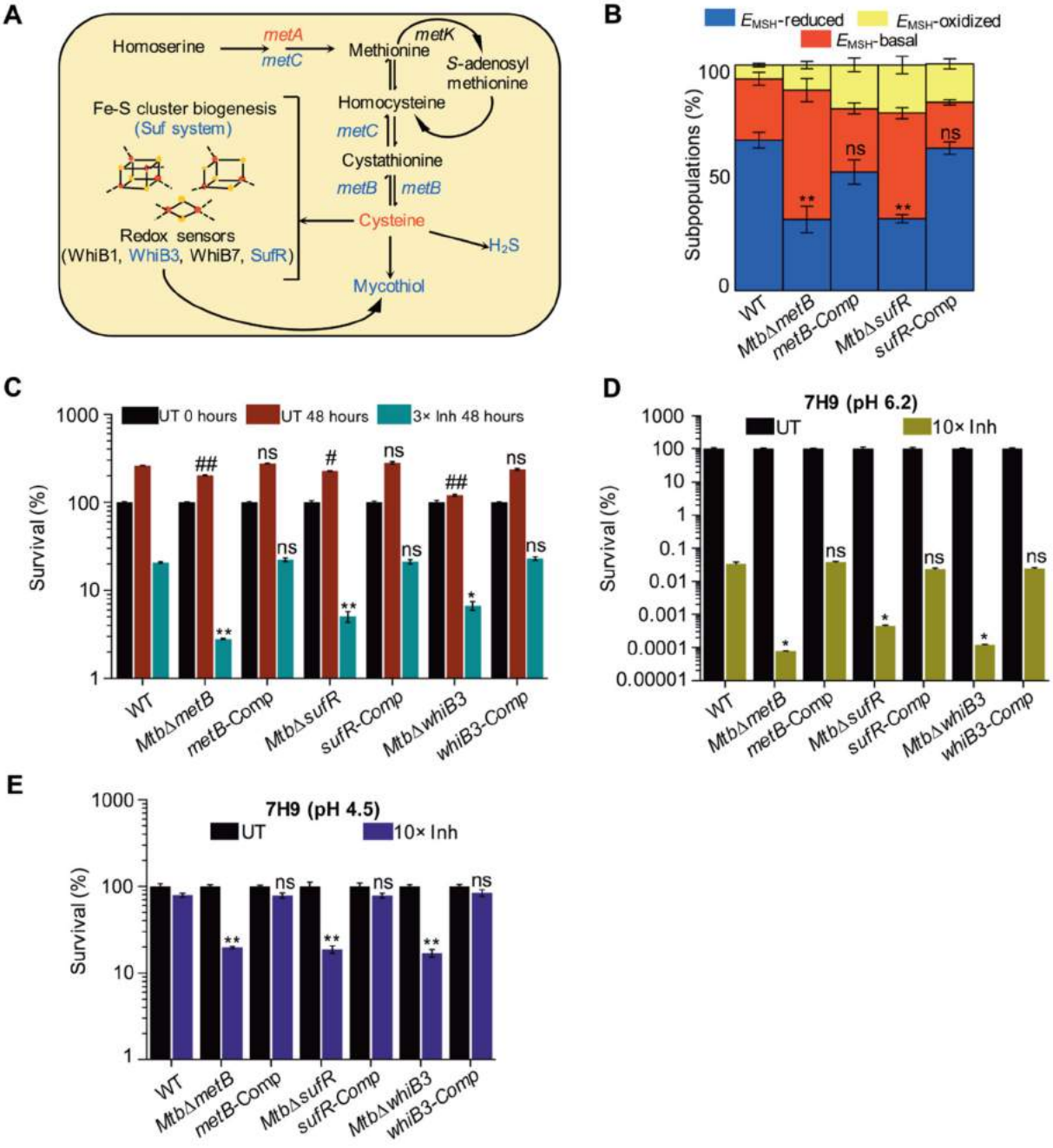

Fig. 2. Cysteine utilization pathways promote redox heterogeneity and drug tolerance in *Mtb*.

(**A**) Various cysteine (CySH) utilization pathways in *Mtb*. Expression of genes (blue) coordinating CySH flux into pathways for mycothiol (MSH), Fe-S cluster, and H_2S biogenesis is induced in the E_{MSH}-reduced fraction. (**B**) THP-1 macrophages were infected for 24 hours with the indicated strains of *Mtb* expressing Mrx1-roGFP2, and the percent distribution of redox-diverse fractions was measured at 24 hours p.i. and depicted as a stacked bar plot. $^{**}P < 0.01$, by Mann-Whitney test compares E_{MSH}-reduced fraction in various strains of *Mtb* with WT *Mtb*. (**C**) THP-1 macrophages infected for 24 hours with the

Europe PMC Funders Author Manuscripts

indicated strains of *Mtb* were exposed for an additional 48 hours to Inh (2.18 μM, 3× of in vitro MIC) or left untreated. Bacillary load was determined by CFU enumeration, and percent survival was quantified by normalizing the CFU in Inh-treated samples at 48 hours against untreated samples (UT) at 0 hours. *$P < 0.05$, **$P < 0.01$, #$P < 0.05$, and ##$P < 0.01$, by Mann-Whitney test. Number signs (#) and asterisks (*) compare survival between WT *Mtb* and other strains under UT and Inh-treated conditions, respectively. (**D** and **E**) Indicated strains of *Mtb* grown in 7H9-tyloxapol broth acidified to pH 6.2 or pH 4.5 were exposed to Inh (7.25 μM, 10× of in vitro MIC) or kept unexposed. Bacterial load was quantified after 5 days of treatment by CFU enumeration, and percent survival was quantified strain-wise by normalizing the bacterial load in Inh-treated samples at day 5 against untreated samples. *$P < 0.05$, **$P < 0.001$, by Mann-Whitney test. Asterisks compare survival between WT *Mtb* and other strains after 5 days of Inh treatment. Data shown in each panel are the results of three independent experiments performed in triplicate (means ± SD). ns, no significant difference ($P > 0.05$).

Europe PMC Funders Author Manuscripts

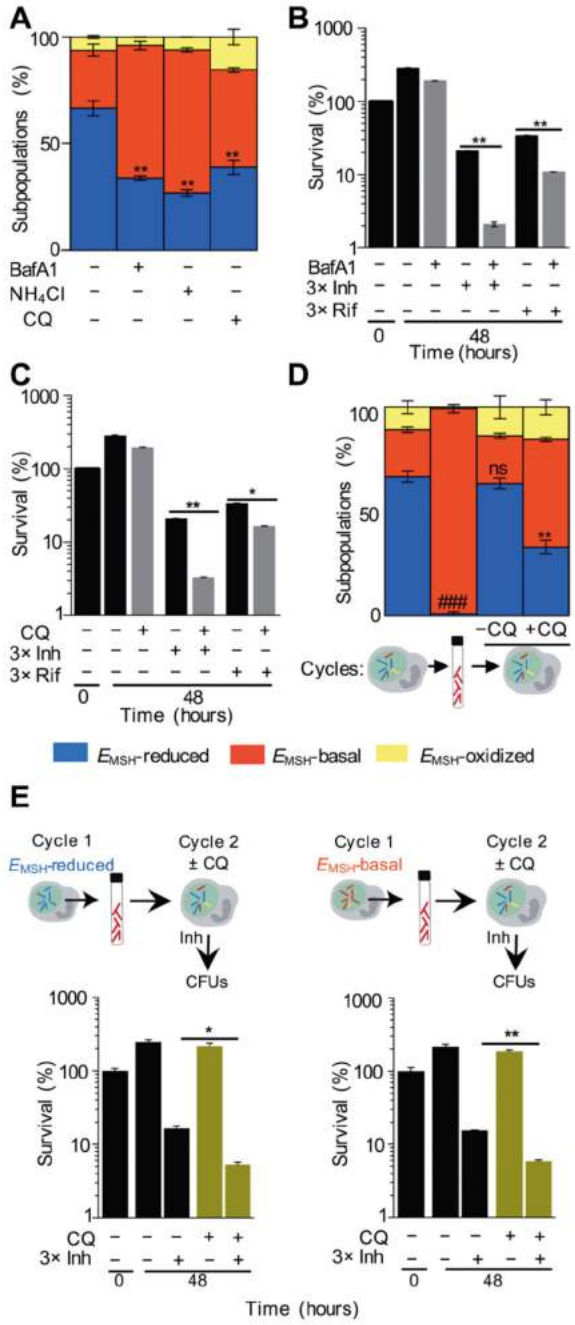

Fig. 3. Phagosomal pH is required for the redox-dependent multidrug tolerance of *Mtb*.

(**A**) THP-1 macrophages—untreated or pretreated with 10 nM BafA1, 10 mM NH_4Cl, or 10 μM CQ—were infected with *Mtb*/Mrx1-roGFP2, and percent distribution of redox-diverse fractions was measured at 24 hours p.i. $^{**}P < 0.01$, by Mann-Whitney test to compare the E_{MSH}-reduced fraction with untreated sample. (**B** and **C**) THP-1 macrophages, untreated or pretreated with 10 nM BafA1 or 10 μM CQ, were infected with WT *Mtb* for 24 hours and exposed to Inh (2.18 μM) or Rif (1 μM) or left unexposed for an additional 48 hours. Percent survival was quantified by normalizing the CFU in drug-treated samples at 48 hours against

untreated samples at 0 hours. *$P < 0.05$, **$P < 0.01$, by Mann-Whitney test. (**D**) THP-1 macrophages were infected with *Mtb*/Mrx1-roGFP2, and E_{MSH} was measured at 24 hours p.i. After this, intraphagosomal bacteria were released and incubated in 7H9-albumen-dextrose-sodium chloride for 2 hours, and E_{MSH} was determined. The 7H9-ADS–adapted *Mtb* was used to reinfect fresh THP-1 macrophages, with or without pretreatment with 10 μM CQ, and E_{MSH} was measured at 24 hours p.i. **$P < 0.01$, ###$P < 0.001$, by Mann-Whitney test. Number signs (#) compare E_{MSH}-reduced fractions between intramacrophage and 7H9-ADS–adapted *Mtb*. Asterisks (*) compare E_{MSH}-reduced fractions between untreated and CQ-treated samples. (**E**) THP-1 macrophages harboring E_{MSH}-reduced and E_{MSH}-basal bacteria were flow-sorted at 24 hours p.i. (cycle 1 infection), and bacteria were released into 7H9-ADS. At 24-hour incubation, 7H9-ADS–adapted *Mtb* were used to infect THP-1 macrophages, with or without pretreatment with 10 μM CQ, for 24 hours (cycle 2 infection), and Inh tolerance was determined as mentioned earlier. *$P < 0.05$, **$P < 0.01$, by Mann-Whitney test. Data shown in each panel are the results of three independent experiments performed in triplicate (means ± SD). ns, no significant difference ($P > 0.05$).

Europe PMC Funders Author Manuscripts

Europe PMC Funders Author Manuscripts

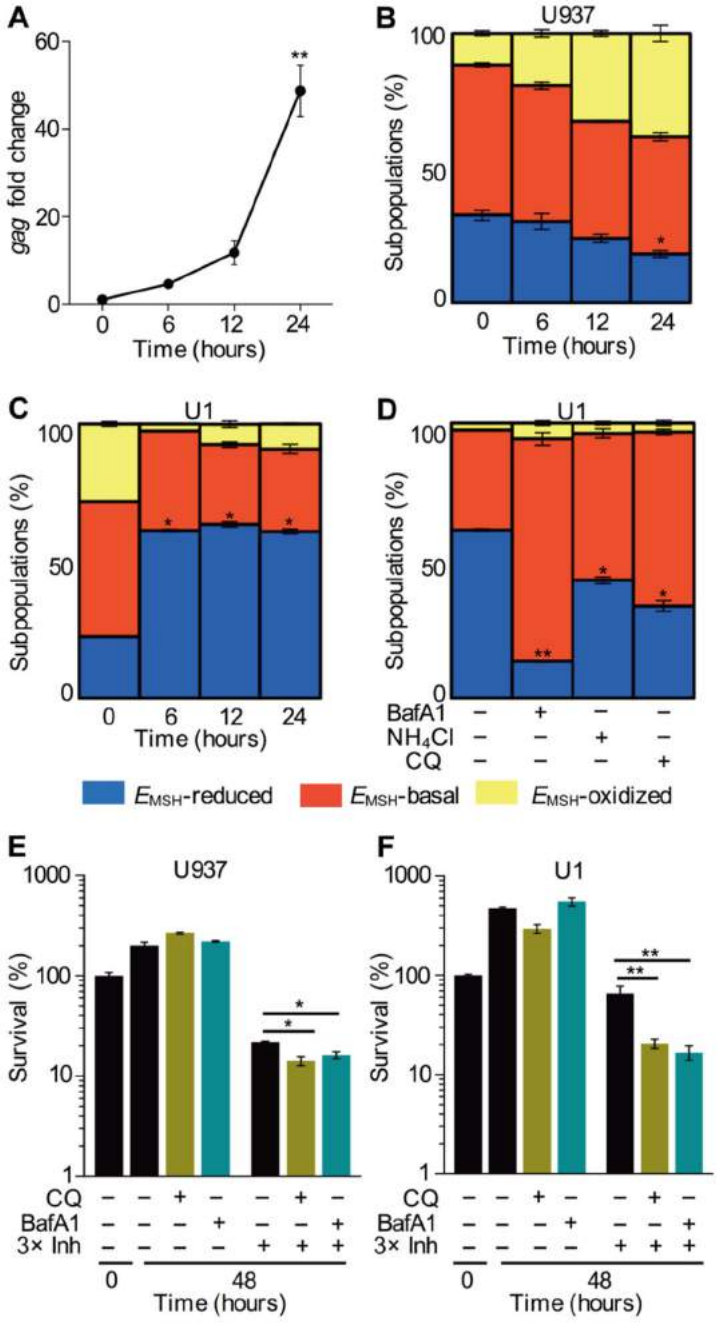

Fig. 4. Phagosomal pH and redox heterogeneity drive drug tolerance during HIV-TB coinfection.

(**A**) The course of HIV-1 replication upon stimulation of the U1 promonocytic cell line with PMA (5 ng/ml). Viral load was monitored by *gag* qRT-PCR. $^{**}P < 0.01$, by Mann-Whitney test comparing *gag* expression with 0 hours. U937 (uninfected HIV-1 control) (**B**) and U1 macrophages (**C**) were stimulated with PMA and infected with *Mtb*/Mrx1-roGFP2, and percent distribution of redox-diverse fractions was measured over time. $^{*}P < 0.05$, by Mann-Whitney test. Asterisks (*) compare E_{MSH}-reduced fraction at various time points with 0 hours. (**D**) U1 macrophages—untreated or pretreated with 10 nM BafA1, 10 mM NH_4Cl,

and 10 μM CQ—were infected with *Mtb*/Mrx1-roGFP2, and percent distribution of redox-diverse fractions was measured at 12 hours p.i. *$P < 0.05$, **$P < 0.01$, by Mann-Whitney test. Asterisks (*) compare E_{MSH}-reduced fractions between untreated and BafA1/NH_4Cl/CQ-treated samples. U937 (**E**) and U1 macrophages (**F**), untreated or pretreated with 10 μM CQ or 10 nM BafA1, were infected with WT *Mtb* for 12 hours and exposed to Inh (2.18 μM) or left unexposed for an additional 48 hours. Bacillary load was determined by CFU enumeration, and percent survival was quantified by normalizing the CFU in drug-treated samples at 48 hours against untreated samples at 0 hours. *$P < 0.05$, **$P < 0.01$, by Mann-Whitney test. Data shown in each panel are the results of three independent experiments performed in triplicate (means ± SD).

Europe PMC Funders Author Manuscripts

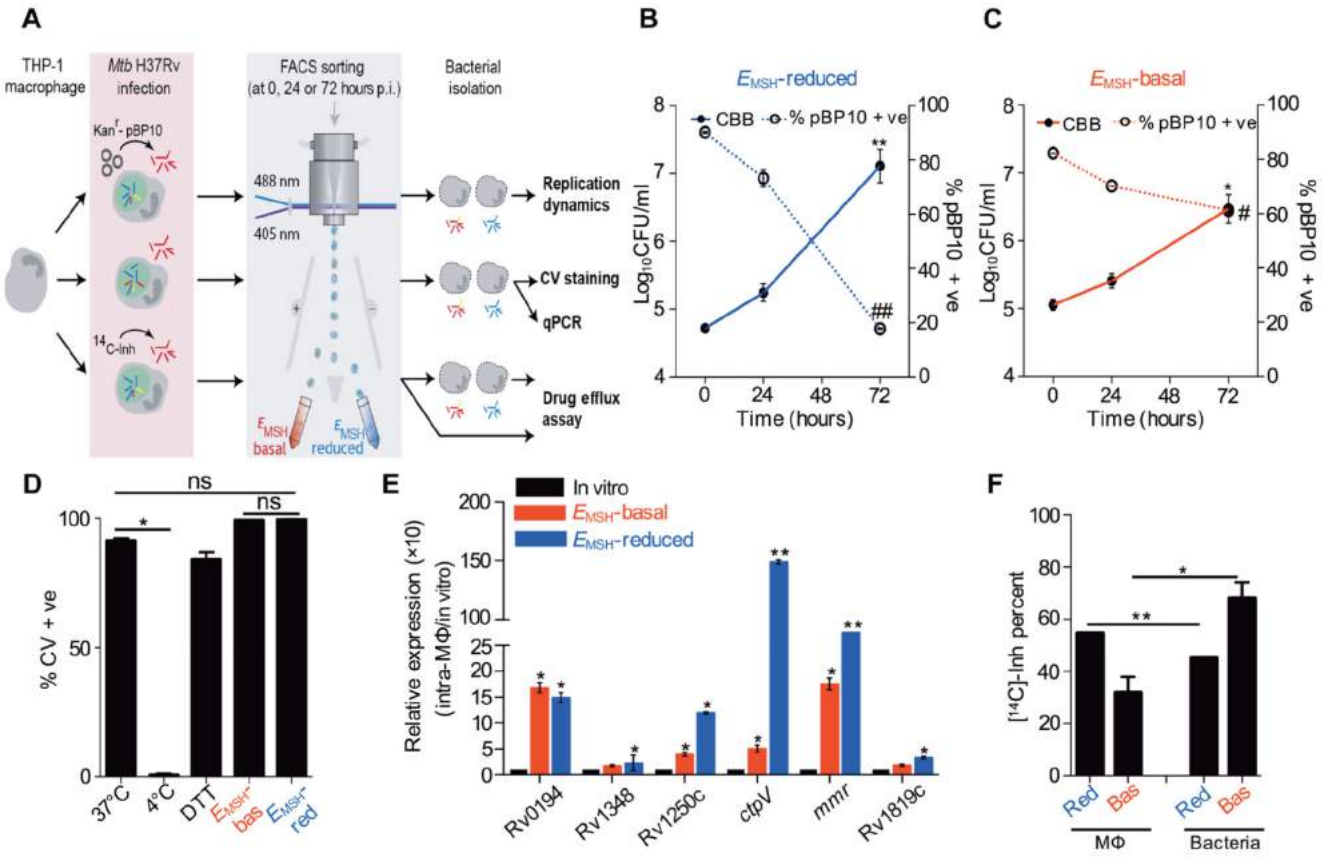

Fig. 5. The drug-tolerant E_{MSH}-reduced population is replicative and has high efflux pump activity.

(**A**) Graphical depiction of Mrx1-roGFP2–coupled flow-sorting strategy to determine replication dynamics, metabolic state, and drug efflux activity in intramacrophage E_{MSH}-reduced and E_{MSH}-basal populations. (**B** and **C**) THP-1 macrophages were infected with pBP10-containing *Mtb*/Mrx1-roGFP2. At indicated time points, macrophages harboring E_{MSH}-reduced and E_{MSH}-basal bacteria were flow-sorted, and bacteria were released and plated in the presence or absence of kanamycin (Kan). The frequency of pBP10 loss and increase in cumulative bacterial burden (CBB) were calculated. $*P < 0.05$, $**P < 0.01$, $\#P < 0.05$, $\#\#P < 0.01$, by Kruskal-Wallis test with Dunn's correction over time p.i. Asterisks (*) and number signs (#) compare CFU per milliliter and percentage of pBP10 + ve bacteria over time p.i., respectively. (**D**) THP-1 macrophages were infected with *Mtb*/Mrx1-roGFP2, and at 24 hours p.i., the redox state of intraphagosomal *Mtb*/Mrx1-roGFP2 thiols was fixed using *N*-ethylmaleimide. Bacteria were released from macrophages and stained with calcein violet–AM (CV-AM). The CV-AM staining and E_{MSH} status of *Mtb* cells were determined using multiparameter flow cytometric analysis. As a control, we performed CV-AM staining of *Mtb* grown in 7H9 broth for 24 hours at 4° and 37°C. $*P < 0.05$, by Mann-Whitney test. (**E**) THP-1 macrophages harboring E_{MSH}-reduced and E_{MSH}-basal bacteria were flow-sorted at 24 hours p.i., bacterial RNA was isolated, and expression of efflux pumps was measured by qRT-PCR. Expression was compared with in vitro control *Mtb*, and fold change was quantified after normalizing by 16*S* ribosomal RNA. $*P < 0.05$, $**P < 0.01$, by Mann-

Europe PMC Funders Author Manuscripts

Whitney test for comparison with in vitro control *Mtb*. (**F**) THP-1 macrophages were infected with *Mtb*/Mrx1-roGFP2 bacteria preloaded with [^{14}C]-Inh. At 24 hours p.i., macrophages harboring E_{MSH}-reduced (Red) and E_{MSH}-basal (Bas) bacteria were sorted and bacteria released. The relative distribution of radioactive [^{14}C]-Inh was measured in bacterial and macrophage (MΦ) fractions. *$P < 0.05$, **$P < 0.01$, by Mann-Whitney test. Data shown in each panel are the results of two independent experiments performed in triplicate (means ± SD). ns, no significant difference ($P > 0.05$).

Europe PMC Funders Author Manuscripts

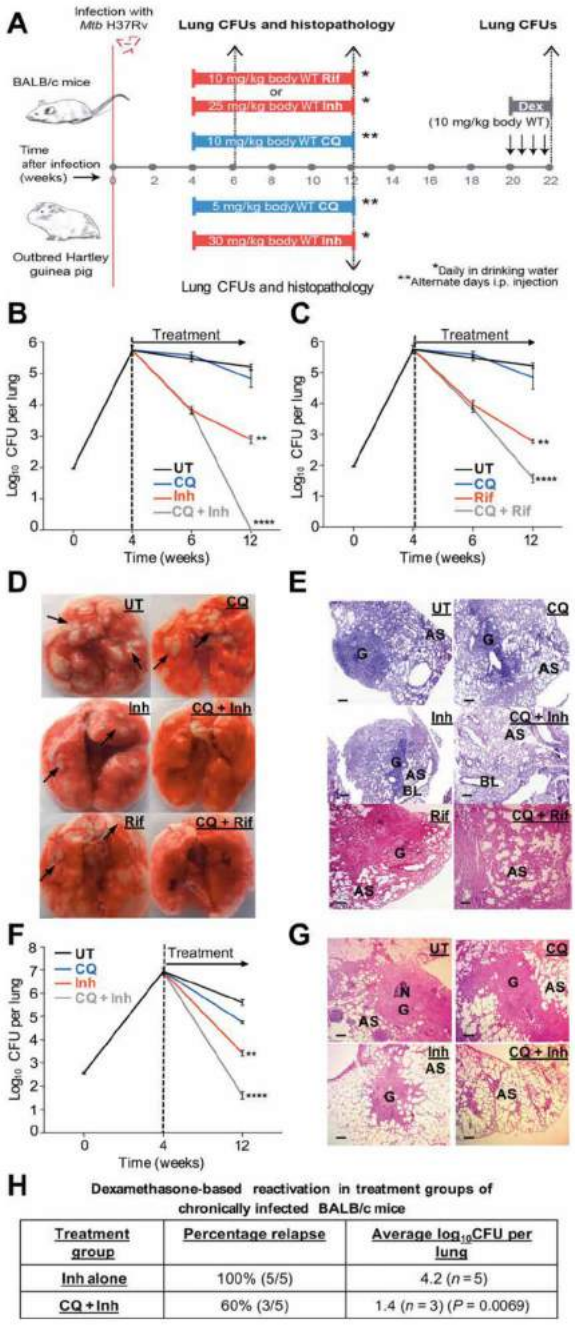

Treatment group	Percentage relapse	Average $\log_{10}$CFU per lung
Inh alone	100% (5/5)	4.2 (n = 5)
CQ + Inh	60% (3/5)	1.4 (n = 3) (P = 0.0069)

Fig. 6. CQ counteracts drug tolerance and reduces relapse in vivo.

(**A**) Strategy to investigate the efficacy of CQ in reducing tolerance against Inh and Rif and post-therapeutic relapse in vivo. BALB/c mice (n = 6) were given an aerosol challenge with WT *Mtb*. From 4 weeks p.i. onward, groups of mice were left untreated or treated with anti-TB drugs (Inh/Rif) alone or in combination with CQ (CQ + Inh/ CQ + Rif). (**B** and **C**) Bacterial CFUs were measured in the lungs at the indicated time points. $^{**}P < 0.01$, $^{****}P < 0.0001$, by Kruskal-Wallis test with Dunn's correction across experimental groups at 12 weeks p.i. (**D**) Gross pathology of the lungs of WT *Mtb*–infected mice at 8 weeks of

Europe PMC Funders Author Manuscripts

Europe PMC Funders Author Manuscripts

treatment across experimental groups. (**E**) Hematoxylin and eosin–stained lung sections (8 weeks of treatment) from mice infected with WT *Mtb* across experimental groups. The pathology sections show granuloma (G), alveolar space (AS), and bronchiole lumen (BL). All images were taken at ×40 magnification. Scale bars, 200 μm. (**F**) Outbred Hartley guinea pigs ($n = 6$) were given aerosol challenge with WT *Mtb*, and efficacy of CQ in reducing Inh tolerance was assessed as described in (B) and (C). $^{**}P < 0.01$, $^{****}P < 0.0001$, by Kruskal-Wallis test with Dunn's correction across experimental groups at 12 weeks p.i. (**G**) Hematoxylin and eosin–stained lung sections (8 weeks of treatment) from guinea pigs infected with WT *Mtb* across experimental groups. The pathology sections show granuloma (G), alveolar space (AS), and necrotic core (N). All images were taken at ×40 magnification. Scale bars, 200 μm. (**H**) Dexamethasone-induced reactivation of *Mtb* from the lungs of BALB/c mice ($n = 5$) after treatment with Inh alone or a combination of CQ plus Inh. Mann-Whitney test was used to compare the relapse frequency (Inh alone versus CQ + Inh combination) for effectiveness of CQ therapy ($P = 0.0069$). Data shown in each panel are the results of two independent experiments (means ± SD). ns, no significant difference ($P > 0.05$).

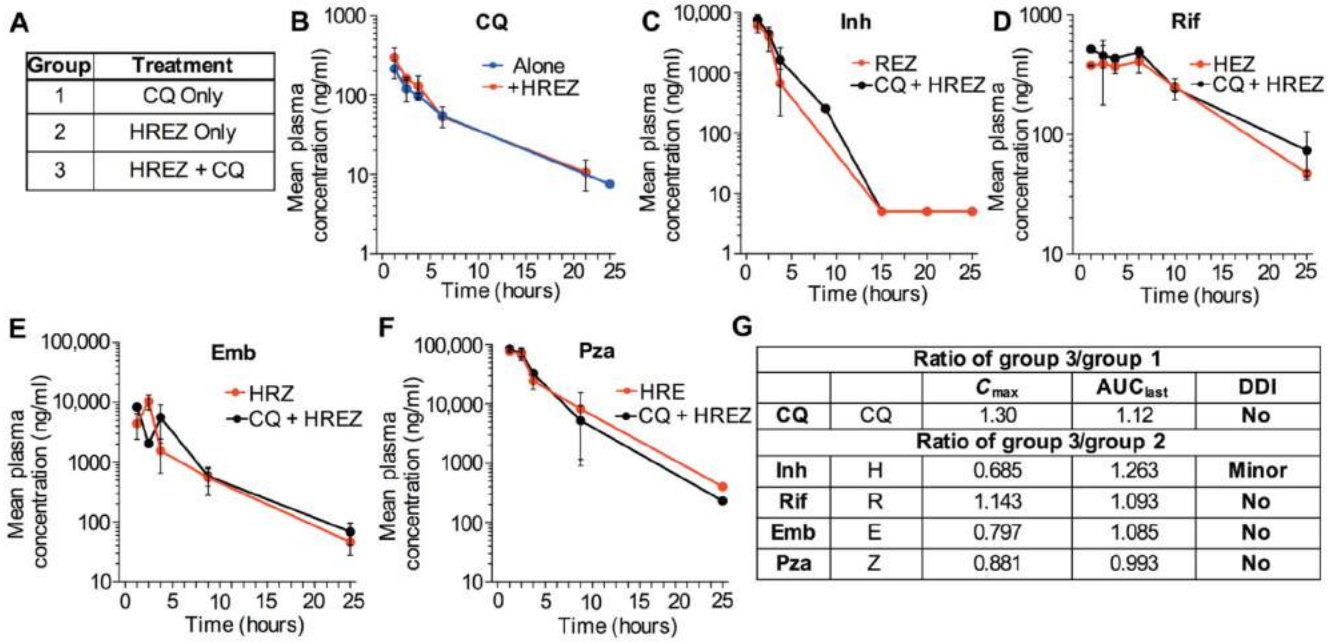

Group	Treatment
1	CQ Only
2	HREZ Only
3	HREZ + CQ

G

		Ratio of group 3/group 1		
		C_{max}	AUC_{last}	DDI
CQ	CQ	1.30	1.12	No
		Ratio of group 3/group 2		
Inh	H	0.685	1.263	Minor
Rif	R	1.143	1.093	No
Emb	E	0.797	1.085	No
Pza	Z	0.881	0.993	No

Fig. 7. CQ exhibits no adverse interactions with anti-TB drugs.

(**A**) The table indicates three groups of treatment in BALB/c mice used in the pharmacokinetic study: CQ alone, front line anti-TB combination therapy (HREZ), and combination (CQ + HREZ). (**B** to **F**) Line plots indicate pharmacokinetic profiles of CQ and individual drugs of the anti-TB therapy regimen analyzed individually and in the presence of each other in plasma of animals over 24 hours. No significant difference was observed between groups at each time point indicated in each panel by Mann-Whitney test ($P > 0.05$). (**G**) The table depicts ratios of C_{max} and AUC_{last} of individual drugs alone or in combination to analyze drug-drug interaction. Doses used are the following: CQ, 10 mg/kg body weight, i.p.; Inh/H, 25 mg/kg body weight, p.o.; Rif/R, 10 mg/kg body weight, p.o.; Emb/E, 200 mg/kg body weight, p.o.; Pza/Z, 150 mg/kg body weight, p.o. p.o., per os consumption; BDL, below detection limit. All data are means ± SD of concentrations at each time point of samples in triplicates ($n = 3$ animals per group).

Europe PMC Funders Author Manuscripts